이학박사 학위논문

Cell cycle regulation by ankyrin repeat-rich membrane spanning scaffold protein and size-dependent fractionation of human mesenchymal stem cells using microfluidic chip filtration

Ankyrin repeat-rich membrane spanning 단백질에 의한
세포주기 조절 기작 및 미세유체칩을 이용한
중간엽 줄기세포의 크기별 분리 연구

2017 년 2 월

서울대학교 대학원

치의과학과 구강악안면 해부 및 영상과학 전공

정 희 경

Ankyrin repeat-rich membrane spanning 단백질에 의한 세포주기 조절 기작 및 미세유체칩을 이용한 중간엽 줄기세포의 크기별 분리 연구

지도교수 장 미 숙

이 논문을 이학박사학위 논문으로 제출함

2016 년 10 월

서울대학교 대학원

치의과학과 구강악안면 해부 및 영상과학 전공

정 희 경

정희경의 이학박사학위논문을 인준함

2016 년 12 월

위 원 장 김 재 범

부 위 원 장 장 미 숙

위 원 노 상 호

위 원 공 영 은

위 원 金 明 錫

ABSTRACT

Cell cycle regulation by ankyrin repeat-rich membrane spanning scaffold protein and size-dependent fractionation of human mesenchymal stem cells using microfluidic chip filtration

Heekyung Jung
Department of Oral Anatomy
The Graduate School
Seoul National University
(Directed by Prof. Mi-Sook Chang, D.D.S., Ph. D.)

As one of the adaptor proteins, ankyrin rich membrane spanning protein (ARMS/Kidins220) is highly expressed in the nervous system, such as the hippocampus, olfactory burb, and motor neurons in the spiral cord. Generally, ARMS/Kidins220 interacts with the neurotrophin, ephrin, vascular endothelial growth factor (VEGF) and glutamate receptors, which have many essential roles in the nervous system such as neuronal survival, neuronal differentiation, dendrites and synapse developments. Recent studies have reported that this protein yields sustained signal of the mitogen-activated protein kinase (MAPK) via the CrkL-C3G complex and Rap1, which are both highly expressed in melanoma. This suggests the ARMS is a potential oncogene and is involved

in controlling cell cycle.

Cell proliferation is tightly controlled by cyclins and cyclin-dependent kinase (CDKs) in G_1, S, M, and G_2 phases. First, we observed that knockdown of ARMS/Kidins220 inhibited mouse neuroblastoma cell proliferation and resulted in a slowdown of cell cycle during G_1 phase by reductions of cyclin D1 and CDK4. In addition, these decrease in cyclin D1 and CDK4 protein levels cause a subsequent reduction of pRb hyperphosphorylation which occurs at the G_1/S phase transition. Moreover, we observed an upregulation of p21, a CDK4 inhibitor, with downregulation of ARMS/Kidins220. Taken together, these data suggest that p21 inhibits the kinase activity of cyclin D1-CDK4 and prevents the hyperphosphorylation of pRb, resulting in down regulation of cell cycle progression. Therefore, we report that the low ARMS/Kidins220 has a role as a signaling mediator to regulate neuroblastoma proliferation and could be worked as a potential oncogene.

Human mesenchymal stem cells (hMSCs) can self-renew and differentiate into multiple cell types, which make them suitable for use in tissue engineering and cell therapy. However, their clinical application is hindered by the need for in vitro culture with growth factors in order for their expansion to reach therapeutically useful levels. Moreover, hMSCs consist of a heterogeneous population that exhibits variable morphology, a limited capacity for self-renewal, and inefficient differentiation. Thus, obtaining purified hMSCs with high potential is an important step toward increasing the efficiency of stem cell therapy.

For the purpose of flow-based identification of hMSC subpopulations, optimally designed microfluidic chips were developed based on the hydrodynamic filtration (HDF) principle. In these chips, hydrodynamic effects for passive separation are combined with fluid interaction along a series of channels. Microfluidic chip design parameters resulted

from complete analysis of laminar flow for flow fraction and complicated networks of main and multi-branched channels, which were validated for microfluidic cell sorting by HDF to fractionate hMSCs into three size-dependent subpopulations: small rapidly self-renewing (RS, < 25 μm); medium spindle-shaped (SS, 25–40 μm); and large flattened (FL, > 40 μm) cells. In our HDF chip, a virtual cut-off width (W_C) boundary causes hMSCs to migrate to sidewalls, whereby they enter branch channels in response to specific ratios between main and side flows. Our results showed continuous and rapid sorting of hMSCs into three subpopulations with highly efficient recovery (>86%) and complete purity rates, and without damage to cells.

Analysis of surface marker expression revealed that RS and SS cells showed high levels of CD73, CD90, and CD105, whereas FL cells did not express CD73. Subsequently, to compare the multipotency of sorted cells, each subpopulation was induced to undergo adipogenic, osteogenic, and Schwann cell (SC) differentiation. Phenotypic and gene marker expression analyses of differentiation indicated that sorted RS and SS subpopulations showed higher potential for adipogenic, osteogenic, and Schwann cell differentiation than the FL subpopulation. Moreover, RS and SS cells displayed significantly increased expression of SC markers and growth factors such as hepatocyte growth factor (HGF) and vascular endothelial growth factor (VEGF).

Therefore, our results indicate that the microfluidic chip successfully sorted hMSCs based on size and target cells with high multilineage potentials were obtained from hMSCs.

Keywords: ARMS/Kidisn220, cell cycle, cyclin D1, cyclin-dependent kinase 4, p21, Human mesenchymal stem cells, Microfluidic sorting chip, Hydrodynamic filtration,

Student Number: 2009-31135

CONTENTS

LIST OF TABLES AND FIGURES

CHAPTER Ⅰ

CHAPTER Ⅱ

CHAPTER Ⅲ

ABBREVIATIONS

ARMS	Ankyrin repeat- rich membrane spanning protein
CDKs	Cyclin dependent kinases
ppRb	Hyperphosphorylated retinoblastoma protein
hMSCs	Human mesenchymal stem cells
HDF	Hydrodynamic filtration
μ-TAS	Micro-total-analysis-system
PDMS	Polydimethylsiloxane
RS	Rapidly self-renewing cells
SS	Spindle shaped cells
FL	Flattened cells
Re	Reynolds number
W_C	Cut-off width
γ_h	The equivalent hydraulic radius
DI	Deformation index
PPARγ2	Peroxisome proliferator-activated receptor gamma 2
LPL	Lipoprotein lipase
RUNX2	Runt-related transcription factor 2
MSX2	Msh homebox homologue 2
OPN	Osteopontin
OCN	Osteocalcin
GFAP	Glial fibrillary acidic protein
HGF	Hepatocyte growth factor
VEGF	Vascular endothelial growth factor

CHAPTER I

General introduction

I. Regulation of cell cycle

Cell cycle can be subdivided into four different phases, referred to as G_1-(gap-1/growth), S- (DNA synthesis), G_2- (gap-2) and M-phase (mitosis) (Bertoli et al., 2013) (Fig. 1). Altogether, G_1-, S- and G_2-phase represent the interphase, which prepares the cell for division during mitosis. In G_1-phase, the cell integrates intra- and extracellular signals and decides to continue replication or to pause cell cycle progression. When pausing, cells can either undergo apoptosis or enter a quiescent, nondividing state (G_O) which still allows a re-entry into cell cycle (Fig. 1).

A complex network of regulatory proteins controls cell cycle at several restriction points. An initial restriction point determines if a cell in G_1-phase enters S-phase. Furthermore, other DNA structure checkpoints prevent the cell from phase transition and cell division if DNA is damaged or imperfectly replicated. The importance of these checkpoint mechanisms becomes apparent through analysis of mutations of the required regulatory proteins during oncogenesis (Massagué, 2004). Numerous proteins that regulate transcription of specific genes control the correct transition throughout the different cell cycle phases. For all cell types, the activation of cyclin-dependent kinases (CDKs) is an essential prerequisite for cell cycle transition (Massagué, 2004). CDKs belong to the CMGC-group of protein kinases

and fulfill core functions in cell cycle regulation when activated by binding a cyclin subunit (Manning et al., 2002). Each cyclin interacts one or two different CDKs and vice versa. The different stages of the cell cycle are associated with an oscillating appearance of different cyclins. D-type cyclins are active in G1-phase, E- and A-type cyclins in S-phase and B- and A-type cyclins in M-phase (Murray, 2004).

Ubiquitination by the Skp1-cullin-F-box protein (SCF)-complex depends on phosphorylation (P) by upstream kinases like GSK3β (glycogen synthase kinase-3 β). In G_1-phase, the pocket proteins, retinoblastoma protein (RB), retinoblastoma-like proteins 1, or -2 (RBL1 or RBL2) bind and inhibit transcription factors of the E2F family, which control gene transcription. After cyclin D/CDK4/6 dependent phosphorylation, pocket proteins release E2F transcription factors to initiate gene transcription for cell cycle progression to S-phase (Massagué, 2004). Oscillation of cyclin ensures correct progression to the next cell cycle stage while preventing reverse progression. For proper regulation of cyclin/CDK complexes during cell cycle progression, cyclins have to be inactivated, which is assured by rapid protein degradation via the ubiquitin-proteasome system. Upon selective phosphorylation, cyclins are recognized by the SCF E3 ubiquitin ligase and are subsequently ubiquitinated for 26S proteasomal degradation. Alternatively, without prior phosphorylation, cyclins can be recognized by another E3 ligase named anaphase-promoting complex (APC) (Vodermaier, 2004) (Fig. 2).

Since the SCF complex is active throughout the entire cell cycle, and the APC is activated at the onset of the anaphase, the complexes function in different stages of cell cycle. G_1-phase cyclins therefore are ubiquitinated by the SCF complex, whereas mitotic cyclins are targeted by the APC (Murray, 2004). In

addition to regulation of cyclin D and E protein stability, cyclin/CDK activity is additionally controlled by CDK inhibitors (CKIs) at the transition from G_1- to S-phase. Based on their structure and specificity, CKIs are divided into two families. The INK4 family (inhibitors of CDK4) consists of p16INK4a, p15INK4b, p18INK4c, and p19INK4d, which specifically bind to CDK4 and CDK6 and disturb their interaction with the respective D-type cyclins (Sherr and Roberts, 1999). In contrast, CKIs of the Cip/Kip1 family, comprising p21Cip1/Waf1 (also called cyclin-dependent kinase inhibitor 1A, CDKN1A), p27Kip1 (CDKN1B) and p57Kip2 (CDKN1C), are characterized by their binding to CDKs and cyclins. Cip/Kip1 CKIs regulate the activity of cyclin D-, E-, A- and B-/CDK complexes (Sherr and Roberts, 1999; Besson et al., 2008). Heterozygous p27Kip1 knockout mice showed increased body size and organ hyperplasia, whereas a p21Cip1/Waf1 knockout resulted in deregulation of DNA-damage dependent G_1-phase cell cycle arrest (Besson et al., 2008). The knockout of p57Kip2 led to organ hyperplasia due to a defective cell cycle exit (Zhang et al., 1997). Cip/Kip proteins are intrinsically unstructured and only adopt specific conformations after binding to other proteins (Lacy et al., 2004), allowing for a broad range of binding partners.

In addition to blocking G_1-S-phase progression, CKIs of the Kip/Cip family fulfill additional functions in the regulation of gene transcription, apoptosis, cell motility, and differentiation (Besson et al., 2008). Post-translational modifications, especially phosphorylation, are thought to modulate protein functions by influencing stability, binding partners affinity or subcellular localization (Borriello et al., 2007). Once a cell has decided to replicate, one important function of G_1-

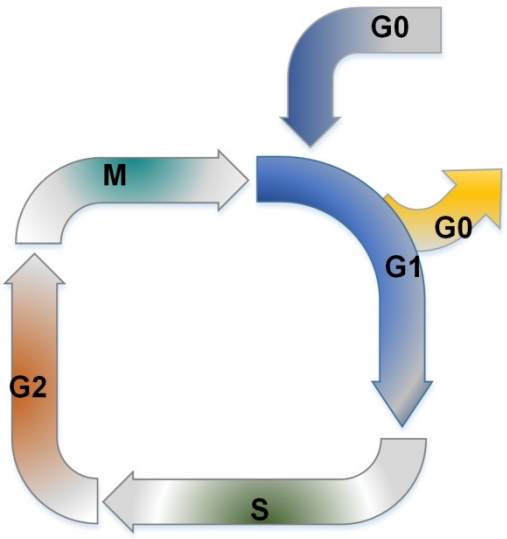

Figure 1. Overview of cell cycle. The mammalian cell cycle is divided into four different phases. In G_1-phase, the cell can decide to enter a quiescent state (G_O) or to prepare entering S-phase for DNA replication and subsequent cell division. In G_2-phase, the cell prepares for cytokinesis (M-phase). (Massagué , 2004).

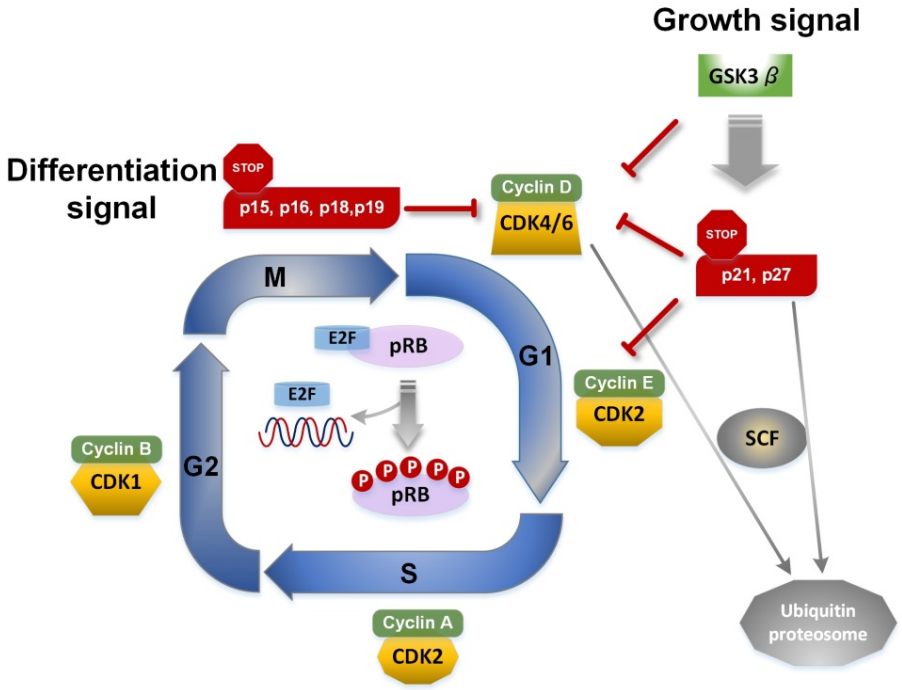

Figure 2. Major components of cell cycle regulation. Different cyclin/CDK-complexes are assembled in different phases of cell cycle and function as regulators of cell cycle progression by phosphorylation of various proteins (Murray, 2004). Upon differentiation or lacking growth signals in G_1-phase, the activity of cyclin/CDK complexes is inhibited by CKIs (cyclin-dependent kinase inhibitors) of the INK4 (p15, p16, p18, p19) or Cip/Kip (p21Cip1, p27Kip1, p57Kip2) family (Sherr and Roberts, 1999; Besson et al., 2008). On the other hand, cyclin/CDK-complexes are regulated by rapid degradation of the cyclin component via the ubiquitin proteasome pathway and being targeted by E3 ubiquitin ligases of the APC- (Anaphase promoting complex) or SCF-type (Skp1-cullin-F-box protein) (Vodermaier, 2004).

phase is to prepare the cell for DNA replication and subsequent cell division. Therefore, during G_1-phase the transcription of genes encoding for proteins that are required for cell cycle progression is induced. One of the proteins regulating gene transcription in G_1-S-phase is the tumor suppressor protein RB. The so-called pocket proteins RB, RBL1 (also named p107) and RBL2 (known as p130) inhibit E2F transcription factors due to their binding. In all phases of cell cycle including Go, E2F-dependent gene transcription is inhibited, until cell cycle reaches late G_1-phase. Pocket proteins are then phosphorylated by phase specific D-type cyclin/CDK4/6 complexes and release the E2F transcription factors to induce gene transcription (Bertoli et al., 2013). A complex network of many different proteins thus regulates cell cycle progression. A functional disturbance of one or several of these proteins can deregulate accurate cell cycle progression and potentially promote developmental alterations or severe diseases, such as cancer.

II. Ankyrin-rich membrane spanning protein (ARMS/Kidins220)

ARMS/Kidins220 was initially identified as a substrate for protein kinase D (PKD) in neural cells (Iglesias et al., 2000) and has been independently characterized as a downstream target of the signaling mediated by neurotrophins and ephrins (Kong et al., 2001). This protein is an integral membrane protein with four transmembrane segments and N- and C-terminal tails that are both exposed to the cytoplasm (Fig. 3). Sequence analysis of ARMS/Kidins220 revealed the presence of numerous domains that mediate protein–protein interactions. The N-terminus of ARMS/Kidins220 contains 11 ankyrin repeats, which form a concave binding surface that is accessible to molecular partners, such as the Rho–guanine

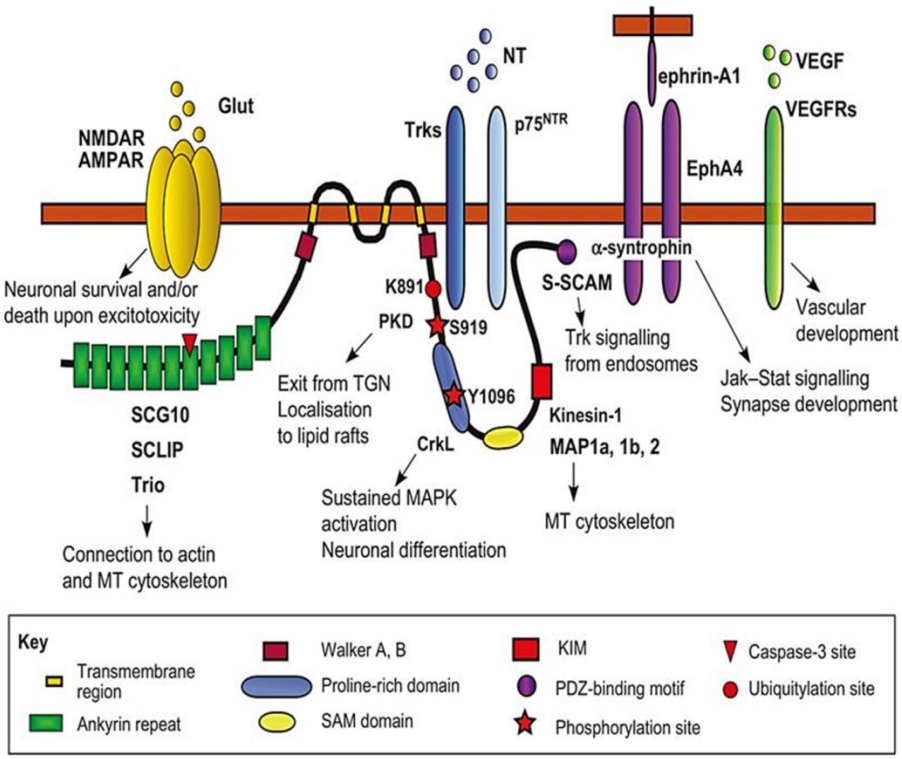

Figure 3. The Structure of ARMS/Kidins220 with multiple protein-protein interaction sites. ARMS/Kidins220 has different domains and sites of post-translational modifications. Also shown are the molecular partners identified to date, the cellular events are triggered by their binding to ARMS/Kidins220 (arrows) (Neubrand et al., 2012).

nucleotide exchange factor (RhoGEF) Trio (Neubrand et al., 2010). ARMS/Kidins220 has been included in PifA (KAP) family of P-loop nucleotide phosphatases (NTPases). P-loop NTPases contain Walker A and Walker B motifs (WA and WB, respectively) (Higgins et al., 1988), which are often involved in the binding of nucleotides and have been identified in the juxtamembrane regions flanking the N- and C- terminus of ARMS/Kidins220. Members of this family are predicted to mediate the assembly of protein complexes that are associated with the inner surfaces of cell membranes (Aravind et al., 2004).

The C-terminus of ARMS/Kidins220 includes several protein-protein interaction domains, such as a proline-rich region (residues 1080–1092) that binds the adaptor protein CrkL (Arevalo et al., 2006), and a sterile alpha motif (SAM; residues 1231–1300) (Iglesias et al., 2000; Kong et al., 2001) that might be involved in both inter- and intra-molecular interactions. In addition, the kinesin light chain (KLC)-interacting motif (KIM) (residues 1387–1426) binds the kinesin-1 motor complex (Bracale et al., 2007). The last four amino acids of ARMS/Kidins220 constitute a PDZ-binding motif that binds the PDZ domain of a-syntrophin, thereby forming a complex that is associated with the EphA4 receptor at the neuromuscular junction (Luo et al., 2005).

The observation that ARMS/Kidins220 interacts with all three Trk receptors and with p75NTR (Arevalo et al., 2004; Chang et al., 2004) prompted a series of studies on the role of ARMS/Kidins220 in various aspects of neurotrophin physiology, mostly focusing on the molecular mechanisms by which ARMS/Kidins220 mediates Trk signaling (Arevalo et al., 2004; 2006). With its multiple domains, ARMS/Kidins220 is a well-suited candidate to act as a signaling

platform, by recruiting cell-specific adaptors and effectors to activated Trk receptors. ARMS/Kidins220 is also involved in functional interactions with several other receptors, such as glutamate, ephrin and vascular endothelial growth factor receptors (VEGFRs) (Luo et al., 2005; Cesca et al., 2012), thus presenting an example of how different trophic pathways can converge and, possibly, be integrated at the level of a single adaptor molecule.

III. ARMS/Kidins220 and neurotrophin signaling

As previously mentioned, ARMS/Kidins220 interacts with Trk receptors (Arevalo et al., 2004), forming a ternary complex with p75NTR (Chang et al., 2004). The interaction between ARMS/Kidins220 and TrkA is mediated by the fourth transmembrane domain of ARMS/Kidins220 and the transmembrane domain of TrkA, whereas the interaction with p75NTR involves the last 250 amino acids of ARMS/Kidins220 (Kong et al., 2001) and the p75NTR intracellular domain (residues 327–342) (Chang et al., 2004). The binding of Trk receptors and p75NTR to ARMS/Kidins220 is differentially modulated by neurotrophins. Formation of ARMS/Kidins220–TrkA complex is involved in NGF and persists for up to 25 hours following stimulation with NGF (Kong et al., 2001). However, the assembly of the ternary complex between ARMS/Kidins220, TrkA and p75NTR is independent of NGF (Chang et al., 2004). Interestingly, increased levels of ARMS/Kidins220 reduce the binding of TrkA to p75NTR, suggesting that ARMS/Kidins220 regulates the formation of receptor complexes that display different neurotrophin-binding affinities (Chang et al., 2004). In addition,

ARMS/Kidins220 selectively mediates the sustained activation of MAPK signaling, without affecting the fast response to neurotrophins or the response to other growth factors, such as epidermal growth factor (EGF) (Kong et al., 2001; Arevalo et al., 2004).

ARMS/Kidins220 is phosphorylated on tyrosine residues in response to NGF and BDNF, the time course of which follows the kinetics of Trk autophosphorylation. This suggests that this protein is a Trk receptor substrate (Kong et al., 2001). In addition, tyrosine phosphorylation of ARMS/Kidins220 occurs simultaneously with that of Shc and PLCc, indicating that this protein is amongst the first to be activated in response to NGF (Arevalo et al., 2004). The adaptor protein CrkL constitutively binds the second poly-proline stretch of ARMS/Kidins220 through its SH3 domain (Arevalo et al., 2006). Upon treating cells with NGF, ARMS/Kidins220 is phosphorylated at tyrosine 1096, causing a conformational change in the CrkL–ARMS/Kidins220 complex. This allows the recruitment of downstream modulators of the MAPK pathway, such as C3G and Rap1 (Arevalo et al., 2006), and determines its sustained activation, which occurs mainly at late endosomes (Hisata et al., 2007). This effect is highly specific, as perturbing ARMS/Kidins220 function using RNA interference (RNAi) or dominant–negative ARMS/Kidins220 constructs does not affect the transient MAPK activation triggered by EGF or the initial steps of MAPK signaling, which are Ras- or Akt-dependent (Arevalo et al., 2004). Impairment of BDNF-induced MAPK activation has also been demonstrated in ARMS/Kidins220-deficient neurons (Cesca et al., 2012). Among the transcription factors activated by the MAPK pathway, ARMS/Kidins220 promotes nuclear factor kappa B (NF-kB)

signaling when cells are treated with BDNF, mediating neuronal survival (Sniderhan et al., 2008). In support of these findings, ARMS/Kidins220–/– embryos show widespread cell death in the central nervous system (CNS) and peripheral nervous system (PNS) and die at birth (Cesca et al., 2012). Remarkably, ARMS/Kidins220 is one of the few proteins that is selectively required for the sustained activation of MAPK signaling, whereas most of the other factors act in both transient and sustained signaling. Because ARMS/Kidins220 has the role in survival pathways such as MAPK signaling, it is recognized as a potential oncogene. Accordingly, ARMS/Kidins220 prevents stress-induced apoptosis in melanoma cells and contributes to tumor progression (Liao et al., 2007; 2011).

IV. ARMS/Kidins220 functions are related to pathologies

Studies performed on ARMS/Kidins220 mutant mice indicate that the alteration of ARMS/Kidins220 protein levels impairs neuronal survival and development. The complete ablation of ARMS/Kidins220 led to embryonic death, which was associated with extensive apoptosis in the CNS and PNS and to cardiovascular abnormalities (Cesca et al., 2011). A partial reduction of ARMS/Kidins220 levels was sufficient to cause defects in spine turnover and synaptic plasticity, with significant repercussions on higher functions such as learning and memory, when studied in adult mice (Wu et al., 2009, 2010; Arévalo et al., 2010; Duffy et al., 2011). Taken together, the results of these studies strongly support the idea that alterations of the ARMS/Kidins220 gene and/or the ARMS/Kidins220 protein is associated with human (neuro) pathologies. Although the literature concerning this aspect of ARMS/Kidins220 function is limited,

several studies have investigated the genetic and molecular pathways linking ARMS/Kidins220 to the onset of various diseases. For example, ARMS/Kidins220 is overexpressed in human samples of melanoma (Liao et al., 2007; 2011), a tumor of neural crest origin, and of neuroblastoma (Rogersand Schor, 2013a; Jung et al., 2014), a cancer type affecting the PNS. In both cases, ARMS/Kidins220 behaves as an oncogene, affecting the ability of cancer cells to survive, proliferate and migrate/metastasize. Additionally, increased ARMS/Kidins220 levels have also been observed in human Alzheimer's disease (AD) samples (López-Menéndez et al., 2013). Here, ARMS/Kidins220 accumulated with hyperphosphorylated Tau protein, probably contributing to the defective NT signaling observed in this pathology. Alterations of ARMS/Kidins220 gene expression have been found in several genetic screens in humans. For example, a microarray-based expression profiling of dopaminergic neurons isolated from the substantia nigra of Parkinson's disease (PD) patients revealed that ARMS/Kidins220 levels were significantly decreased compared to spectrum disorder (ASD) patients, and found increased levels of ARMS/Kidins220 mRNA in ASD patients. Interestingly, genes belonging to the NT pathways were overall the most represented of the affected genes (Kong et al., 2012). Finally, a very recent study was conducted on a small number of schizophrenia patients, by means of high-coverage targeted exome capture on a small number of NT-related genes from blood leukocytes. Interestingly, two ARMS/Kidins220 missense polymorphisms and one novel gene variant were identified in five of 48 schizophrenia patients (Kranz et al., 2015). One of these polymorphisms has been subsequently associated with reduced prefrontal rostralization in schizophrenia patients, compared to healthy control subjects

(Malaspina et al., 2016).

V. Human mesenchymal stem cells

Human mesenchymal stem cells (hMSCs) are multipotent stromal cells that can self-renew and differentiate into ectodermal and mesodermal cell types that can transdifferentiate into cells with endodermal characteristics such as epithelial cells and neurons (Fig. 4). They are found in the central nervous system, where they guide the differentiation of neurons, astrocytes, and oligodendrocytes from neural stem cells (NSCs) (Uccelli et al., 2008). hMSCs contribute to the regeneration of mesenchymal tissues such as bone, cartilage, muscle, ligaments, tendons, and adipose tissue; provide the stroma for tissue engineering; and have been applied as cell therapy for lung injury, kidney disease, diabetes, graft-versus-host disease including neurodevelopmental and neurodegenerative diseases, Parkinson's disease, and Alzheimer's disease (Kennea et al., 2002).

hMSCs are traditionally derived from bone marrow, which contains a large number of red blood cells (RBCs) (Jiang et al., 2002). hMSCs are larger than RBCs. Thus, a size-based separation tool is essential to isolate or concentrate hMSCs from bone marrow. In addition, the cells can be isolated from cord blood, placenta and amniotic fluid (Lee et al., 2004; Yen et al., 2005; Tsai et al., 2006).

A great deal of research on adult stem cells has focused on their capacity to divide or self-renew and their differentiation potential. Adult stem cells are present in the brain, bone marrow, peripheral blood, blood vessels, skeletal muscle, skin, teeth, heart, liver, ovaries, and epithelium. They are easily derived from peripheral tissues without ethical concerns, in contrast to in human embryonic research.

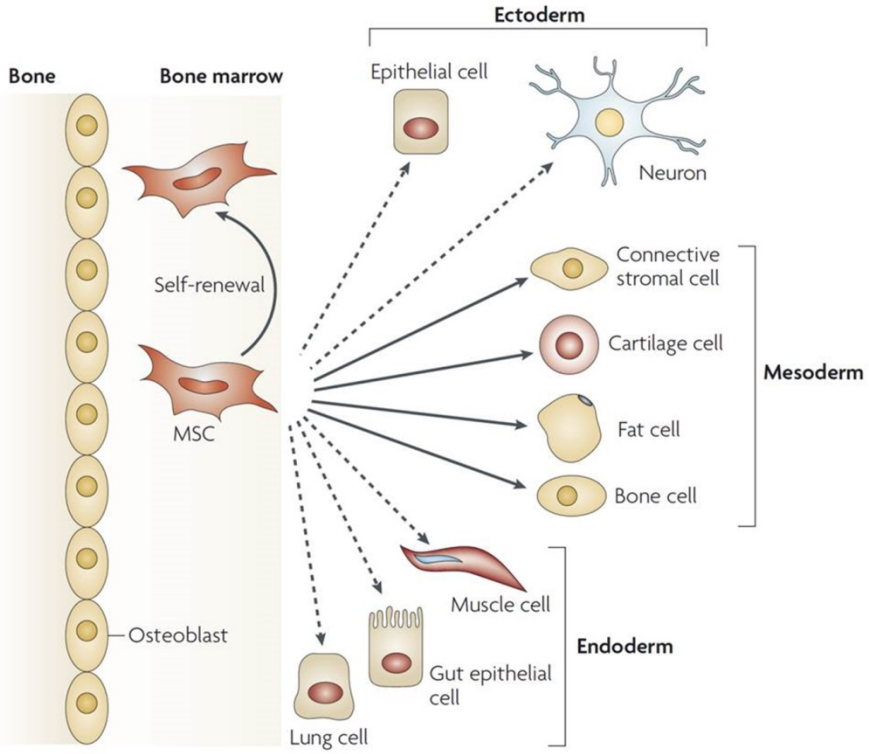

Figure 4. The multipotentiality of MSCs. This figure shows the ability of mesenchymal stem cells (MSCs) in bone-marrow cavity to self-renew (curved arrow) and to differentiate (straight, solid arrows) towards the mesodermal lineage. The reported ability to transdifferentiate into cells of other lineages (ectoderm and endoderm) is shown by dashed arrows, as transdifferentiation is controversial in vivo (Uccelli, et al., 2008).

hMSCs express many surface markers, including cluster of differentiation (CD) 29, CD44, CD49-af, CD51, CD73, CD90, CD105, CD106, CD166, and Stro1, but lose hematopoietic lineage markers, such as CD11b, CD14, and CD45 (Phinney and Prockop, 2007; Lv et al., 2014). hMSCs are known to improve tissue damage in response to injury and disease, and their therapeutic effects have been verified in animal models of lung injury, kidney disease, diabetes, myocardial infarction, and neurologic disorders. Indeed, soluble factors including hepatocyte growth factor (HGF), transforming growth factor-β (TGF β), vascular endothelial growth factor (VEGF), TNF-stimulated gene 6 (TSG-6), prostaglandin E2 (PGE2), and galectins 1 and 9, emitted by hMSCs alter the tissue environment and may play a prominent role in tissue repair (Prockop, 2007; Madrigal et al., 2014).

VI. Microfluidics

In the early 1980s, microfluidic technology developed as a functional extension of microelectromechanical systems technology and led to the creation of "micro total analysis systems" (μ-TAS) or "lab-on-a-chip" (LOC). These miniaturized systems can be used to realize entire procedures performed in traditional laboratories with the advantages of decreasing sample/reagent consumption, reaction/analysis time, and the risk of contamination, increasing sensitivity and reliability, and the ability to run multiple processes sequentially (Primiceri et al., 2013; Titmarsh et al., 2014) (Fig. 5).

Therefore, researchers have been attracted to this technology and have applied it in their studies to achieve the manipulation of fluids in microchannels

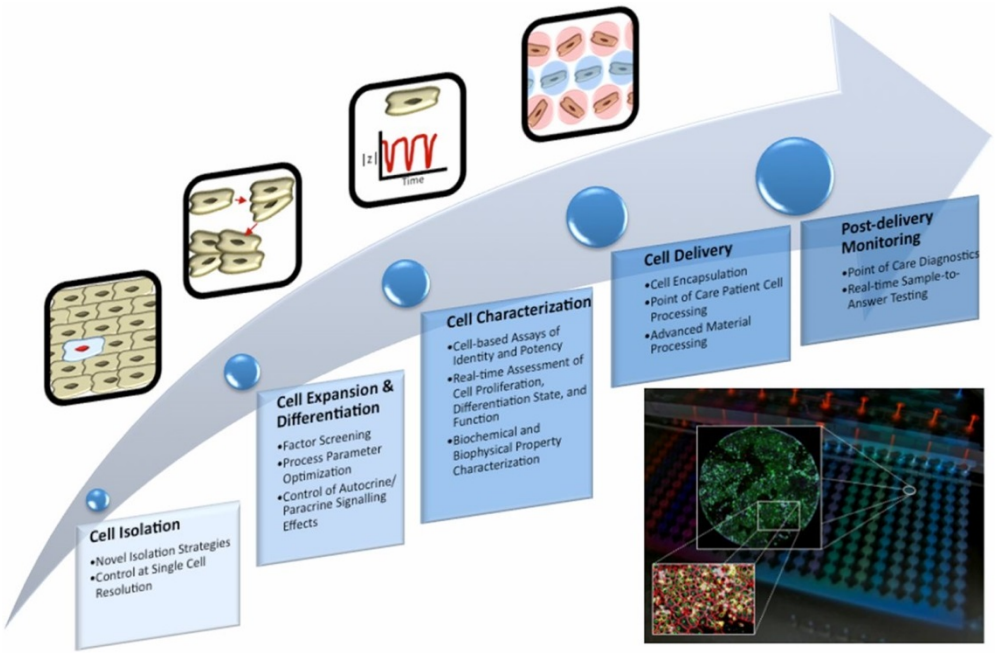

Figure 5. Microfluidic technologies add insight to cell therapy processes. This flow diagram shows a generic cell therapy implementation process. Bullet points in each step highlight areas where microfluidic technologies can add insight. The inset shows how integrated microfluidic platforms provide both control of culture conditions and readout of cellular phenotypes (Titmarsh et al., 2014).

ranging from the nano- to micrometer scales (Wu et al., 2011). Microfluidic systems can be fabricated using a variety of microfabrication processes from materials such as polymers, glass, silicon, and metals, depending on the specific requirements and specifications. In particular, polydimethylsiloxane (PDMS)-based microfluidic devices have several useful characteristics, such as elasticity, durability, biocompatibility, optical transparency, gas permeability, no toxicity, and low electrical conductivity. PDMS devices are replicated from a mold usually made via a soft-lithography technique because of advantages such as low cost, ease of fabrication, and rapid processing (MacDonald et al., 2002). A variety of microfluidic devices have been fabricated based on this microfabrication process, including micropumps, microvalves, and micromixers. Furthermore, these PDMS-based microfluidic devices can be integrated to perform a specific assay for applications such as molecular diagnosis, protein analysis, and cell studies (Wu et al., 2011).

From mid-2000, microfluidic systems developed to offer cells an in vivo-mimicking microenvironment that is challenging to realize in traditional large-scale two-dimensional (2D) systems. Moreover, the capability to perform perfusion allowed the infusion of assay reagents while high optical transparency enabled real-time imaging and analysis of cellular responses. These characteristics significantly improved the culture and analysis of stem cells, which are important in the field of medicine. Consequently, numerous precision microfluidic platforms have been developed for the study of different types of stem cell, including embryonic stem cells (ESCs), MSCs, hematopoietic stem cells (HSCs), and NSCs that offer many useful capabilities, such as isolation, culture and differentiation, stimulation, and

signaling analysis. Specially, monitoring the real-time responses of stem cells yields a literal, straightforward result because stem cells tend to undergo morphologic changes easily after long experimental processes (Wu et al., 2011; Titmarsh et al., 2014) (Fig. 5).

VII. The application of microfluidics in stem cells therapy

Microfluidics represent an alternative tool for stem cell therapy in clinical applications that require rapid isolation and precise counting of these cells and accurate control of multiple parameters affecting metabolic rates, viability, and cell characterization. Therefore, microfluidic systems may become a powerful platform for both fundamental stem cell research and commercial applications in the near future.

Cell sorting or separation—isolating cells of interest from a large number of samples, or distinguishing cells that belong to different subgroups—is essential for many biomedical and chemical analyses, and is a basic step in many diagnostic and therapeutic metho`ds. Traditionally, fluorescence-activated cell sorting (FACS) and magnetic-activated cell sorting (MACS) are two of the conventional single cell-level sorting strategies (Fu et al., 1999; Nilsson et al., 2009). In FACS separation, specific antibodies labeled with fluorescent molecules are attached to individual cell samples to identify a subset of cells with specific properties. During sorting, the cells flow in a stream at a relatively high speed, and a detector sensitive to the fluorescent signal is situated along the flow stream. The detector observes either light scattering or the presence or absence of the fluorescent signal when each cell passes. After collecting the data from this observation, various actuation methods

can be applied to implement separation. For MACS separation, antibody-conjugated magnetic beads are bound to specific proteins in cells of interest. A magnetic field gradient is then applied beside the main stream of the flow of sample cells. Subjected to magnetic force, the cells that have bound to the beads are isolated from the main stream of the sample.

Both FACS and MACS rely on antibodies as additional tags or labels to identify specific cells. The labeling steps necessary for this can complicate the separation processes, and the attachment of antibodies increases the cost of separation. Indeed, the attachment of antibodies may have an effect on the functionality of the cells. Therefore, it is preferable to use the intrinsic properties of cells as biomedical and biophysical markers for separation or sorting. These properties include size, shape, electrical impedance, density, deformability, and hydrodynamic properties. Studies on these intrinsic properties of cells help researchers to achieve a better understanding of cell characteristics and functions. The identification and isolation of particular cells from clinical samples may be a powerful method of the diagnosis and therapeutic treatment of many diseases.

Several LOC microfluidic technologies involving label-free cell sorting are emerging especially based on cell size and deformability. In size-based sorting, active sorting methods apply external optical/magnetic/electrical force fields across the cell flow stream, whereas passive sorting methods rely on the structure of the microfluidic device or hydrodynamic forces generated in the flow, such as drag force and inertial lift force (Di Carlo et al., 2007; Petrsoon et al., 2007; Yamada et al., 2007). Several corresponding technologies, such as external optical force field,

mechanical pressing, and hydrodynamic stretching are also used for deformability based sorting (MacDonald et al., 2003; Geislinger et al., 2014).

VIII. Microfluidics for size based cell separation

Size is one of the basic physical properties of a cell. Many microscale cell-separation techniques take advantage of these intrinsic properties for high-performance separation. These techniques can be broadly classified as active and passive separation techniques. Generally, active techniques rely on an external force field for functionality, whereas passive techniques rely entirely on the channel geometry and inherent hydrodynamic forces for functionality.

Many intrinsic properties of cells, such electrical conductivity, optical polarizability, magnetic properties, and mass are relative to cell size. For example, electrical impedance or conductivity varies with cell diameter. When subjected to an external field that transduces a size-dependent, force-bearing response in the cell, the difference in these properties between cell types can be recognized by the difference in the magnitude of such forces. Utilizing this phenomenon, several types of cell separation have been developed (MacDonald et al., 2003; Pamme et al., 2004; Petrsson et al., 2007; Vahey & Voldman, 2008) (Fig. 6).

As cell mixture enters one inlet, the side flow from the other inlet aligns the cell sample to one of the channel side walls. When the cells reach the fractionation chamber, they come under the influence of the external force field. The external force field induces the vertical migration of cells in relation to their size. The cells are thus separated when exiting the chamber. By designing a bifurcation near the exit of the chamber section, cells of different sizes and other

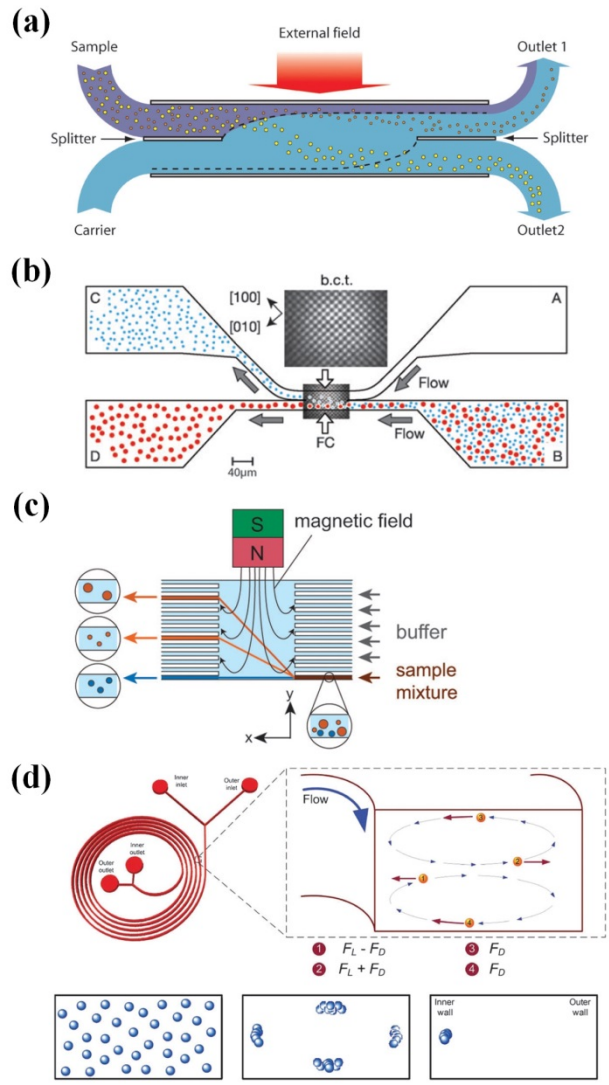

Figure 6. Continuous separation in microfluidic systems. Sample or multiple cells injected into inlet and flow into each separation chamber with various sorting principles; (a) Split flow thin (SPLITT) fractionation (b) optical fractionation (c) magnetophoresis (d) inertia and Dean flow.

intrinsic properties are guided to different outlets, thus achieving separation.

The integration of external force fields, such as split-flow thin-cell (SPLITT) fractionation, an optical field, a magnetic field, an electric field or inertial, and Dean flow fields, increases the complexity of the device and its production cost (Giddings et al., 1985; MacDonald et al., 2003; Pamme et al., 2004; Vahey & Voldman, 2008; Petrsson et al., 2007). Also, the biologic structure of the cells may be damaged through energy absorption, thus affecting the downstream analysis of the cell samples. These disadvantages are motivating researchers to find more reliable technologies for cell separation.

SPLITT fractionation, originally developed by Giddings et al. (1985), is based on the difference in velocity between the sample suspension and a carrier stream. As shown in Fig. 6a, a particle suspension and a carrier stream are moved into a separation chamber at different velocities. Flow splitters at the entrance and exit of the chamber smooth the flow and define inner and outer splitting planes. A force field, such as gravity, an electric field, or a magnetic field, is applied perpendicularly to the direction of flow, deflecting some of the particles into the carrier stream (Huh et al., 2007; Lai et al., 2009). Continuous separation using magnetophoresis was first reported by Pamme and colleagues in 2004. In this method, the suspended particles or cells are separated according to size because the larger particles are most affected and subsequently end up in an outlet closer to the magnet. This magnetic force is used to modify not only magnetic particle- or magnetically labeled cells, but also non-magnetic objects. It is utilized to separate white blood cells (WBCs) from red blood cells (RBCs), but it struggles to sort samples with similar diamagnetic characteristics (Furlani, 2007).

One passive sorting method, optical sorting, can be achieved by means of an optical interference pattern, a so-called optical lattice (MacDonald et al., 2003) (Fig. 6b). A three-dimensional optical field can be generated such that the optical force is directed perpendicular to the direction of flow. The optical force on a particle or cell depends on optical polarizability. Sorting can be achieved based on differences in particle size or refractive index.

In inertial microfluidics, the particle experiences lifting in a shear-flow field environment due to the shear-induced lift-force and wall-induced lift effect (Fig. 6d). It results in particle migration across the stream of laminar flow (Bhagat et al., 2008), and curved channels produce a secondary flow that arises from a mismatch in velocity between central and near-wall regions of a channel. Central fluid elements have a larger inertia than fluid elements at the walls, and tend to flow outward around a curve, creating a pressure gradient along the curve. The design consists of two inlets and two outlets, and the sample is introduced through the inner inlet. Neutrally buoyant particles experience lift forces and Dean drag force within the microchannel.

Microchannel cross-sections illustrating the principle of inertial migration for particles with ap, which results in differential particle migration (/D_h ~ 0.1). The randomly dispersed particles align in the four equilibrium positions within the microchannel where the FLs balance each other. Additional forces due to Dean vortices reduce the four equilibrium positions to just one near the inner microchannel wall.

Although inertial lift force can affect separation efficiency in hydrodynamic filtration (HDF) and pinched-flow fractionation (PFF), they may

also be employed for size-based cell separation. The first design to utilize inertial lift force for particle sorting was introduced by Di Carlo et al. (2007). Various designs based on inertial force-induced separation were subsequently developed by many groups (Bhagat et al., 2008; Kuntaegowdanahalli et al., 2009). The significant advantage of this method is that separation relies entirely on intrinsic hydrodynamic forces. Consequently, the design of the system is simple. Also, because of the large channel dimensions (relative to sample-cell sizes), this method can achieve high volume throughput and eliminate clogging. However, this method has a limitation in terms of the efficiency of tiny cells removed because of their uniform distribution. Moreover, the size difference between the cell groups to be separated should be considerably large, so that one group can be focused on while no significant inertial effect is active on the other groups.

IX. Hydrodynamic filtration

Differing from methods that require an external field to induce cell separation, HDF is another passive separation method featuring multiple capillary branches perpendicular to the main flow thereby aligning all particles along the side walls of the main channel (Yamada et al., 2004). In this method, particles are introduced into the main channel, and side branches drain liquid from the main channel continuously, the smaller particles are closer to the side wall than larger particles because of the difference in size, resulting in them being filtered out earlier than larger-sized particles. The separation mechanism is based purely on the relative flow profile, and not on microchannel geometry. When the relative flow rate in the side channels is low (Fig. 7a), no particles are diverted into the side branches-only

fluid. A medium flow rate is applied to the side channels (Fig. 7b), allowing small particles to be separated with the medium, but not large particles, which have a hydrodynamic center line outside the dashed flow line that diverts into the side branch. Relatively high flow rates in the side channels (Fig. 7c) result in no particle separation. The dashed lines in Figs. 7a-c show the virtual boundaries of the layers of fluid in the main channel that will be diverted into the side branches. Before the separation branches, there are multiple branches responsible for aligning and concentrating the particles along the side walls by medium removal. The technique has also been demonstrated in the separation of WBCs from RBCs. An alternate design, providing improved particle alignment prior to hydrodynamic separation, was also developed, in which the carrier medium fractions removed during the alignment process were recombined with the main flow (Yamada and Seki et al., 2006). By adding extra inlets perpendicular to the flow, carrier–medium exchange is performed in several steps, providing an aspiration and washing procedure for continuous-flow cell processing (Yamada and Seki, 2007). Recently, Seki and his colleagues combined magnetophoresis to the concept of HDF-based microfluidics, and sorted cells based on size and surface markers (Mizuno et al., 2013). As the separation mechanism is based purely on the low profile not microchannel geometry, channels significantly larger than the cell diameter can be employed, minimizing clogging and increasing throughput.

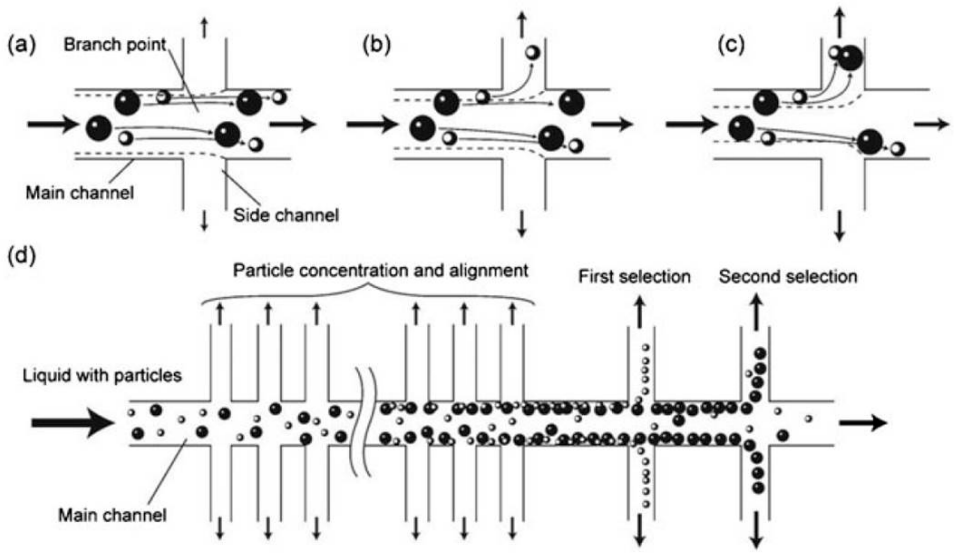

Figure 7. The hydrodynamic filtration principle. Fluids and particles entered into main channel are removed gradually from the side branches perpendicular to the main flow. This action will eventually line up particles along the main channel walls. By controlling the flow rate of the side branch flow it is possible to remove particle fractions of a particular size while larger particle moves on to be separated later (Yamada and Seki, 2005; Lenshof and Laurell, 2010).

CHAPTER II

Ankyrin repeat-rich membrane spanning (ARMS/ Kidins220) scaffold protein regulates neuroblastoma cell proliferation through Cyclin D1/CDK4 and p21

Parts of the data shown in this thesis have been published in

Molecules and Cells 2014 37: 881-887

I. Abstract

Ankyrin rich membrane spanning protein (ARMS/Kidins220) is known as an adaptor protein which highly is expressed in nervous system and selectively binds to neurotrophin-neurotrophin receptor complex to transfer the signal to downstream in nervous system.

Recent studies have reported that this protein make sustained signal of the mitogen-activated protein kinase (MAPK) via CrkL-C3G complex and Rap1 and are shown high expression in melanoma. These suggested the ARMS might be a potential oncogene and involved in controlling cell cycle.

In our data, the knockdown of ARMS/Kidins220 inhibits neuroblastoma cell proliferation and resulted in inducing slowdown of cell cycle in G1 phase, which resulted in resulted in significant reduction of cyclin D1 and CDK4. In addition, these decrease of protein levels cause subsequent reduction of pRb hyperphosphorylation. Moreover, we observed upregulation of p21, a CDK4 inhibitor, according to downregulation of ARMS. Taken together, this data suggest that p21 inhibit the kinase activity of Cyclin D1/CDK4 and prevent the hyperphosphorylation of pRb result in down regulation of cell cycle progression. Therefore, our results represent that ARMS/Kidins220 might have a new role as a signaling mediator to regulate neuroblastoma proliferation and could be worked as a potential oncogene.

II. Introduction

Ankyrin repeat-rich membrane spanning (ARMS, as known as Kidins220) protein has been identified a transmembrane protein and is highly expressed in nervous system and colocalized with TrkA-C and p75, as the receptors of on the cell surface of sympathetic neurons in the developing nervous system (Igresias et al., 2000; Kong et al., 2001). It has important roles in neuronal differentiation, survival and development. The proteins have multifunctional scaffold protein and its various domains for protein-protein interactions (Iglesias et al., 2000; Kong et al., 2001). Thus, several research groups have studied the structure and interactions with complexes of receptors and effects in various mechanisms (Chao, 2003; Neubrand et al., 2012) (Fig. 1).

Specifically, ARMS/Kidins220 critically acts as a major signaling factor involved in prolonged MAP kinase signaling by neurotrophins (Arevalo et al., 2004; 2006) and might regulate the levels of pMAPK and I nfluence on neuronal cell death mediated by excitotoxicity in cerebral ischemia (Lopez-Menendez et al., 2009).

Since MAPK signaling is a major survival pathway and Trk receptors were initially identified as oncogenes (Martin-Zanca et al., 1986), ARMS/Kidins220 has also been suggested as a potential oncogene. Recent studies have been reported the relevance between ARMS/Kidins220 expressions and tumorigenic mechanisms. The overexpression of ARMS/Kidins220 promoted melanoma formation by preventing stress-induced apoptotic death mediated by MEK/ERK signaling pathway (Liao et al., 2007). In addition, the ARMS/Kidins220 might regulate

migration and invasion in metastatic melanoma via activation of MEK/ERK signaling pathway (Liao et al., 2011). Moreover, ARMS/Kidins220 expression was increased in neuroblastoma cell lines and might stabilize NGF-induced survival signaling (Rogers and Schor, 2013a). ARMS/Kidins220 deletion is associated with the neural to Schwann like transition in neuroblastoma cell line model (Roger and Schor, 2013b). However, the molecular mechanisms of ARMS/Kidisn220 have never been investigated in cell proliferation and cell cycle progression.

In this study, we investigated the role of ARMS/Kidins220 in regulating of neuroblastoma cell. We performed to regulate the expression level of ARMS using shRNAi in neuroblastoma cell lines and were explored whether ARMS/Kidins220 regulated cell proliferation via cyclins and CDKs expressions in each cell cycle phase.

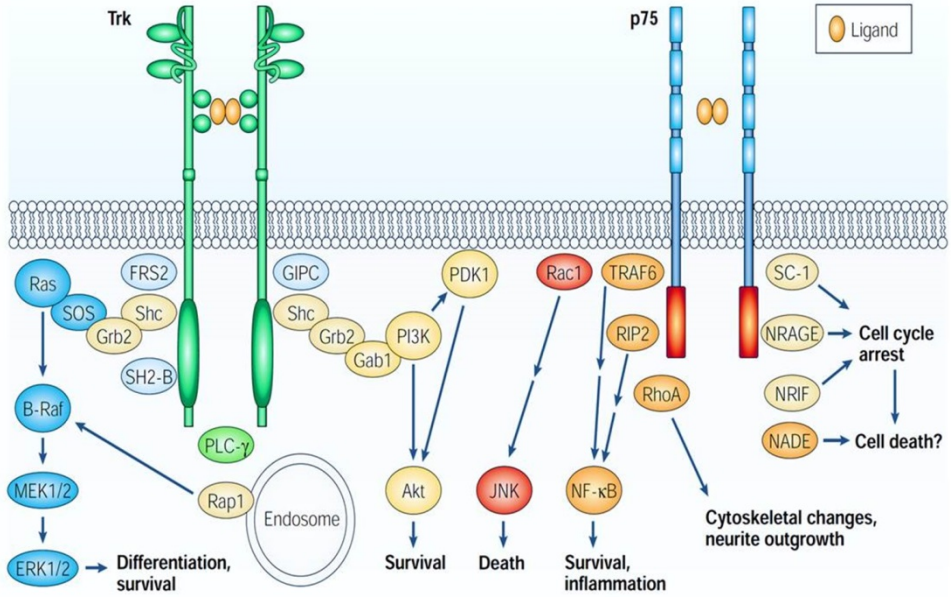

Figure 1. Neurotrophin receptor signaling. Trk receptors mediate differentiation and survival signaling through extracellular signal-regulated kinase (ERK), phosphatidylinositol 3-kinase (PI3K) and phospholipase Cγ (PLC-γ) pathways. The p75 receptor predominantly signals to activate NF-κB and Jun N-terminal kinase (JNK), and modulates RhoA activity. These responses are mediated through adaptor proteins and might exert effects on apoptosis, survival, neurite elongation and growth arrest. (Chao, 2003; Neubrand et al., 2012).

III. Materials and methods

1. Cell culture

Neuro2a mouse neuroblastoma cells were grown in Dulbecco's modified Eagle's medium (DMEM, WelGene, Korea) contained with 10% fetal bovine serum (FBS; Gibco, CA), 10 U/ml penicillin, and 10 g/ml streptomycin at 37°C with 5% CO_2. Antibodies against the C-terminus of ARMS/Kidins220 (clone 892, Kong et al. 2001), cyclin D1, cyclin A, cyclin E, CDK4, ERK, pERK and phospho-pRb (Ser780) (Cell Signaling, MA), CDK2, p21, p16, and α-tubulin (Sigma-Aldrich, CA) were used.

2. Generation of ARMS/Kidins220 short hairpin RNA (shRNA) retroviral vectors and ARMS/Kidins220-knockdown Neuro2a cell lines

Retroviral vectors producing shRNA against ARMS/Kidins220 were constructed by inserting oligonucleotide sequences into pSUPER.puro retro vector (OligoEngine, WA) as previously described (Li et al., 2008; Brummelkamp et al., 2002) (Table 1). Briefly, the pSUPER vector with shARMS sequences was co-transfected with VM-γP and VSV-G plasmids into 293T cells using lipofectamine (Invitrogen, CA) according to the manufacturer's protocol. After 48 h, the culture media containing retroviral supernatants were filtered through a 0.45 μm filter (Satorius, Japan). To increase the concentration of virus stock, the filtered media was ultra-centrifuged at 250,000 x *g* for 1.5 h at 4°C using a Beckman SW26 rotor. After removing the supernatant, the virus pellets in the bottom were resuspended in

a small amount (1% of original volume) of serum-free DMEM. To performing virus titer, we prepared NIH3T3 cells and infected the virus with 10-fold serial dilutions into the cells (antibiotic selection). Virus titer are determined by counting the number of puromycin (2 μg/ml)-resistant colonies at day 5. To construct the control and ARMS/Kidins220-knockdown Neuro2a stable cell lines, Neuro2a cells were infected with the retroviral supernatants containing 4 μg/ml polybrene for 5 hr. For recovery, cells were cultured in DMEM containing 10% FBS for 48 h and then maintained in selection media containing puromycin (2 μg/ml) for next 7 days.

3. Cell proliferation assay

For the cellular growth assay, cells were plated in 24-well plates (5×10^3 cells/well) and counted with trypan blue solution (Gibco, CA) at the indicated time points. The cell proliferation was also measured using EZ-CyTox (Daeil Science, Korea) according to the manufacturer's protocol. Cells were plated in 96-well plates (3×10^3 cells/well), and 10 μl of assay solution were added to each well. Cells were then incubated for 1.5 h at 37°C, and the absorbance was measured by the microplate reader (Bio-Rad, CA) at 450 nm.

4. Fluorescence-activated cell sorting analysis (FACS)

The cell-cycle distribution was measured by flow cytometry using propidium iodide (PI) (Sigma-Aldrich, CA) at indicated times (0, 24, and 48 h).
The cells were trypsinized, washed twice with cold phosphate buffered saline (PBS), and fixed in chilled 70% methanol. Fixed cells were washed twice with PBS, and incubated with 0.1 mg/ml RNase A (Sigma-Aldrich, CA). After then, the cells were

stained with PI (50 μg/ml) for 30 min in the dark (Jadhav et al., 2007). The percentages of cells in each cell cycle phase were measured on a FACS Calibur system (Becton Dickinson, CA), and analyzed with ModFit LT ™ software (Becton Dickinson, CA).

5. Immunoblotting

To synchronize cells in the Go phase, all cells were cultured in serum-free DMEM for 24 h and then stimulated by DMEM containing 10% FBS (0, 4, 8 and 24 h). At each indicated time, the cells were harvested using cell lysis buffer (10 mM Tris-HCl (pH 8.0), 150 mM NaCl, 1 mM EDTA, and 1% NP-40 (TNE buffer) supplemented with the protease and phosphatase inhibitors. Equal amount of proteins (100 μg/lane) were resolved by 6-20% gradient SDS-PAGE, and western blotting was performed with antibodies against different proteins.

6. Statistical analysis

Data were analyzed using Student's t-test and expressed as mean ± standard error of mean (SEM). Probability (P) values < 0.05 were considered statistically significant.

Table 1. Short hairpin RNA interference (shRNAi) oligonucleotide sequences against ARMS/Kidins220.

Direction	Primer sequence
Forward	5'-CACCGCCAGAGAGCAGATCAGTATTCGAAAATACT GATCTGCTCTCTGGC-3′
Reverse	5′-AAAAGCCAGAGAGCAGATCAGTATTTTCGAATAC TGATGCGTCTCTGGC-3′

IV. Results

1. Regulation of neuroblastoma cell proliferation by knock-down of ARMS/Kidins220

The expression of ARMS/Kidins220 in melanoma cells has been shown to confer resistance to UVB-induced apoptosis by activating the ERK signaling pathway (Liao et al., 2007). Although it was reported that ARMS might be a potential oncogene and can effect on tumor cell survival signaling (Liao et al., 2007; 2011), the role by which this protein influences tumor cell proliferation has not been elucidated yet. Thus, in this study, we investigate the role of ARMS/Kidins220 in tumor cell proliferation.

First, we constructed ARMS/Kidins220-knockdown Neuro2a stable cell lines (ARMS-KD) using ARMS-specific shRNA (shARMS)-containing retroviral vectors. The control Neuro2a cells were infected with a virus containing vector alone. Then, by immunoblotting with ARMS antibody (clone 892), we confirmed that ARMS/Kidins220 expression was reduced to 35.9 ± 2% in ARMS-KD cells compared with the control cells (Fig. 2a). Next, we performed a cell proliferation assay using trypan blue staining to investigate whether ARMS/Kidins220 could regulate proliferation. As shown in Fig. 2b, there was no statistical difference in cell growth in cell lines on the first day. However, from the second day, the number of cells in the ARMS-KD group was different from that of the control group. On the fourth day, ARMS-KD cells were numbered 54.9% fewer than the control cells (The control, $24 \times 10^3 \pm 0.24$; ARMS- KD, $13.8 \times 10^3 \pm 0.11$).

According to this data, doubling times of the control and ARMS-KD cells

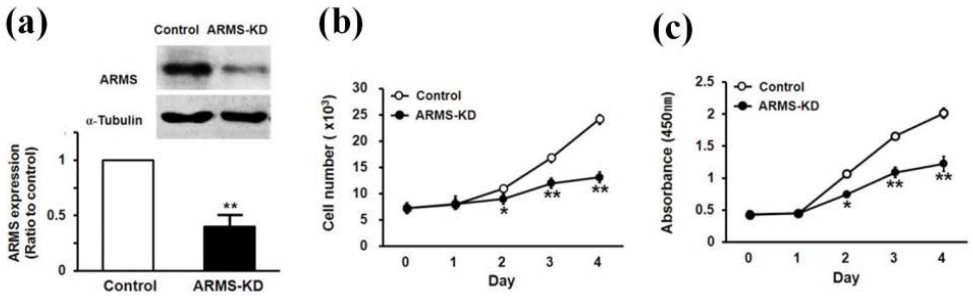

Figure 2. Knock-down of ARMS/Kidins220 decreases Neuro2a cell proliferation. (a) Western blot analysis of Neuro2a cell lysates after shControl and shARMS retroviral infection. To verify the suppression of ARMS/Kidins220, Western blotting was performed with ARMS (892) antibody and alpha-tubulin antibody. (b) Cell counting assay for cell proliferation. Cell proliferation was determined by counting the cell number with trypan blue solution at indicated times. (c) Cell proliferation test using Ez-CyTox solution. The values are represented as the mean ± SEM of three independent experiments, and statistical significance is evaluated by the Student's t-test ($^{*}p < 0.05$, $^{**}p < 0.01$).

were calculated as approximately 1.88 days and 4.26 days, respectively. To confirm this result, we also examined cell proliferation using an EZ-CyTox assay. Consisted with the result of the cell counting assay, ARMS-KD cells showed a decreased proliferation rate compared to the control cells from the second day, with maximal apparent differences on the fourth day (The control, 2.01 ± 0.08 vs ARMS-KD, 1.03 ± 0.07) (Fig. 2c). Taken together, these data indicate that the expression level of ARMS/Kidins220 affects the proliferation of Neuro2a cells.

2. G_1 phase arrest in cell cycle by downregulation of ARMS/ Kidins220

In order to investigate whether ARMS/Kidins220 has a role in cell cycle progression, we analyzed cell-cycle phase progression using fluorescence activated cell sorting (FACS) in the control and ARMS-KD cells (Fig. 3). First, both cell lines were synchronized in the Go phase by serum starvation for 24 h. As expected, both cell lines were showed similar proportions in each cell cycle phase at 0 hr. However, after the addition of serum, the percentages of the control cell group remaining the Go/G_1 phase significantly decreased from 54.2 ± 0.9% to 16.9 ± 2.2%, which indicated the transition from Go/G_1 to S phase in cell cycle. On the other hand, the proportions of ARMS-KD cells in the Go/G_1 phase slightly decreased from 50.0 ± 2.1% to 41.7 ± 0.4% (Fig. 3b). At the same time, the proportion of the control cells in G_2/M phase dramatically increased from 13.9 ± 0.8% to 48.2 ± 5.9%, whereas that of ARMS-KD little increased slightly from

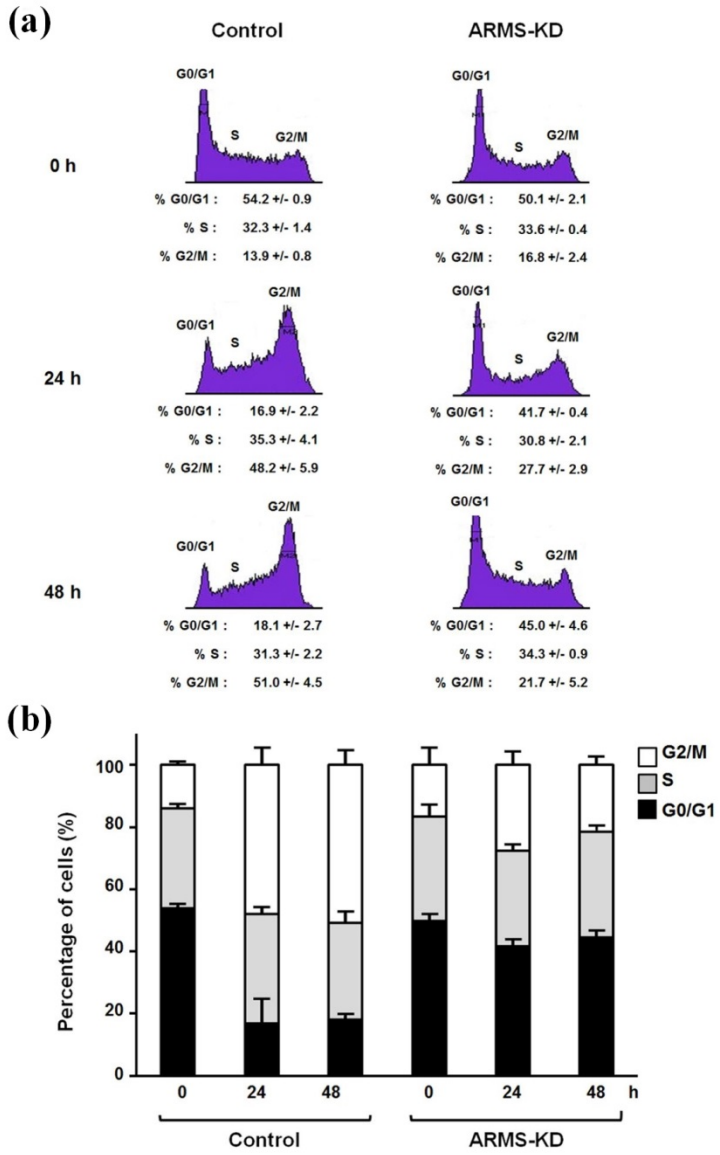

Figure 3. Inhibition of G_1–S phase progression by knock-down of ARMS/Kidins220. (a) FACS analysis shows the distribution of cells in each G_1, S, and G_2/M phase is indicated. (b) The bar graphs indicated the percentage of the cells in G_1, S, and G_2/M phase in the control and ARMS-KD cell lines.

16.8 ± 2.4% to 27.7 ± 2.9% (Fig. 3b). These results suggest that downregulation of ARMS/Kidins220 slows cell cycle in G_1 phase, leading to cell growth inhibition.

3. Reductions of cyclin D1 and CDK4 involved in downregulation of ARMS/Kidins220

Cell growth is regulated by cell cycle regulatory protein, such as such as cyclins and CDKs and D-type cyclins (cyclin D1) are especially important for cell-cycle progression through G_1 phase (Sherr, 1995). Decreased cyclin D1 expression prevents cells from entering S phase, sustaining them in G_1 phase (Baldin et al., 1993). To verify whether downregulation of ARMS/Kidins220 induced G_1 phase arrest through regulatory proteins, we performed Western blotting to examine the expression of G_1 phase regulatory protein, cyclin D1, at different time points of cell cycle progression. As expected, downregulation of ARMS/Kidins220 resulted in significant decreases in cyclin D1 protein levels at 8, 24 and 48 h, compared with the control cells ($p < 0.01$) (Fig. 4). Although there was some decrease in cyclin D1 protein levels at 0 h in ARMS-KD cells, this decrease did not reach statistical significance.

To examine the effects of ARMS/Kidins220-knockdown on the other cyclins, we also analyzed the expression of cyclin E and cyclin A in both cells. Cyclin E is involved in S phase, and cyclin A mainly functions in G_2/M phase (Furuno et al., 1999). In contrast to cyclin D1, there were no significant differences in cyclin E or cyclic A expressions between the control and ARMS-KD cells (Figs. 4a, 4c, and 4d).

Interestingly, even at 0 h, without cell-cycle progression, the CDK4 protein level was significantly decreased in ARMS-KD cells. The expression of CDK2, a binding partner of cyclin E and cyclin A, was similar in both cell lines

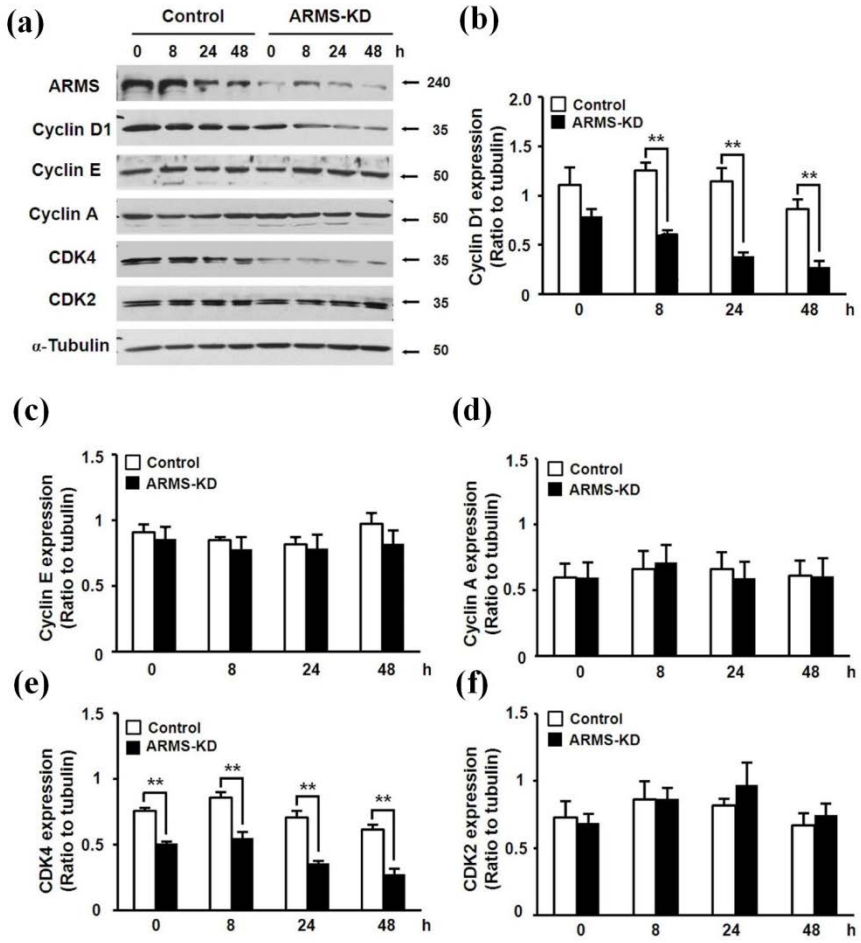

Figure 4. Decrease of cyclin D1 and CDK4 by knock-down of ARMS/Kidins220. (a) Western blot analysis of cyclins and CDKs in the control and ARMS-KD cell lines (cyclin D1, cyclin E, cyclin A, CDK4, and CDK2). (b-f) Band intensities from three independent experiments were analyzed and normalized to alpha-tubulin. The values are mean ± SEM and statistical significance was evaluated by Student's t-test ($^{*}p < 0.05$, $^{**}p < 0.01$)

(Fig. 4f). These results indicate that knockdown of ARMS/Kidins220 is associated with the decreased expressions of cyclin D1 and CDK4 in G_1 phase but has no effect on other cell cycle regulatory proteins.

4. Inhibition of hyperphosphorylation of pRb via reduction of cyclin D1 and CDK4 by downregulation of ARMS/Kidins220

To examine whether expression levels of cyclin D1 and CDK4 influence the downstream pRb pathway, we performed Western blotting with a phospho-pRb (Ser780) antibody, which specifically binds to CDK4-phosphorylated pRb. Generally, cyclin-dependent kinases (CDKs) are activated by binding of a G_1 phase cyclin followed by hyper-phosphorylation of Rb (ppRb) and progression into S phase (Sherr et al. et 1995; Chen et al., 1989; Jiao et al., 2006). As expected, the level of hyper-phosphorylated pRb (ppRb) was decreased in ARMS-KD cells compared with the control cells at 24 h. Until 8 h after stimulating, the levels of ppRb in both cell lines were no different, however, at 24 h, ppRb in the control cells significantly increased than that in ARMS-KD cells. This data indicated that reduction of cyclin D1 and CDK4 decreases pRb phosphorylation, which result in phase arrest in G_1 cell cycle (Figs. 5a-d). Traditionally, the other proteins groups, which could regulate cell cycle, are called cyclin dependent kinase inhibitors (CKIs), representatively p16, p17, p19, and p21. In this study, we focused on p21 and p16, which regulate cyclin dependent kinase in G_1/S transition. The p21 is involved in regulating the function of cyclin D1/CDK4 and cyclin E/CDK2 complexes (El-Deiry et al., 1993; Harper et al., 1993; Xiong et al., 1993a).

As another CKI protein, p16 was known to specially inhibit the function of

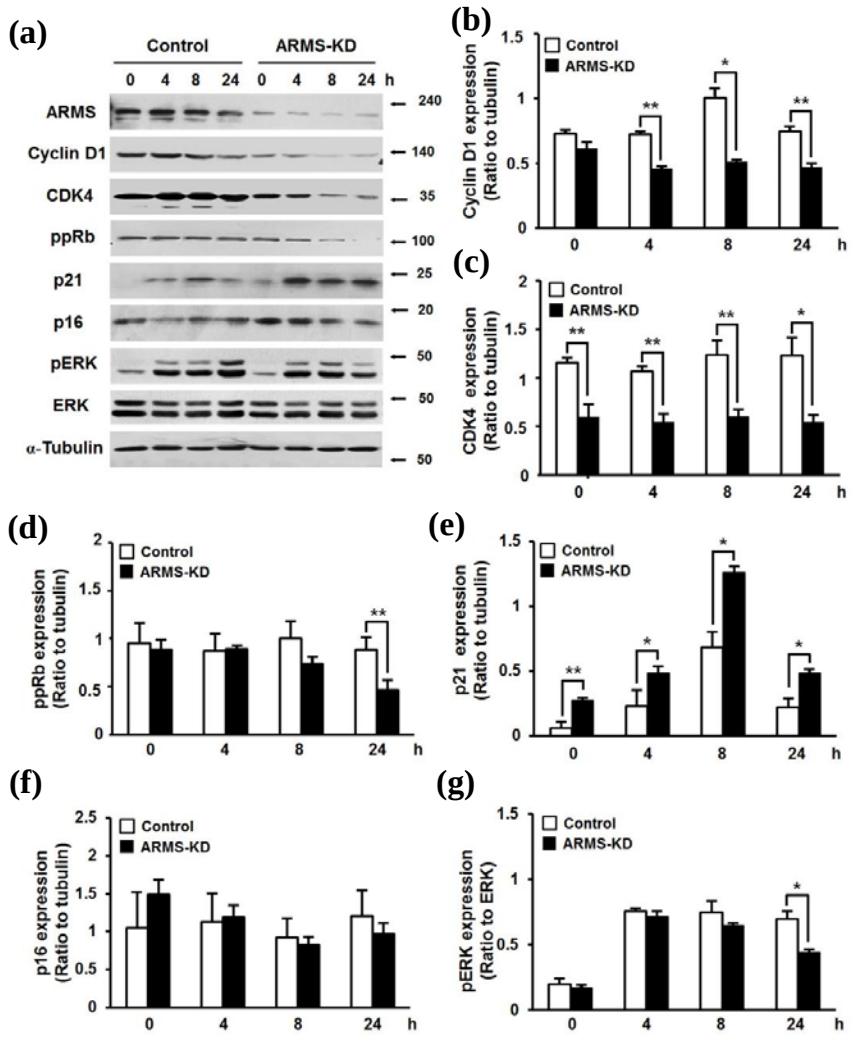

Figure 5. Reduction of ppRb via alteration of cyclin D1, CDK4, and p21 by knock-down of ARMS/Kidins220. (a) Western blot analysis of cyclin D1, CDK4, ppRb, p21, p16, pERK and ERK in the control and ARMS-KD cells. The loading the control is alpha-tubulin. (b-g) The bar graphs show the changes in cyclin D1, CDK4, ppRb, p21, p16, pERK and ERK during cell cycle progression in the control and ARMS-KD cells. Band intensities from three independent experiments

were analyzed and normalized to alpha-tublin. The values are mean ± SEM and statistical significance was evaluated by Student's t-test ($^{*}p < 0.05$, $^{**}p < 0.01$).

cyclin D1/CDK4 in G_1 phase (Bates et al., 1994; Xiong et al., 1993b). At all-time-points in our experiment, the levels of p21 protein in ARMS-KD cells was significantly higher than that in the control cells (Fig. 5e). In contrast, we did not observe any significant differences in p16 between the two cell lines (Fig. 5f). These results indicate that knockdown of ARMS/Kidins220 upregulates p21 protein expression, thus inhibiting cyclin D1/CDK4 function in G_1 phase of cell cycle. Next, we examined the activation of the p42- and p44-kDa extracellular signal regulated kinases (ERKs) in ARMS-KD cells since ARMS/Kidins220 was shown to act as a platform for sustained Erk activation in neurons through the recruitment of CrkL (Arevalo et al., 2004; 2006) and ARMS/Kidins220-knockdown downregulates ERK activity in melanoma cells (Liao et al., 2007; 2011).

Consistent with previous studies, the level of pERK protein in ARMS-KD cells was decreased at early time points compared with the control cells, especially at 60 min ($p < 0.05$) (data not shown). We also the level of pERK protein in ARMS-KD cells was significantly decreased at 24 h compared with that in the control cells ($p < 0.05$) (Figs. 5a and g). Taken together, our results suggest that downregulation of ARMS/Kidins220 inhibits neuroblastoma cell-cycle progression at G_1/S check point through the upregulation of p21 protein (Fig. 6).

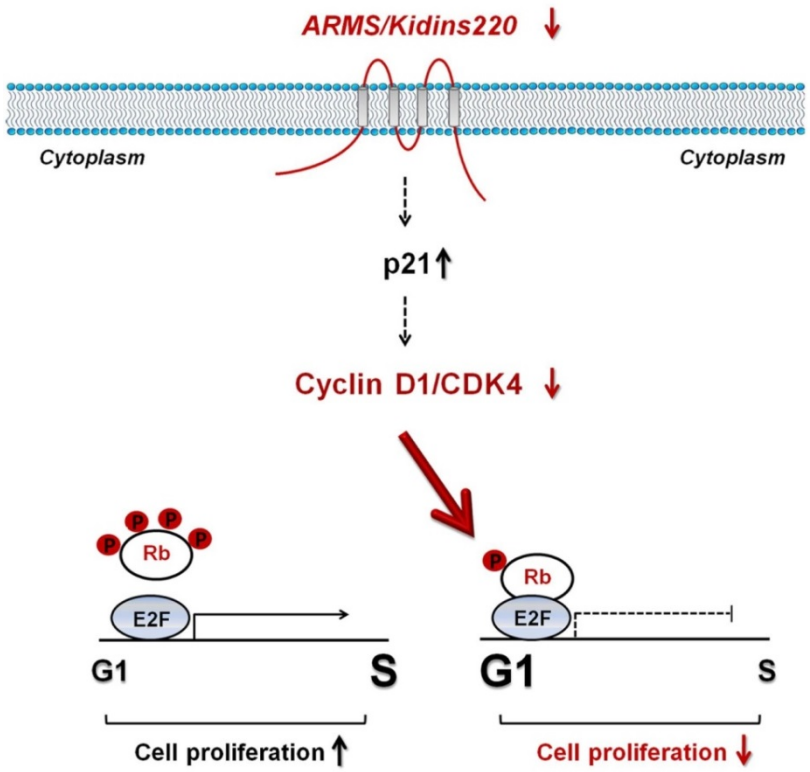

Figure 6. Diagram depicting how ARMS/Kidins220 regulates cell cycle progression. Knock-down of ARMS/Kidins220 controls cell proliferation rate and reduces the cyclin D1 and CDK4 in G_1 phase. Moreover, knock-down of ARMS is involved in upregulation of p21, leading to inhibit cell proliferation. Inhibition of cyclin D1 and CDK4 could result in hypo-phosphorylation of pRb family proteins and subsequent sequestration of E2F transcription factors. The transcriptional activation of E2F-responsive genes is essential for DNA synthesis and cell cycle progression. Taken together, our results suggest that reduction of ARMS expression is able to induce the expression of p21, leading to inhibition of cyclin D1 and CDK4, and reducing pRb phosphorylation.

V. Discussion

ARMS/Kidins220 is a transmembrane protein with four membrane-spanning domains and is consisted of 11 ankyrin repeats, a polyproline region, and a SAM domain as well as the C-terminal PDZ-binding sites (Kong et al, 2001; Arevalo et al., 2006 ; Neubrand et al., 2012).

ARMS/Kidins220 is highly expressed in the nervous system and has important roles in neuronal differentiation, survival and development via its various domains for protein-protein interactions (Iglesias et al., 2000; Kong et al., 2001). Thus, several research groups have studied the structure and interactions with receptor complexes and determined effects in various mechanisms (Chao, 2003; Neubrand et al., 2012).

Recently, ARMS/Kidins220 expression is highly increased in human melanoma compared to benign skin lesions, and prevents stress-induced apoptosis in melanoma cells by activating ERK pathway (Liao et al., 2007). Moreover, it has been reported that ARMS/Kidins220 regulate phosphorylation of MAPK, resulted in neuronal cell death by mediate excitotoxicity in cerebral ischemia (Lopez-Menendez et al., 2009). In addition, the roles of ARMS/Kidins220 in physiological functions have been reported in the vascular and nervous systems (Cesca et al., 2012) but the mechanisms have not been clearly elucidated. Similar to Trk receptors as oncogenes, ARMS/Kidins220 might have a critical role involved in regulating of tumorigenesis (Martin-Zanca et al., 1986; Liao 2007; 2011). Although ARMS/Kidins220 is involved in tumor cell survival and contributes to tumor

progression, its role in cell proliferation and cell-cycle progression has never been investigated.

Generally, the oncogenes might have functions to increase cell-proliferation by stimulating cell cycle progression. As a tumor suppressor, pRb inhibits cell cycle progression at G_1/S by blocking the activity of the E2F family of transcription factors, which activate the genes required for induction of S phase (Dulic et al., 1994). Rb function is regulated through cell cycle by phosphorylation (Chen et al., 1989). Hyperphosphorylation of pRb by cyclin-CDK complexes in G_1 phase inactivates its growth suppression function; consequently, G_1 restriction point is bypassed (reviewed in Malumbres and Barbacid, 2009).

In this study, ARMS/Kidins220-knockdown induced the cell growth rate slow down and regulated cell cycle via sustaining in G_1 phase. The downregulation of ARMS/Kidins220 was associated with the decreased expressions of cyclin D1 and CDK4 in G_1 phase. The expressions of other regulatory proteins such as cyclin A, -E, and CDK2 were not changed. Cyclin D1 is often overexpressed and associated with tumorigenesis in many cancers and loss of cyclin D is sufficient to cause G_1 arrest in other cellular contexts (Masamha and Benbrook, 2009). Cyclin D1/CDK4 level was significantly decreased in ARMS-KD cells and was tightly associated with p21 upregulation in our experiment. In contrast, p16, another of CKIs, was unchanged. Indeed, the level of ppRb was also reduced in ARMS-KD cells than the controls at 24 hr after the cell-cycle entry.

Consistent with previous studies, we also found that pERK level was reduced after ARMS/Kidins220 knockdown (Arevalo et al., 2004; Liao et al., 2007; 2011). Since ARMS/Kidins220 mediates prolonged MAPK signaling by interacting

with CrkL (Arevalo et al., 2004; 2006), it will be interested to examine which adaptor(s) or effector(s) is involved in ARMS/Kidins220-p21 pathway of cell cycle regulation. Identifying the specific domain of ARMS/Kidins220 involved in the regulation of p21 expression using the serial deletion constructs of ARMS/Kidins220 will be useful to further delineate this pathway. Another interesting question to address will is be whether ARMS/Kidins220 is also involved in other tumor cells and normal cell proliferation by the same mechanism demonstrated in our study. Although the role of p21 is still controversial, it is clear that p21 inhibits cyclin D1/CDK4, which results in retarded cell proliferation in this study.

In summary, we demonstrated that ARMS/Kidisn220 regulates neuroblastoma cell proliferation by regulating cyclin D1/CDK4, resulting in upregulation of p21 proteins. Therefore, our results suggest that ARMS/Kidins220 acts as an important platform for organizing the signaling complex to regulate cell cycle progression in response to extracellular stimuli and may serve as an important prognostic factor of tumors in the nervous system.

CHAPTER III.

Sorting of human mesenchymal stem cells by applying multi-branched microfluidic chip

Parts of the data shown in this thesis have been published in

Analyst 2015 140: 1265-1274

I. Abstract

Human mesenchymal stem cells (hMSCs) have the ability to replicate self-renewal and to differentiate into multiple cell types that allow them to use tissue engineering and cell therapy. Recent studies have reported that the MSCs consist of heterogeneous populations with variable morphology, making a limited capacity for self-renewal, and less efficiently differentiated (multipotent properties). Thus, to getting the purified hMSCs with high potential is important step for increasing the efficiency of stem cell therapy.

Here, we have sought to develop and validate a novel method to collect a desired size of hMSCs by microfluidic chip with the hydrodynamic filtration (HDF) principle. HDF is a principle which is similar to cross flow filtration which utilizes small capillary branches perpendicular to the main flow. When a particle is flowing in a microchannel, the center position of the particle cannot be present in a certain distance from sidewalls, which is equal to the particle radius.

Using this multibranched channel, we conducted the separation of hMSCs and fractionate the cells into three subpopulations, i.e., small, rapidly self-renewing (RS) (< 25 μm), spindle-shaped (SS) (25-40 μm), and large, flattened (FL) (> 40 μm) cells. The results obtained in this study demonstrate high purity (> 86%) and successful recovery (> 80%) of each group of cells. Through verify surface marker expressions (CD73, CD90 and CD105) of collected cells in each outlet, the RS and SS cells show high levels of CD73, CD90 and CD105 while, FL cells do not show any the expression of CD73. In addition, to investigate the sorted population's multipotency potential, we performed adipogenic, osteogenic, and Schwann cell

differentiations and then compared the multilineage potentials of each subpopulation. From comparing the expressions of the marker genes in each group, we determined that the marker genes expressions involved in differentiations in RS and SS populations had significantly increased than in FL group cells. In addition, RS and SS groups had higher differentiation potential than the unsorted populations because they contained FL cells with lower potential. These results indicate that the HDF multi-branch chip successfully sorted hMSCs based on size, and that cell size appears to be closely related to multipotency and can serve as an indicator of differential potential.

II. Introduction

Human bone marrow-derived mesenchymal stem cells (hMSCs) have been considered as a cell therapy for regenerating of damage tissues or various diseases and applied for tissue engineering. They could divide of self-renew and have potentials to differentiate into cell with adipocyte in the ectoderm, osteoclast in the mesoderm and trans-differentiation endoderm such as epithelial cells and neurons (Pitternger et al., 1999; Colter et al., 2001; Pinney and Prockop, 2007; Sherman et al., 2011). Although these hMSCs are eligible for these medical applications, there are still potential limitations.

There have been reported that hMSCs consist of heterogeneous subpopulations of stem cells, which have different self-renewal ability and multipotent potentials (Smith et al., 2004; Haasters et al., 2009). First, they have been classified into small rapidly self-renewing cells (RS), elongated, spindle-shaped cells (SS), and slowly replicating, large, flattened cells (FC) based on the size. Moreover, smallest RS cell populations have been shown to have the highest multipotency to differentiate into various cell types, while large FC cells are regarded to be very early osteogenic progenitors with subsequently losing stem cell characteristics. Thus, sorting these stem cells based on their size and concentrating target populations with high multipotency are important to increase the effectiveness of cell therapy. There have been many researches for manipulation and sorting of cells in biomedical applications such as cell biology, clinical diagnostics, and oncology Fu et al., 1999; Nilsson et al., 2009; Gao et al., 2013; Primiceri et al., 2013). Thus, getting purified cell samples from different group is

very important and basic step for studying their biological and physical properties. Traditionally, cell sorting and separation is achieved by FACS and MACS. Both methods have high quality sorting efficiency and achieve high throughput but required inevitable, irreversible, labeling steps with specific antibodies with high cost and further experiments restriction and need for high cost complicated device with well training operation skills. These factors could be restriction points to sorting experiments (MacDonald et al., 2003; Schneider et al., 2010).

Microfludidics and microfabrications could be shown the alternative methods to these traditional sorting systems and recent studies have reported that manipulate particles and living cells (Hyun et al., 2013). There are classified into two separation principles, active separation and passive separation. The active separation is applied for microfluidics with external fields factors, such as magnetophoresis, dielectrophoresis, and optical method (MacDonald et al., 2003; Schneider et al., 2010). These methods were considered for increasing sorting efficiency but results in high costs production and complicated device designs. Instead, the passive separation sorting methods used the barriers of channel obstruction pattern, hydrodynamic effect or the combinations of both within a microfluidic device achieve separation, respectively.

Specially, hydrodynamic effects understand the flow profile and interaction in microfluidic channel to obtain separation based on the inertial force (Di Carlo et al., 2007; Aota et al., 2011), pinched flow (Kawamata et al., 2008) and HDF (Stone et al., 2004; Yamada et al., 2007; Bruus, 2008; Sugaya et al., 2011). Using HDF principle, mid-2000, Seki groups introduced a microfluidic chip with multiple branched channels for particles and cells and have made effort to increase the

sorting efficiency. The particles or cells are injects through main inlets and aligned into the wall by side supporting flow. Then there are occurred the selective flow fractionation along to side branched channel and determined the flow distributions relative to the hydraulic resistances. By these HDF, they performed various cells separation experiments, such as liver cells, white blood cells (WBC) from red blood cells (RBC), JM cells (human T-lymphocyte cell line), and HeLa cells (human epithelial tumor cell line) (Stone et al., 2004; Yamada et al., 2007; Bruus, 2008).

The basis of flow-based HDF is implemented from conventional crossflow filtration which employs numerous capillary branches perpendicular to the main flow. HDF is relatively simple and approachable for continuous separation of particles or cells without chemical treatments and external fields, compared to many recent flow-based separation methods. By the mechanism called particle focusing, the branches manage to remove the medium and align particles to the sidewalls of the main channel (Yamada et al., 2005; Lenshof and Laurell, 2010).

In this study, we applied a microfluidic chip with HDF for sorting populations from heterogeneous hMSCs populations not targeting a specific size cells from unrelated, arbitrary crowds. First of all, unlike previous studies, we clarified the analogy of pressure-driven laminar flow in microfluidic networks and intended trimodal separations subjected to the possible classification of hMSC with three fractions. Multi-branches connected to main channel are effective in removing excess fluid gradually, aligning of the cells eventually along the main channel walls.

The cells were injected through main inlet and moved into the side branches by side flow, according to the focusing with a proper ratio between main and side flow rates. Then, the cells are sloped the branch channels with 60º, which is in

parallel to the direction of side inlet for focusing. According to the focusing with a proper ratio between main and side flow rates, cells were move into the side branch by side flow. To estimate the sorting efficiency of our designed chip, we analyzed efficiency, the recovery ratio of different outlets for each fraction and the purity of each fraction at different outlets. Our results demonstrated the validity of microfluidic chip filtration and showed its possible application to the rapid and precise fractionation of hMSCs with high multipotency.

Fig. 1 represents size-selective separation enabled by flow focusing effect caused by flow fraction between main and branch stream. In other words, with proper the control of flow fraction, some particles with hydrodynamic centers in the branch stream region are diverted into branch channel and other particles flow along the main stream. The width of the gray-colored region in Fig. 1 denotes the virtual boundary of the fluid layer is termed as cut-off width (Wc), which is a key factor to determine size of particles to be diverted into the branches. Here, we assume that particles continuously flow through the channel in full width. In the straight main channel after entrance length, $L/r_h = 0.1\mathrm{Re}r_h$, since $L >> L_0$, the flow is reasonably assumed to be fully developed flow in most of the channel, where L is the channel length, r_h is the equivalent hydraulic radius, and Re means Reynolds number. Hence, the analysis of flow fraction of two streams is essential to HDF principle. In this study, the suspending fluid without feed material is supplied from the side channel flow to a certain angle, where we carefully chose as 60º.

The flow fraction of main and side streams is analytically examined from derivation of the flow ratio between two streams. Considering the shape of microchannel, our present model takes into account the 3-dimensional flow profile

at the rectangular cross-section with arbitrary aspect ratio.

As we assume the medium as a Newtonian fluid and fluid flows as steady state laminar flow in a straight channel, the governing equation is given by Stokes equation, $\mu\nabla^2\mathbf{v} = \nabla P$. For rectangular microchannel with the width *W* and the height *H*, the governing equation becomes

$$\frac{\partial^2 v_z}{\partial x^2} + \frac{\partial^2 v_z}{\partial y^2} = \frac{1}{\mu}\frac{dP}{dz}. \tag{1}$$

Here, v_z is the streamwise axial velocity in *z*-direction, *P* is the pressure drop applied along the channel length, and μ is the fluid viscosity.

The analytical solution for *v* with no-slip boundary condition is given by (Yamada et al., 2007)

$$v_z(x,y) = \frac{4H^2}{\pi^3\mu}\frac{\Delta P}{L}\sum_{n=odd}^{\infty}\frac{1}{n^3}\left[1-\frac{\cosh(n\pi x/H)}{\cosh(n\pi W/2H)}\right]\sin(n\pi y/H). \tag{2}$$

The streamwise average velocity is obtained by integrating Eq. (2) with respect to the *y*-direction,

$$\overline{v}_z(x) = \frac{1}{H}\int_0^H v_z(x,y)\,dy = \frac{8H^2}{\pi^4\mu}\frac{\Delta P}{L}\sum_{n=odd}^{\infty}\frac{1}{n^4}\left[1-\frac{\cosh(n\pi x/H)}{\cosh(n\pi W/2H)}\right]. \tag{3}$$

Further, the average velocity in the channel is obtained by integrating Eq. (3) along the spanwise *x*-direction,

$$\overline{v}_z = \frac{2}{W}\int_0^{W/2}\overline{v}_z(x)\,dx$$

$$= \frac{H^2}{12\mu}\frac{\Delta P}{L}\left[1-\frac{192}{\pi^5}\frac{H}{W}\sum_{n=odd}^{\infty}\frac{1}{n^5}\tanh(n\pi W/2H)\right] \tag{4}$$

where $\sum_{n=odd}^{\infty} n^{-4}$ equals to $\pi^4/96$ by the Riemann zeta function.

Then, the volumetric flow rate Q is described by the hydraulic resistance R such that

$$Q = \frac{WH^3}{12\mu}\frac{\Delta P}{L}\left[1-\frac{192}{\pi^5}\frac{H}{W}\sum_{n=odd}^{\infty}\frac{1}{n^5}\tanh\left(n\pi W/2H\right)\right] = \frac{\Delta p}{R}. \quad (5)$$

Further, we subdivide the main channel stream and set the focused stream of $-X \le x \le 0$ (or $0 \le x \le X$, due to symmetry) with $X = W/2 - W_C$, for detailed analysis of flow streams. The fractional flow rate, Q_x, for the focused stream is derived as

$$Q_X = \int_0^X \int_0^H v_z(x,y)\,dy\,dx$$

$$= \frac{WH^3}{24\mu}\frac{\Delta P}{L}\left[\frac{2}{W}X - \frac{192}{\pi^5}\frac{H}{W}\sum_{n=odd}^{\infty}\frac{1}{n^5}\frac{\sinh\left(n\pi X/H\right)}{\cosh\left(n\pi W/2H\right)}\right]. \quad (6)$$

In Fig. 2, the virtual boundary is observed in the forefront of the initial branch point where main and side streams merge. The width of this virtual boundary can be mathematically predicted from a proportion of two streams. Our previous study has defined the ratio of flow rates of two streams as the ratio of flow fraction, ξ (Jung et al., 2015). By employing the relationship of total flow rate and fractional flow rate, $Q_i^m + Q_i^S = Q$ and $Q_i^m + Q_x = Q/2$, ξ can be expressed as

$$\xi \equiv Q_i^m / Q_i^s = \left(Q - 2Q_X\right)/\left(Q + 2Q_X\right). \quad (7)$$

The equation above is rearranged with $\Gamma_1 = \tanh(n\pi W/2H)$, $\Gamma_2 = \cosh(n\pi W/2H)$, and $\Gamma_3 = \sinh(n\pi X/H)$ and rewritten as

$$\xi \equiv \frac{Q_i^m}{Q_i^s} = \frac{1 - 2X/W - \left(192/\pi^5\right)\left(H/W\right)\Sigma_{n=odd}^{\infty}\left[n^{-5}\left(\Gamma_1 - \Gamma_3/\Gamma_2\right)\right]}{1 + 2X/W - \left(192/\pi^5\right)\left(H/W\right)\Sigma_{n=odd}^{\infty}\left[n^{-5}\left(\Gamma_1 + \Gamma_3/\Gamma_2\right)\right]}. \quad (8)$$

To achieve trimodal separation from the hMSC populations, our microfluidic chip is designed to have three outlets as shown in Fig. 3. The hMSCs in certain range enter the corresponding branches where the ratio of flow fraction is optimized for the specific size. The sorting can be improved with proper the control of the ratio of flow fraction for each branch channel. In steady state flow, we observe the parabolic velocity profile, or fully-developed flow at the distance of approximately $0.1\mathrm{Re}r_h$ from the node of main and side channels. After this distance, the streamline becomes parallel to the main channel and laminar flow is then observed. Branches are constructed from this point forward and for more accurate design we have divided the main channel into the number of branch points, as marked in Fig. 1. The branch point, S_b, is significant since the complex input fluid begins to diverge into two streams: optimized amount of flow enters the branch channel and the rest remains in the main channel. At this point, the ratio in Eq. (8) is equivalent to the ratio of flow rates in branch and main streams at specific *j*th branch point S_j.

$$\left.\frac{Q^b}{Q^m}\right|_{S_j} = \frac{1-2X/W-\left(192/\pi^5\right)(H/W)\sum_{n=odd}^{\infty}\left[n^{-5}\left(\Gamma_1-\Gamma_3/\Gamma_2\right)\right]}{1+2X/W-\left(192/\pi^5\right)(H/W)\sum_{n=odd}^{\infty}\left[n^{-5}\left(\Gamma_1+\Gamma_3/\Gamma_2\right)\right]}. \qquad (9)$$

The number of terms required for sufficient accuracy is subject to H/W and W_C. Here, the equation converges with less than 4 terms (i.e., n = 1, 3, 5).

From Eq. (5) with rapidly converging sum, the flow rate at the main channel between branch point *j*-1 and *j* can be given as

$$Q^m_{j-1,j} \equiv \frac{\Delta P^m_{j-1,j}}{R^m_{j-1,j}} = \frac{WH^3}{12\mu}\frac{\Delta P^m_{j-1,j}}{L^m_{j-1,j}}\left[1-\frac{192}{\pi^5}\frac{H}{W}\tanh\left(\pi W/2H\right)\right]. \qquad (10)$$

Since the corresponding flow rate $Q^m_{j-1,j}$ is represented by subtracting output flows at branches from 1st to (j-1)th from the total input flow Q, the pressure drop at the corresponding interval is estimated as

$$\Delta P^m_{j-1,j} = R^m_{j-1,j}\left(Q - \sum\nolimits_1^{j-1} Q^b_j\right). \quad (11)$$

The first 48 branch channels and next 7 channels deviated from the main channel are connected to outlet 1 and outlet 2, respectively, where the main channel connects inlet 1 and outlet 3 with an invariant width.

All branches are slanted to the angle of 60º which is parallel to the side stream. This geometry is determined from our preliminary study which has resulted in higher efficiency in slanted channel than perpendicular configurations (Jung et al, 2015). Branches connected to both outlet 1 and 2 are composed of multiple channels for effective separation of particles. The design of multiple branches is responsible for aligning against sidewalls and concentrating the particles by fluid removal, providing the separation enhancement. Branches are designed to have two parts: a narrow section and a wide section. Yamada and Seki suggested that specifying the narrow and wide section allows keeping the total length of branch channels uniform by adjusting the hydrodynamic resistance properly (Yamada et al., 2005). The narrow section exists for practical application of pressure drop, and the wide section works as a reservoir with a relatively broadly width to prevent the reverse flow in the process of particle discharge. Branch channels are designed to consist of narrow and wide segments that make the total lengths of the channels uniform by adjusting their hydraulic resistances to specific values. Thus, the flow rate at the j-th branch channel is given by

$$Q_j^b \equiv \frac{\Delta P_j^b}{R_j^b + R_j^{bR}} \tag{12}$$

where the hydraulic resistances for each section are arranged in series, expressed as

$$R_j^b = \frac{12\mu L_j^b}{W_j^b H^3}\left[1 - \frac{192}{\pi^5}\frac{H}{W_j^b}\tanh\left(\pi W_j^b / 2H\right)\right]^{-1}, \tag{13}$$

$$R_j^{bR} = \frac{12\mu L_j^{bR}}{W_j^{bR} H^3}\left[1 - \frac{192}{\pi^5}\frac{H}{W_j^{bR}}\tanh\left(\pi W_j^{bR} / 2H\right)\right]^{-1}. \tag{14}$$

Table 1 suggests the design parameters we have used in this study. In hydrodynamic filtration, the virtual boundary width is considered as W_C. If the hydrodynamic center of particles is located in this width, colored in white in Fig. 1, those particles will be diverted into the following branches and vice versa; thus, objective particle size primarily determines the cut-off width. The targeted parameters in chip design calculation are lengths of narrow section of each branch channel and length between the last branch and outlet 3. We set the heights and the widths of main as well as branch channels, total lengths of main and branch channels, and inter-distances between each branch channel.

Objective parameters are each length of individual branch channels and the length between the last branch and outlet 3. The pressure drops between inlet and every outlet point are set to equal on the ground that the main and all branch channels are open to the atmosphere, yielding

$$\Delta P_{i,1} = \cdots = \Delta P_{i,j} = \cdots = \Delta P_{i,O3} \quad . \tag{15}$$

Note that the pressure drop is basically described as the product of the flow rate and hydraulic resistance. From Eqs. (9)-(15), $\Delta P_{i,1}$ is first calculated with the initial

guess of L_1^b, and then for that specific pressure drop value, L_j^b is repeatedly computed by iteration scheme on the condition of $\Delta P_{i,1} = \Delta P_{i,j}$ in the multiple branches. Sufficient minimum tolerance is acknowledged in the nonlinear regression with the least sum of squares method based on generalized reduced gradient (GRG) scheme. Similarly, the length between the last branch and outlet 3 ($L_{55,O3}^m$) can be determined by iteration scheme on the condition of $\Delta P_{i,1} = \Delta P_{i,O3}$.

The configuration of the microfluidic chip is shown in Fig. 2. The chip consisted of two inlets from main and side channel and fifty five branch channels connected to three outlets reservoirs (Fig. 3). The first forty eight branch channels were connected to outlet 1, each of which was composed of narrow and broad segments, with properly adjusted flow resistances. The next five branches are connected to outlet 2 and others are subjected to outlet 3. The slanted branch channels are directed to 60º to the main channel and the length between $L_{i,1}^m$ and b_1 is 2,000 μm long to help the fluid reach steady state. The dimensions of each microchannel are set to 90 μm (width) x 65 μm (height) x 2.3 cm (length) (Table 1).

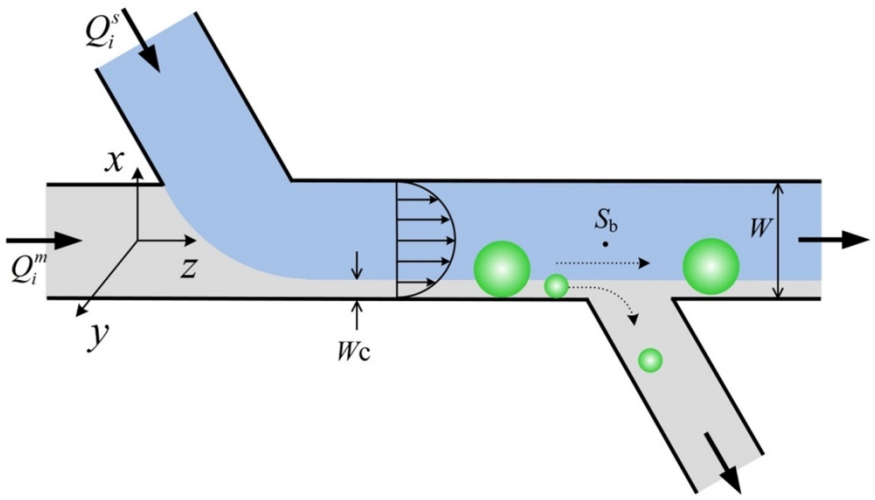

Figure 1. Schematic of the flow fraction of HDF of particles in microchannel with a branch, on the basis of the cut-off width of fully-developed flow stream.

Table 1. Design parameters and values of multibranched sorting chip.

Channel	Dimension		Notation	Values (μm)
Main	Height		H	65
	Width		W	90
	Length		$L_{i,1}^{m}$	440
			$L_{j-1,j}^{m}$ (j = 1-48)	280
			$L_{j-1,j}^{m}$ (j = 49-55)	280
			$L_{55,O3}^{m}$	1140
	Cut-off		W_{C1}	12.5
			W_{C2}	20
Branch	Height		H	65
	Total length		L_{j}^{bT} (j = 1-48)	30000
			L_{j}^{bT} (j = 49-55)	1000
	Width	Narrow section	W_{j}^{b} (j = 1-48)	54
			W_{j}^{b} (j = 49-55)	75
		Wide section	W_{j}^{bR} (j = 1-48)	90
			W_{j}^{bR} (j = 49-55)	105
	Length	Narrow section	L_{j}^{b}	to be computed
		Wide section	L_{j}^{bR}	to be computed

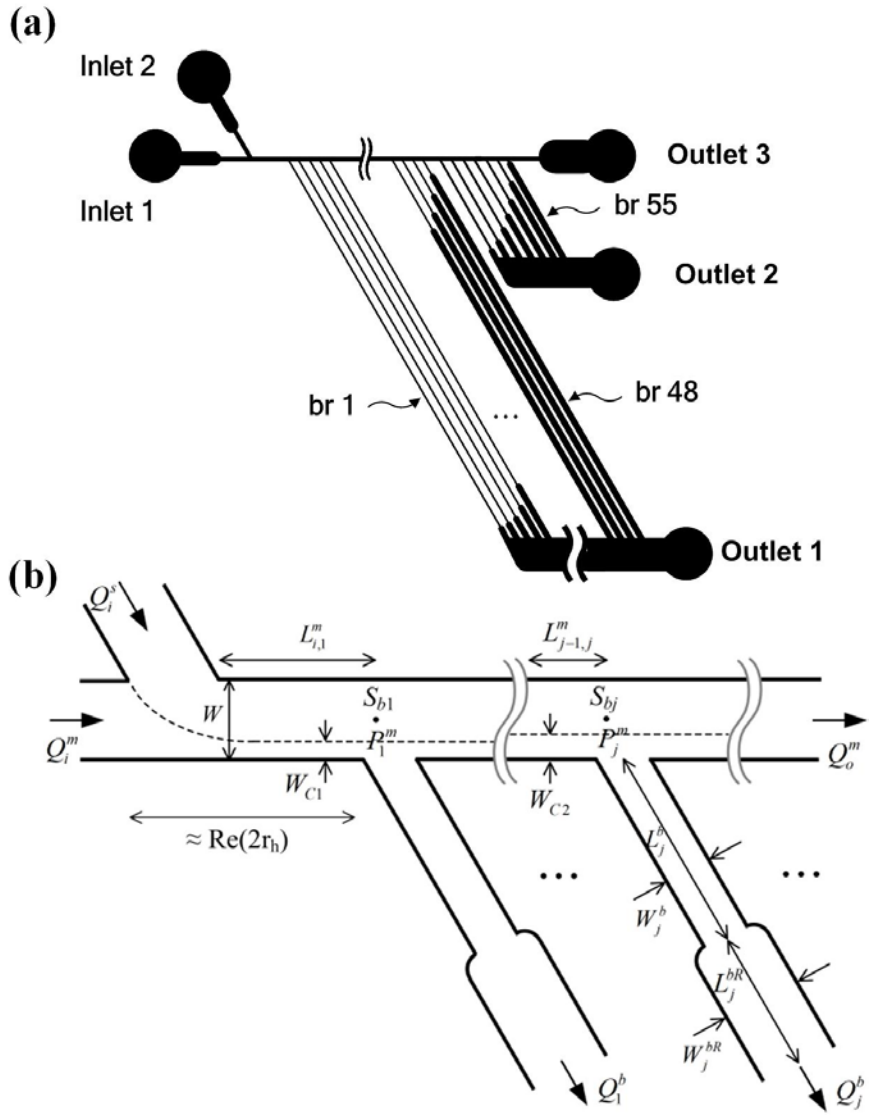

Figure 2. The HDF and multi-channel network in the sorting chip. (a) Schematics of HDF microfluidic chip for sorting of particles and hMSCs, and (b) multi-channel network for analysis and design.

III. Materials and methods

1. Sorting chip fabrication

The microfluidic chip were fabricated the microfluidic chip designed with all values of channel dimension (shown in Fig. 2 and Table 1). All procedures were followed by the standard soft lithography protocols (Yoo et al, 2014). Channel design was performed with AutoCAD-2009 (Autodesk Inc.) and the photomask was prepared for the fabrication of a master mold on a silicon wafer (boron doped, p-100). In order to create the master mold, the photolithography was employed with the negative photoresist (PR) SU-8 2050 (Microchem, Newton, MA) which coated onto the cleaned wafer by spinning. After UV (wave length = 365 nm) patterning by the mask on the PR for 10 sec with the mask aligner (MA-6 mask aligner, 128.6 mJ/cm^2), the post exposure bake was carefully performed and then the unexposed PR was removed by dissolving with the SU-8 developer (Microchem, Newton, MA). For PDMS replica with the designed patterns, Sylgard 184 (Dow Corning, MI) silicon elastomer prepolymer was mixed in 1:10 ratio with curing agent and pouring on onto the molding master. After sufficient degassing, the PDMS layers with mold were baked at 80^oC for 1 h. The cured PDMS replicas were peeled off and the holes were punched for two inlets and three outlets by 1.6 inch puncher. Prepared PDMS replicas were bonded to the glass substrate followed by O_2 plasma treatment (70 W, 40 sec, CUTE-1MP, FemtoScience, Korea). For enhancing the bonding strength, the assembled device was finally performed post-backing in an oven at 80^oC for 1 h (Fig. 3).

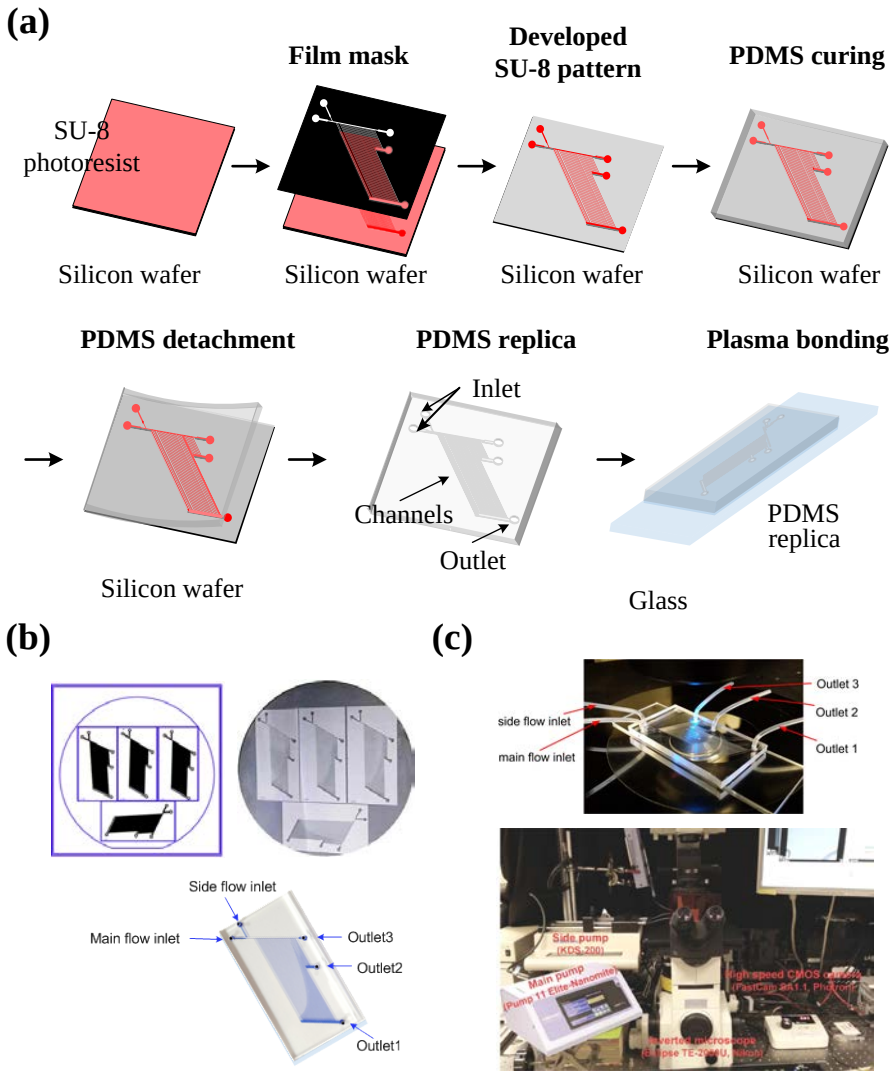

Figure 3. The multibranched chip for sorting of particles and hMSCs. (a) Schematics of the microfluidic chip fabrication procedures and (b) the CAD and master mold of the microfluidic chip used in this study. (c) The completed sorting experiment setting with the microfluidic chip connected pumps via tubing under the microscope.

2. Sorting chip operation

The sample suspension was introduced into the main channel through the main inlet using a syringe pump (Pump 11 Elite-Nanomite, Harvard Apparatus, MA), and the medium fluid was injected into the inlet 2 by another pump (KDS-200, KD Scientific, MA) (Fig. 3). The microfluidic chip was positioned under an inverted microscope (Eclipse Ti-E and Eclipse TE2000, NiKon, Japan) with a 10 x objective lens to allow monitoring and imaging. Most images were taken by a digital 5M pixel sCMOS camera (Zyla, ANDOR, UK) and particle streak images were captured at exposure time of 150 ms with NIS-Elements software. The cell deformation was observed by an ultra high-speed CMOS camera (FastCam SA1.1, Photron, Japan) with 10,000 frames/sec and a $15{,}000^{-1}$/sec exposure time. All sorting data were obtained from at least 3 times and were analyzed by the ImageJ (NIH, MD).

3. Sample preparations for side flow performance and particle sorting

Prior to all of the experiments, all solutions should be are filtered through 0.2 μm syringe filters (Sartorius, Japan) for preventing the clogging in the channel. For flow distribution experiment, the main fluid, only distilled water, was introduced through the main inlet and trypan blue (0.4%) solution (Gibco, CA) was injected from side inlet through Teflon tubing consisted with 1.5 mm (OD) and 0.8 mm (ID). We examined the changes of flow distribution and stream lines based on

various flow rate (Q_t) and the ratio of side flow rate (Q_s) to main flow rate (Q_m) (Table 2).

To examine the fabricated micro devices work, the fluorescent polystyrene latex particles (Thermo Fisher Scientific Inc. MA) with diameter 15 and 39 μm were added into pre-filtered 0.2% triton-X 100 solutions (300 ppm) and gently mixed using a stirrer for 30 min. Simultaneously, prior to experiment, the microfluidic chips were washed for 30 min with dust free 0.2% (w/v) Triton X-100 and filed the solutions to maintain hydrophilic status. The particle mixture was sonicated for 30 sec and then confirmed that the particles did not aggregate in the suspension under the microscope.

The prepared particle solutions was continuously injected into the microchannel using the main syringe pump, while the solution without particles, as a sheath flow, were introduced from the inlet by side syringe pump. Total flow rate (Q_t) was constant for all experiments at 30 μL/min and the ratio of side flow rate (Q_s) to main flow rate (Q_m) was fixed at 6. After separation experiments, collected particles in each outlet were taken images under the microscopy and the efficiency of separation was analyzed by the image J (NIH, MD).

4. hMSCs culture and preparations for cell sorting

hMSCs were purchased from Cambrex (Walkersville, MD) and were culture in low glucose dulbecco's modified eagle's medium (DMEM, Welgene, Korea) supplemented with 10% fetal bovine serum and 1% penicillin/streptomycin (Gibco, CA) at 37^{o}C with 5% CO_2 . Cells were plated at a density of 4 x 10^4 cells /100 mm dishes (BD Bioscience, CA) and were cultured for 48 h. In order to

Table 2. The changes of virtual *W*c based on total flow and the flow rate ratio.

Q_t	Q_m	Q_s	Q_m:Q_s	W_c (μm)	Velocity (cm/sec)	Re	Wall shear rate	ΔP
0.3	0.04	0.17		39.33	0.085	0.06	0.817×10^2	0.0004
0.5	0.06	0.44		39.33	0.142	0.11	0.136×10^3	0.0007
1	0.14	0.86		16.85	0.285	0.22	0.272×10^3	0.0014
3	0.43	2.57		14.98	0.855	0.65	0.817×10^3	0.004
5	0.71	4.29	1:6	13.11	1.42	1.08	0.136×10^4	0.007
30	4.29	25.71		9.72	8.55	6.45	0.817×10^4	0.043
50	7.14	42.86		9.26	14.2	10.8	0.136×10^5	0.072
100	14.3	85.71		8.70	28.5	21.5	0.272×10^5	0.144
200	28.6	171.4		3.75	57.0	43.0	0.545×10^5	0.289
	10	20	1:2	29.62				
	7.5	22.5	1:3	24.41				
30	4.29	25.71	1:6	9.72	8.55	6.45	0.817×10^4	0.043
	2.73	27.27	1:10	9.36				
	1.43	28.57	1:20	8.59				

* flow rate (μL/min); wall shear rate (1/sec); ⊿P (bar/cm)

confirm size-distribution of heterogeneous hMSCs, we captured both images of the cells at cultured and suspended states and analyzed the area and length of cells by the ImageJ (NIH, MD). It is reasonably assumed that the cell diameter can be calculated by a 2-dimesional ellipsoidal particle with major axis L_l (the longest length) and minor axis L_s (the shortest length).

For sorting experiments, the hMSCs were suspended at a concentration of 1.0×10^5 cells/100 μL in DMEM media. Briefly, hMSCs were added to the main inlet at 4.3 μL/min and the media were introduced into side inlet at 25.7 μL/min, respectively. The hMSCs populations were collected from each outlet, and their sizes in taken pictures were measured and analyzed by the software ImageJ (NIH, MD). The values are represented as the mean ± SEM of three independent experiments and the efficiency of separation was represented as the recovery and purity ratio, as previously mentioned.

5. Viability and growth of hMSCs subpopulations

To confirm the cell viability and cell growth, sorting populations from each outlet were assessed via the trypan blue exclusion staining. Cell viability is calculated as the number of viable cells divided by the total number of cells in the grids on the hemocytometer. To investigate the differences of growth rate between sorting populations, 150 cells per each population were seed on the 96 wells and cultured for 7 days. On the everyday, the cell numbers were counted with trypan blue solutions.

6. The surface marker expressions of hMSCs subpopulations-immunocytochemistry

After sorting of hMSCs based on the size, we analyzed the surface marker expressions of each subpopulation using immunocytochemistry as previously described (Haasters et al., 2009). The hMSCs collected from each outlet were seeded at a density of 1.0 x 10^4 cells and were cultured for 48 h. Then, cells were fixed with 4% paraformaldehyde (PFA), permeabilized in 0.2% Triton X-100 and blocked with 5% normal goat serum (NGS) in phosphate-buffered saline (PBS) for 1 h. Each sorting populations were incubated overnight at 4^{o}C with the following primary antibodies: mouse monoclonal anti-CD73, 1:500 (Invitrogen, CA) and rabbit polyclonal anti-CD90, 1:500 (Abcam, Cambridge, UK) or rabbit polyclonal anti-CD105, 1:250 (Abcam, Cambridge, UK). After washing with PBS, cells were incubated with the following secondary antibodies: Alexa Fluor 546 anti-mouse IgG (Invitrogen, Paisley, UK) and Alexa Fluor 488 anti-rabbit IgG (Invitrogen, Paisley, UK). Cells were counterstained with 4,6-diamidino-2-phenylindole (DAPI; Santa Cruz Biotechnology, CA) for nuclear staining. The z-stack images of immunopositive cells were captured using a laser scanning confocal microscope (LSM700, Carl Zeiss, Germany).

7. Adipogenic, osteogenic, and Schwann cell differentiation from sorted hMCSs

First, each size-sorted subpopulation and unsorted hMSCs were seeded at a density of 4,500 cells/well in 96-well plates and were cultured for 48 h. For

adipogenic induction, the confluent cells were incubated in DMEM with 10% FBS, 0.1 μM dexamethasone, 10 μg/mL insulin, 0.5 mM 3-methyl-1-isobutylxanthine, and 50 μg/mL indomethacin for 7 days (Lee et al., 2014a). For osteogenic induction, the cells were cultured in medium containing 0.2 μM dexamethasone, 10 mM glycerophosphate, and 50 μg/mL ascorbic acid for 7 days (Byun et al., 2012). All experiments were processed with the unsorted group under differentiation conditions and the unsorted groups under non-differentiation conditions simultaneously as the control s. The differentiation media were replaced every 2 days, and all reagents for cell differentiation were obtained from Sigma-Aldrich Corp. (Sigma-Aldrich, CA). Schwann cell (SC) differentiation of hMSCs was induced as reported previously (Park et al., 2012). First, the sorted subpopulations and the control cell groups were plated at a density of 3×10^4 cells/well in 24-well plates, and cultured with growth media containing 1 mM β-mercaptoethanol for 24 hr. Next, the cells were cultured in differentiation medium including 0.28 μg/mL all-trans-retinoic acid for 3 days. Then, the cells were incubated with medium containing 10 μM forskolin, 10 ng/mL recombinant human basic fibroblast growth factor (bFGF), 5 ng/mL recombinant human platelet-derived growth factor-AA (PDGF-AA), and 200 ng/mL human heregulin-β1 (HRG- β1) for 8 days (Dezawa et al., 2001; Park et al., 2012). The differentiation media were replaced every 2-3 days, and all reagents for cell differentiation were purchased from Sigma-Aldrich.

8. Oil-Red O and alkaline phosphate staining

The differentiated cells were fixed with 4% paraformaldehyde (PFA) for

10 min at room temperature and then incubated with the appropriated staining solutions. Adipogenic differentiated groups were reactive with 0.3% Oil Red O for 30 min in dark (Lee et al., 2014a). Lipid droplets can be visualized with Oil Red O, a lysochrome diazo dye that stains neutral triglycerides, lipids, and lipoproteins. After removing the staining solution, the cells were washed 3 times with H_2O followed by observation. For alkaline phosphatase staining, the osteogenic induction cells were stained with 0.1 mg/ml naphthol AS-MX phosphate, 0.5% N,N-dimethylformamide, 2 mM $MgCl_2$, 0.6 mg/ml fast blue BB salt, and 0.1 M Tris-HCl (pH 8.5) for 30 min at room temperature (Byun et al., 2012). Alkaline phosphatase (ALP) is a membrane-bound glycoproteins and is bound to the membrane of osteoblast and functions to enhance osteogenesis by degrading pyrophosphate. In ALP staining, formazan dye with a bluish-purple color is generated in the presence of alkaline phosphatase through a reaction mediated by components in the substrate solution (Zhu et al., 2010). After staining, the staining solution was removed, and the cells were washed three times with H_2O. The stained cell images were taken by CCD camera (AxioCam-HRC, Carl Zeiss, Germany) under inverted microscopes (Eclipse Ti, Nikon, Japan). All reagents for cell differentiation and staining were obtained from Sigma-Aldrich.

9. Reverse transcription-polymerase chain reaction

For reverse transcription-polymerase chain reaction (RT-PCR), total RNA was extracted from differentiated cell populations using Trizol® reagent (Life technologies, Carlsbad, CA). cDNA was synthesized from 1 μg/mL of total RNA using M-MLV reverse transcriptase (Invitrogen, CA) and semi-quantitative RT-

PCR was performed using i-StarTaqTM DNA polymerase (Intron Biotechnology, Seongnam, Korea). Table 3 displays the primer pairs for differentiation markers and PCR reaction conditions (Yang et al., 2011; Kim et al., 2012; Park et al., 2012). The amplified PCR products were electrophoresed on 2% agarose gels containing ethidium bromide (Et-Br) and analyzed using ImageJ software.

10. Image analysis and statistics

As previously mentioned, all data are expressed as the mean ± SEM of at least three independent experiments. Statistical comparisons of the experimental results were determined by analysis of variance (ANOVA) followed by Tukey's post-hoc honestly significant difference (HSD) test.

Table 3. PCR primer sequence and experiment conditions

Gene	Primer sequence	Product size (bp)	Annealing tem. (℃)	Cycle No.	Accession No.
Adipogenic differentiation markers					
PPARγ2	5′-tgtctcataatgccatcaggtttg-3′ 5′-gataacgaatggtgatttgtctgtt-3′	250	58	33	NM_015869
LPL	5′-gagatttctctgtatggcacc-3′ 5′-ctgcaaatgagacactttctc-3′	276	58	33	NM_000237.2
aP2	5′-accaggaaagtggctggcat-3′ 5′-caggtcaacgtcccttggct-3′	331	59	31	NM_001442
Adiponectin	5′-agcctccttctcctgggtcc-3′ 5′-gttgcctctagcctggtggg-3′	295	59.5	35	NM_001177800
Osteogenic differentiation markers					
OCN	5′-atgagagccctcacactcct-3′ 5′-gccgtagaagcgccgatagg-3′	197	59	35	NM_199173.4
MSX2	5′-gccaagacatatgagccctaccacct-3′ 5′-ggacaggtggtacatgccatatccca-3′	400	59	35	NM_002449.4
RUNX2	5′-tatgaaaaaccaagtagcaaggttc-3′ 5′-gtaatctgactctgtccttgtggat-3′	336	59	33	NM_001278478
OPN	5′-agccccacagacccttccaa-3′ 5′-caatggagtcctggctgtcca-3′	104	59	35	NM_001040060

Table 3. PCR primer sequence and experiment conditions

Gene	Primer sequence	Product size (bp)	Annealing tem. (℃)	Cycle No.	Accession No.
Schwann cell differentiation markers					
GFAP	5′-gtaccaggacctgctcaatg-3′	293	60	30	NM_002055
	5′-tgtgctcctgcttggactcctt-3′				
P0	5′-cccaggccatcgtggtttac-3′	338	59.5	35	NM_000530
	5′-ggtcttgcccactatgtctgg-3′				
S100	5′-ggtcttgcccactatgtctgg-3′	158	59	32	NM_006272
	5′-cagtgtttccatgactttgtcca-3′				
HGF	5′-atgctcatggaccctggt-3′	423	59	32	M73239
	5′-gcctggcaagcttcatta-3′				
VEGF	5′-gccttgctgctctacctcca-3′	401	59	32	X62568
	5′-caaggcccacagggatttt-3′				
GAPDH	5′-accacagtccatgccatcac-3′	452	58	24	NM_002046
	5′-tccaccaccctgttgctgta-3′				

IV. Results

1. hMSCs size distribution

As above mentioned, hMSCs are known as composed of heterogeneous populations with variable sizes. First of all, to verify this characterization of hMSCs, we investigated size distributions of hMSCs to confirm the size barriers and determined the number divided cell scale ratio in our study. From the cell images in cultured states, the longest length (L_l), the shortest length (L_s) and the area were analyzed using Image J and these parameter were compared to the literature data (Haasters et al., 2009) (Fig. 4a). Note that the size distribution at suspended state is meaningful information for the microfluidic chip filtration. As Fig. 4b, the equivalent diameter d ($=\sqrt{L_l L_s}$) of our hMSCs is ranging from 16 to 62 μm (ave. 26.1 ± 2.1 μm) in suspended status. We determined their sizes into three groups: small (< 25 μm), medium (25-40 μm), and large (> 40 μm) one. The corresponding cumulative populations are estimated as 42, 47, and 11%. Therefore, we determined Wc for 12.5 μm (a half of small cell average diameter) and 20 μm (a half of medium average diameter) for outlet 1 and outlet 2, respectively in this chip.

2. Side flow effects on focusing and flow fractionation

Prior to all experiments, we performed like this are being calculated (theoretical value), the flow velocity of the fluid in the chip ensure that each outlet was designed by fractionation. In this experiment, Q_t and running times were out coming flow volume in each outlet were measured and compared the ratios of fractionation, respectively.

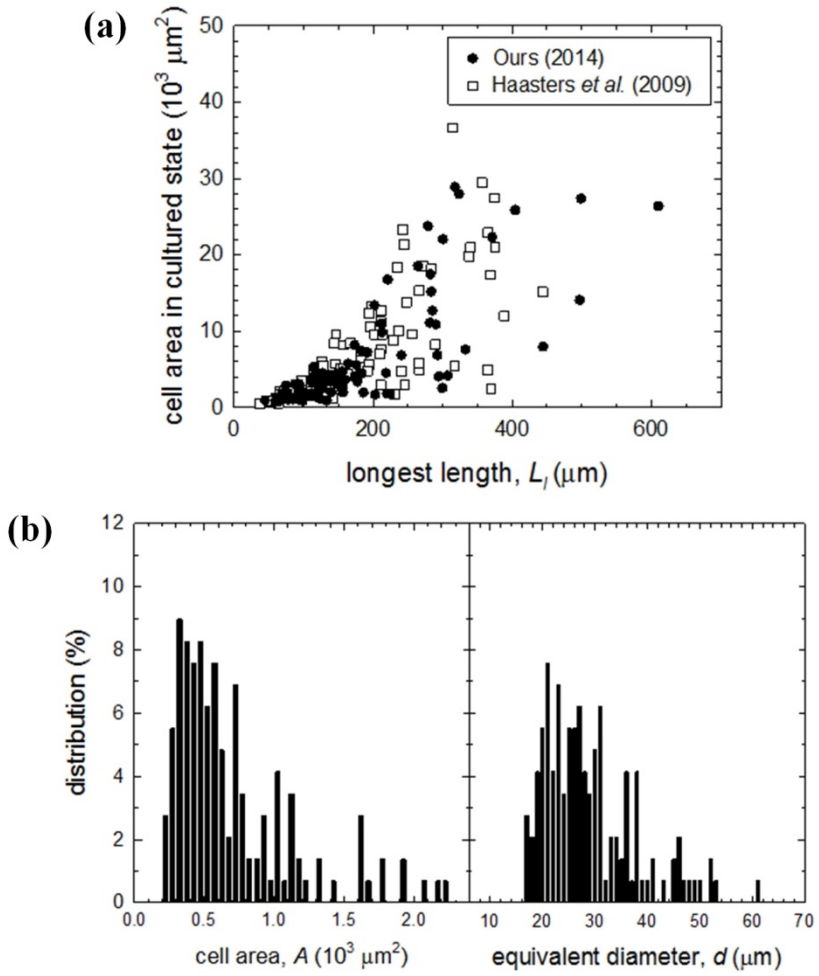

Figure 4. The hMSCs size distribution. (a) Relationship between major axis and 2-dimensional area of hMSCs in cultured state compared with previously published data, and (b) distribution of suspended hMSCs based on 2-dimensional area and its equivalent diameter.

Considering the design, we predicted the theoretical flow distribution values and the output flow rate values demonstrated 92.49 % at outlet 1, 4.59 % and 2.92% at outlet 2 and outlet 3.

We performed the flow fractionation of this microchip at variable Q_t = 5, 30, and 100 μL but flow ratio was fixed at 6 (Q_s:Q_m). From the experiments (5 μL/min) we have got the flow fractionation ratio, 69.29 ± 1.1% at outlet 1, 16.75 ± 1.0% and 13.95 ± 1.2% at outlet 2 and outlet 3. At Q_t = 30 μL/min, the flow fractionation ratio were 87.14 ± 1.6% at outlet 1, 6.84 ± 0.6% and 4.96 ± 2.59% at outlet 2 and outlet 3. In addition, At Q_t = 100 μL/min, the flow fractionation ratio were 86.85 ± 1.44% at outlet 1, 7.37 ± 0.19% and 5.76 ± 1.26% at outlet 2 and outlet 3.

At the microchannel design stage it was assumed that the flow rate distribution in the horizontal (width) direction is parabolic as shown in Fig. 1 while the flow rate distribution in the vertical (depth) direction was neglected. Theoretically, it was estimated that percentages of the volumetric flow rate passing through each branch point will be split into a side channel, when the ratio of the flow rates from inlets 1, 2, and 3 is 1:1:0.2.

The range of total flow rate (Q_t) was conducted from 0.3 to 200 μL/min and that of ratio was conducted from 3 to 20, respectively (Fig. 5). Due to the flow rates of the two inlet and the flow ratio of the main and the side fluid (Q_s/ Q_m) were various fluids and dimensions of the inlet channels, when the two fluids “met” at the entrance of the main channel, the main fluid was pushed further towards the side walls, decreasing the width of the main fluid. At the entrance region, the main and the sheath fluid “met” and fully-developed at 2,000 μm downstream of the

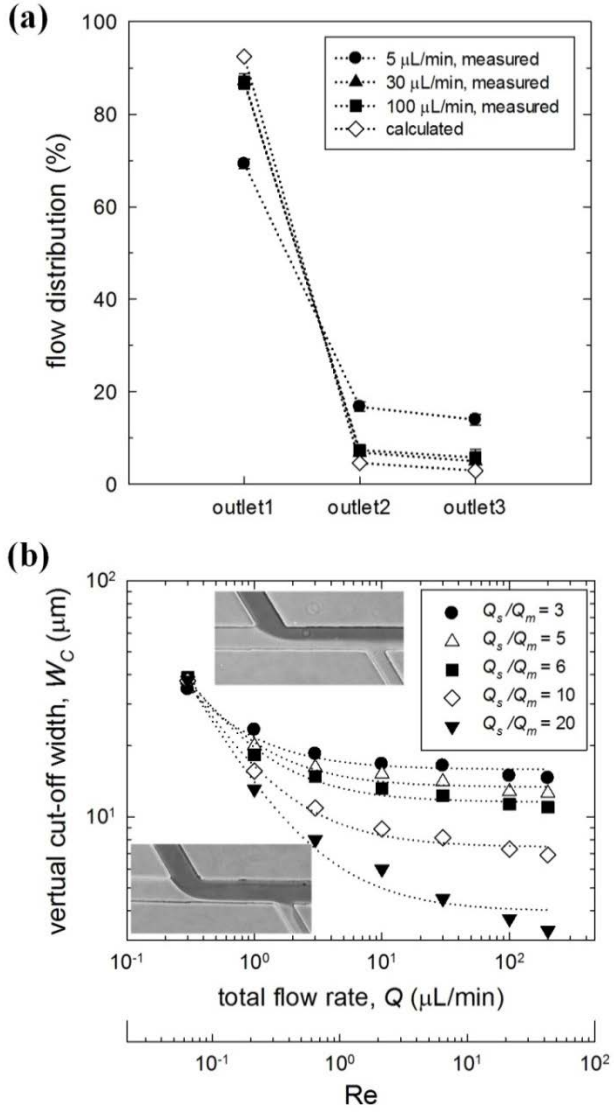

Figure 5. Flow distribution in the multibranched sorting chip. (a) Comparisons of calculated flow fractionation and experimental flow fractionations in various flow ratios. (b) Virtual cut-off widths with variations of Q_t and Q_s/Q_m, which are determined from the fully-developed region between main and side channel node and first branch point. Microscope images show flow fractions by weak focusing

for Q_s/Q_m = 6 and Q_t = 0.3 μL/min (upper) and strong focusing for Q_s/Q_m = 20 and Q_t = 100 μL/min (lower).

entrance length, which is called width of *W*c. The depth of *W*c were observed by the inverted epi-microscope and the images were captured using sCMOS camera. The all image data was analyzed by the ImageJ (NIH, MD).

3. Sorting of bidisperse spherical particles

Before the cell size dependent separation, we first examined whether spherical rigid model particles behaviors would move toward one sidewall by flow splitting and diverts into the outlets relative to their size. Fig. 6a shows the streak imaging of particle behavior at the confluent points of the main channel and branch channels. Small particles with 15 μm diameter might go to the branch channel, whereas 39 μm particles, which are larger size, are passed along the main channel. It was therefore demonstrated that the particles with diameter larger than 39 μm moved toward one sidewall in the main channel after the split flows were recombined in the main channel. In fact, the theoretical value of *W*c was 12.5 μm and the virtual values of *W*c was 9.72 μm for the first 48 branches. It was suggested that particles with radius larger than *W*c never go through the side channels. It was expected that spherical solid particles/cell with diameter larger than 2 × *W*c would flow through the main channel but would not flow into the side channels.

The images of sorted particles in each outlet are shown in Fig. 6b. As shown in the data, the small particles with 15 μm were mainly collected at outlet 1 and larger ones with the 39 μm were found at outlet 2 and outlet 3 after separation. To evaluate the separation efficiency, particles collected from each outlet were analyzed using ImageJ, which were presented graphs of the purity and recovery rate in Fig. 6c. The recovery rate is defined as the ratio of the number of target particles

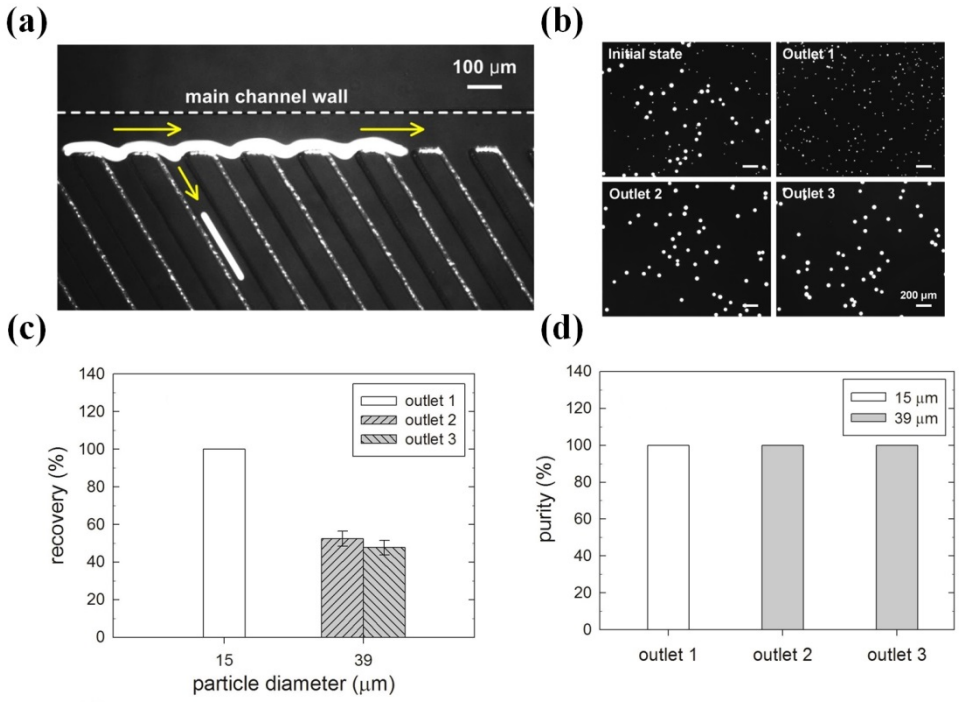

Figure 6. Sorting results of the model particles using multibranched chip. (a) Streak images of large particle (39 μm) flowing in main channel and small one (15 μm) flowing in branch channel, where images were taken at the region between 4th and 12th branch points, (b) The images of particles before sorting and particles from collected each outlets after sorting, and (c-d) the sorting efficiency represented recovery and purity ratio.

collected through a particular outlet to the total number of target particles during sorting. The purity ratio is represented as the ratio of the number of target particles to total number of particles in a particular outlet (Jung et al., 2015). As shown in Fig. 6c, 15 μm particles were found in outlet 1 only, represented recovery rate of 100%. While, 39 μm particles were collected through outlet 2 and outlet 3 at a recovery rate of 55% and 45%, respectively. Considering of purity ratio, 100% of the 15 μm particles went through the outlet 1, and 100% of the 39 μm went through outlet 2 and outlet 3.

4. Sorting of hMSCs subpopulation

Regarding the movement of particles, Fig. 7a shows streak images of green fluorescent protein-labeled hMSCs along the branch channel during separation. Fig. 7b shows the distribution of hMSCs collected in each outlet. The average sizes of the cells were 17.2 ± 5.3 μm in outlet 1 and 28.8 ± 5.4 μm in outlet 2. Also, cells 52 ± 13 μm or over 55 μm, which seemed to be aggregated, were observed in outlet 3. In this study, the aggregated cells were regarded as a single large cell and exited via Outlet 3. As predicted, small (< 25 μm), medium (25-40 μm), and large (> 40 μm) cells were main founded in outlets 1, 2, and 3, respectively. The purity obtained using label-free microfluidic techniques ranges from about 60-99%. Our results show that sorting populations of small and large cells from hMSCs concentrates the population of hMSCs with high multipotency. We emphasized that our hMSC sorting data represents improved cell-sorting efficiency.

In outlet 1, the smaller cells were recovered at a rate of 93.9%, and the

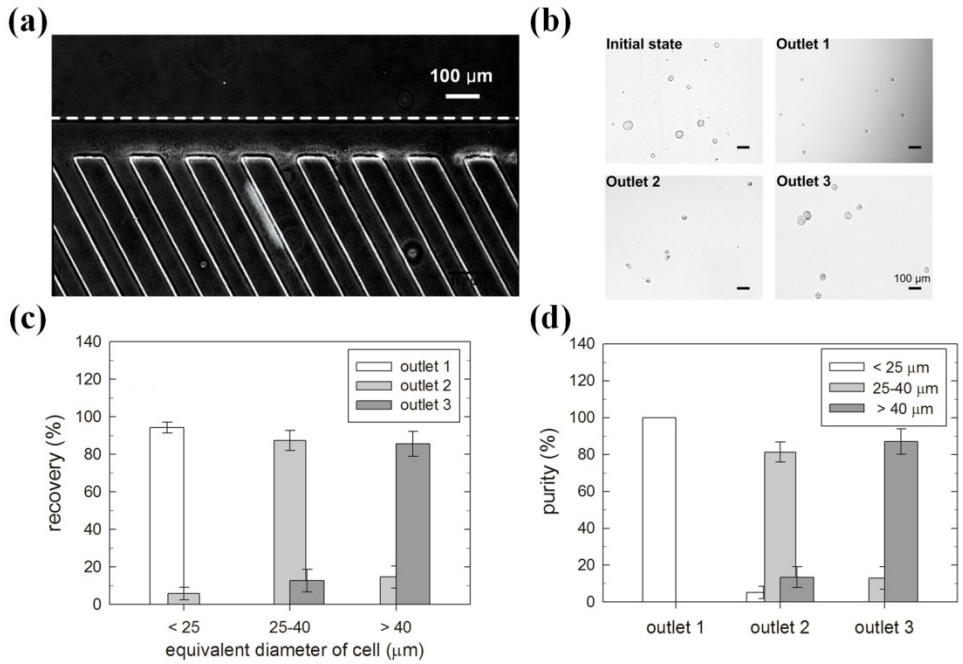

Figure 7. Sorting results of hMSCs using multibranched chip. (a) Sorting performance of a large cell flowing in main channel and small one flowing in branch channel. (b) The images of hMSCs before sorting and subpopulations from collected each outlet after sorting, and (c-d) the sorting efficiency with recovery and purity ratio.

cells ranging between 25 and 40 μm in size were recovered at a rate of 4.92%. However, few cells (> 40 μm in diameter) were found there. In addition, the purity of the cells collected at outlet 1 was 100%, which is one of the highest purities obtained from current label-free microfluidic sorting techniques (85% and 95%). In outlet 2, the medium cells were recovered at a rate of 80.4% and the smaller cells were recovered at a rate of 15%. In addition, the purity of the cells at outlet 2 was over 98.7%. The larger cells were not observed here. In contrast, large cells (> 40 μm in diameter) were recovered at a rate of 85% in outlet 3. Moreover, the purity of the cells in outlet 3 was 84%. Interestingly, the purity and recovery of cells was slightly lower than that for particles. This may be due to the effects of cellular shape and deformability. Although the cell deformation is so weak in our HDF chip (Fig. 8), the effect still could change their original shape and interfere with cell movements, which decrease the sorting efficiency. First, we considered ratio of the maximum to minimum diameters of hMSCs to predict cell shape (Fig. 9). In any rotated cells, it is possible to measure both L_l and L_s by applying the reasonable assumption of a 2D ellipsoid for the dimensions of the deformed cell.

As shown Fig. 9a, the dotted lines (blue color) represent the compact equivalent sphere. A ratio closer to 1 equated to a sphere shape, whereas a ratio far from 1 indicated an ellipse shape. As Fig. 9b shows, the population of cells mainly factors such as cellular shape and deformability when sorting for a particular size. Recent studies on inertial separation focusing on non-spherical particles reported that the rotational diameter of particles, regardless of their cross-sectional shape, determines the final focused position, except in the case of asymmetric disks. Also, deformable cells were found to migrate more rapidly toward the center than

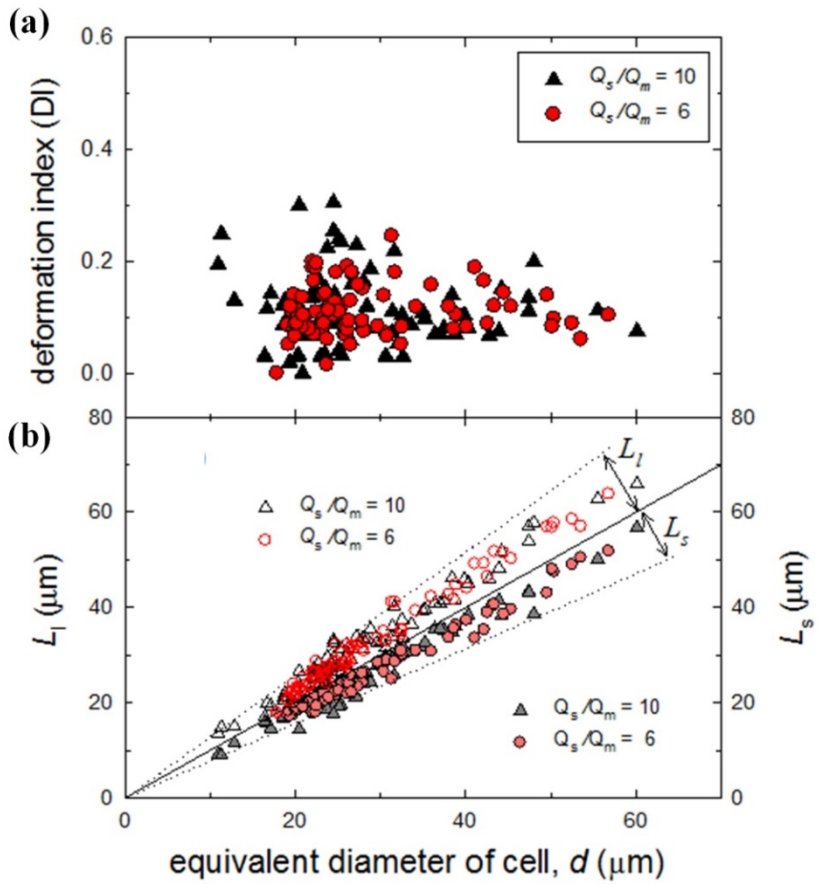

Figure 8. Deformability of hMSCs in the multibranched channel with different flow ratio. (a) Deformation index (DI) represented the change of cell shapes to different flow ratio (Q_s:Q_m = 10 and 6). (b) The relationship between change of hMSCs's L_l and L_s and cell diameter in different flow ratio conditions.

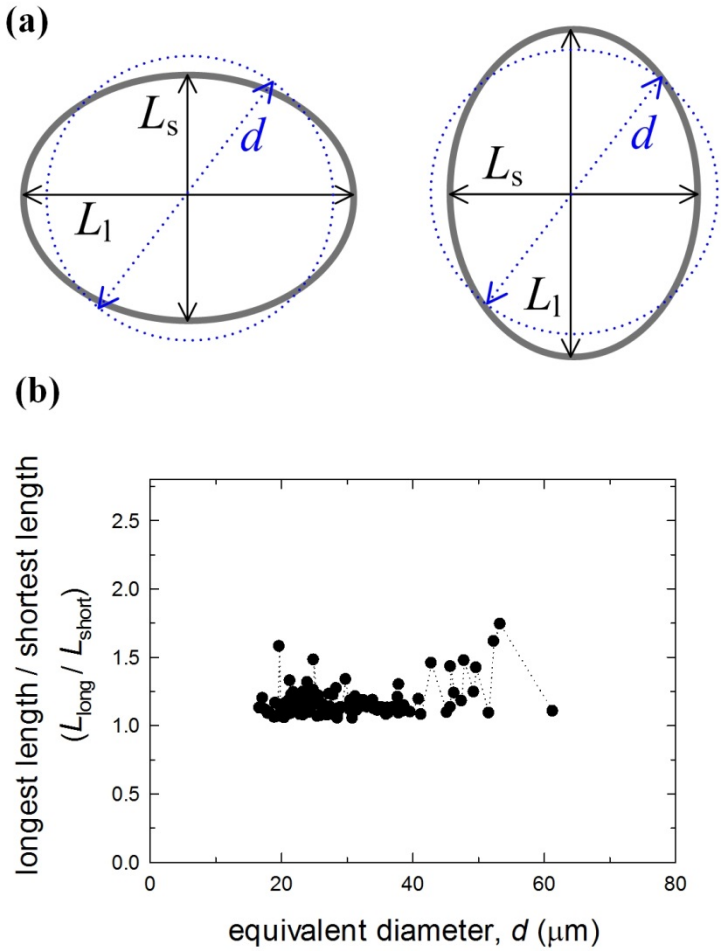

Figure 9. Biophysical makers of hMSCs in suspended state. (a) Cell diameter assumed major axis (L_l) and minor axis (L_s) with rolling behavior. (b) The circularity of hMSCs calculated from L_l and L_s in suspended status.

hardened cells.

These studies displayed good agreement with our results that FL cells, which are more deformable than smaller cells, underwent fast lateral migration toward the center. These favorable results may not always occur when FLs (relatively large and hardened cells) are separated from small, RS and SS cells (relatively small but deformable cells). However, these issues must be studied in future works.

5. Cell viability and growth of hMSCs subpopulation

In this study, we proposed channel sorting via a sorting chip and HDF using only fluid and no chemical modification to achieve cell separation with minimal physical damage. Optical micrographs and viability results for the sorted hMSCs obtained from the outlets are shown in Fig. 10. Following separation, cell viability was assessed using trypan blue dye exclusion and was expressed as the percentage of viable cells (cells that excluded the dye) among the total cells collected from each outlet. As illustrated in Fig. 10a, the viabilities of the sorted subpopulations were 97%, 92%, and 90% from Outlets 1, 2, and 3 at 30 μL/min, respectively. These percentages are similar to the initial viability of hMSC cells and comparable to results previously reported (Yamada et al., 2007; Lee et al., 2011; Warkiani et al., 2014). The levels decreased slightly at 50 μL/min (95%, 91%, and 87% from Outlets 1, 2, and 3, respectively), but the sorting process did not cause critical damage. Indeed, the large cells exhibited lower viability than the small and medium cells. This suggests that the effect of flow conditions on viability is dependent on cell characteristics such as size.

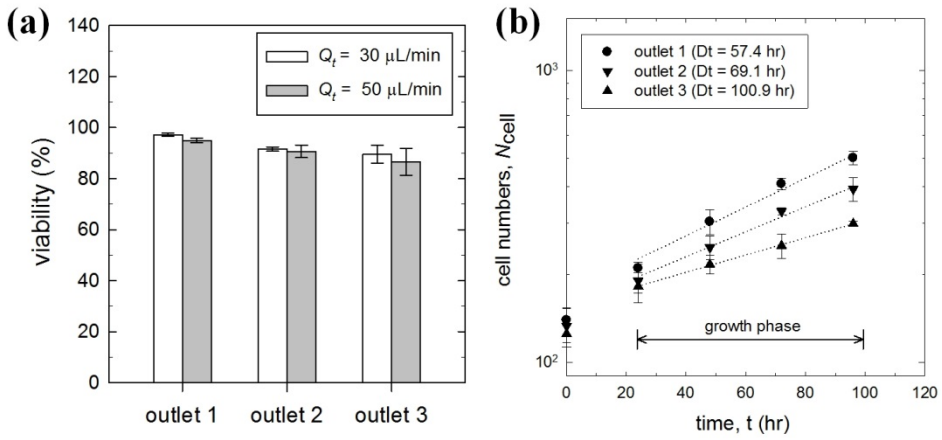

Figure 10. Viability of cells before separation and after sorting process. (a) Viability of sorted cells from each outlet after sorting for different total flow rates and (b) comparison of growth rate between unsorted (initial) cells and accumulative sorted cells from all outlets after sorting.

Next, we compared the cell growth rate between the sorted subpopulations to determine the population with the highest rate of self-renewal. The same number of sorted cells from each outlet were seeded, and then the total number of cells were counted at the indicated times. On the basis of doubling time (tD), we found that small cells collected from Outlet 1 grew faster than the others (cf., 57.4, 69.1, and 100.9 hr for each cell), as presented in Fig. 10b. The tD was calculated as follows:

$$tD = t[\ln 2/\ln (Nf/Nb)], \quad (16)$$

where Nb was the cell number at the beginning of the incubation time, and Nf was the cell number at the end of the incubation time.

6. Expression of surface markers in the sorted subpopulations

Generally, hMSCs would be defined by the specific surface marker expressions as one of the minimal criteria (Dominici et al., 2006). In previous study, among the hMSCs populations, the small and rapid self-renewing cells expressed CD73, CD90, and CD105 simultaneously, while large flattened cells showed a loss of one or more hMSC surface markers, mainly lack of CD73 expression (Hassters et al., 2009). Thus, we would determine whether our sorting populations could be represented to them in previous reports.

According to Fig. 11a, the small rounded cells collected from outlet 1 expressed CD73 and CD90 together, representing that they were RS-like cells. The medium-sized outlet 2 cells with spindle-shaped also showed both CD73 and CD90 expressions, indicating they were SS-like cells. On the other hand, the large cells from outlet 3 have only CD90 without CD73, suggesting that the cells were FL-like

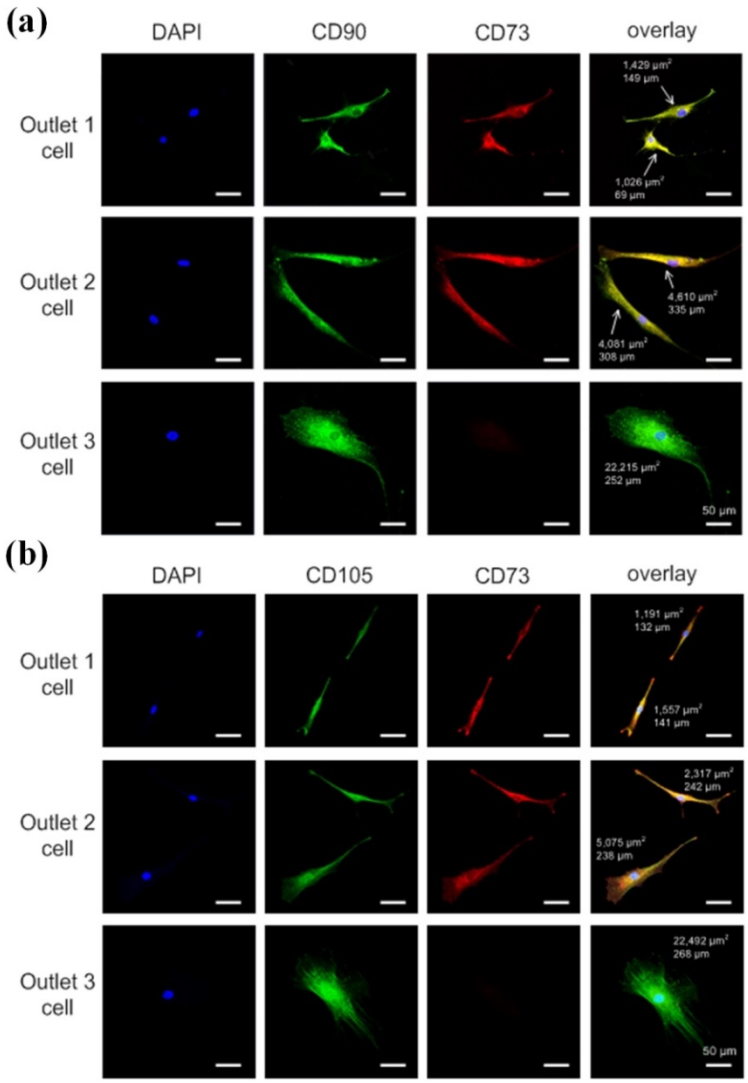

Figure 11. Morphological and immunochemical characterizations of hMSC subpopulations. The images show the maximum diameter and area with the expressions of (a) CD73 and CD90; (b) CD73 and CD105 in each collected cell.

cells. Additionally, in Fig. 11b, the cells from outlet 1 show high level of CD73 and CD105 together, but the cells from outlet 3 did not find CD73 expression. We analyzed and summarized the expression levels of each population in Table 4. In Table 4, all the cells from outlet 1 were double expressions for CD73/CD90, whereas most cells from outlet 3 (84.4%) show CD 90 expressions without CD 73.

Likewise, similar results were obtained with double immunocytochemistry of CD73/CD105. All the cells from outlet 1 were double positive, whereas most cells from outlet 3 (91.7%) were single positive for CD105. We also measured the maximum diameter and the area of cells from each outlet and compared with the previous data. Our results are consistent with the previous report that the maximum diameter of RS cells is less than 157 μm and the area is smaller than 6617 μm^2, while FL cells have a larger maximum diameter (> 157 μm) and a larger area (> 6617 μm^2). The previous report presented the correlation between the morphological characteristic of each subpopulation of hMSCs and the expression patterns of surface markers.

These data demonstrated that sorting hMSCs using microfluidic chip filtration can successfully fractionate into the three subpopulations RS, SS, and FL cells, respectively.

7. Differentiation of hMSCs subpopulations

Several studies have shown that the cell cycle of hMSCs is correlated with a small and highly proliferative subpopulation of hMSCs; smaller hMSCs exhibit enhanced differentiation potential into typical mesenchymal tissue cell

Table 4. Immunocytochemical analysis of hMSC subpopulations.

Surface marker	Total No. of cells	No. of cells (%)		
		Outlet 1	Outlet 2	Outlet 3
CD73(+)	134	0 (0)	3 (6.4)	0 (0)
CD90(+)		0 (0)	3 (6.4)	27 (84.4)
CD73(+)/CD90(+)		55 (100)	41 (87.2)	0 (0)
CD73(–)/CD90(–)		0 (0)	0 (0)	5 (15.6)
CD73(+)	183	0 (0)	3 (4.4)	0 (0)
CD105(+)		0 (0)	3 (4.4)	44 (91.7)
CD73(+)/CD105(+)		67 (100)	62 (91.2)	0 (0)
CD73(–)/CD105(–)		0 (0)	0 (0)	4 (8.3)

lineages via chemical induction relative to larger hMSCs (Colter et al., 2001; Lee et al., 2011). To verify the relationship between cell size and multipotency. we investigated the adipogenic, osteogenic, and Schwann cell (SC) differentiation potentials of the sorted populations, and compared the morphologic changes among subpopulations during differentiation. Thus, following size-based sorting, the subpopulations were subjected to the induction procedures, and compared with the unsorted and non-induction groups as the controls.

After adipogenic differentiation, no morphological differences were observed among the sorted populations under a bright-field microscope for the first 2 days. On the third day, lipid droplets (black spots in the figures) were apparent in the RS and SS populations, but not in the FL or the control populations (Fig. 12a). These black spots were confirmed to be lipid droplets at high magnification (data not shown). On the seventh day, the number and size of droplets in both subpopulation groups had increased considerably relative to Day 3. Some lipid droplets were found in unsorted cells, but these were detected less than in RS and SS cells. Lipid-droplet formation in FL cells was comparable to that in the non-induction group.

After osteogenic differentiation, several studies have reported that cells become flat and spread in multiple directions in two dimensions compared with the fibroblast-like spindle shape of the control cells (Matsuoka, 2013). Likewise, in our data, it was difficult to detect morphologic changes in cells during osteogenic differentiation because the cells appeared very thin and flat under the bright-field microscope. Thus, we performed ALP staining of the subpopulations and the control cells to confirm differentiation. For the first 2 days, no significant

morphologic changes were observed. However, from the third day, induction group cells were flat and spread out, whereas the control cells were compact and dense. Moreover, as expected, ALP activity was significantly higher in RS and SS cells than in unsorted and FL cells (Fig. 12b). First, we stained the subpopulations that had undergone adipogenic differentiation with Oil Red O. Induction was apparent by the accumulation of lipid-rich vacuoles within the cells, which continued to develop over time, coalesced, and eventually filled the cells (Pittenger et al., 1999). As shown in Fig. 13a, RS and SS populations had many more lipid droplets with red color along the cell edges than unsorted and the control cells. Moreover, the number of lipid droplets in RS and SS cells was much higher than that in FL and the control cells. Although the observed morphologic differences may be related to differentiation, they are insufficient to quantitatively predict the final cellular state (Matsuoka, 2013). Thus, the adipogenic character of the sorted populations was evaluated by performing functional and genetic assays. In adipogenic differentiation, a complex series of changes involving the expression of specific genes occurs. Stem cell differentiation is characterized by growth arrest, followed by the induction and expression of multiple adipogenic genes and, ultimately, triglyceride accumulation. Peroxisome proliferator-activated receptor gamma 2 (PPARγ2), lipoprotein lipase (LPL), aP2, and adiponectin are key regulators of adipocyte differentiation. PPARγ2 is a transcription factor expressed at high levels by adipocytes during the early stages of adipogenic differentiation (Tontonoz et al., 1994; Cristancho & Lazar, 2011). LPL is an enzyme that the controls lipid accumulation that is induced by insulin and troglitazone during adipogenic differentiation (Bouraoui et al., 2012). aP2, also known as fatty acid binding protein

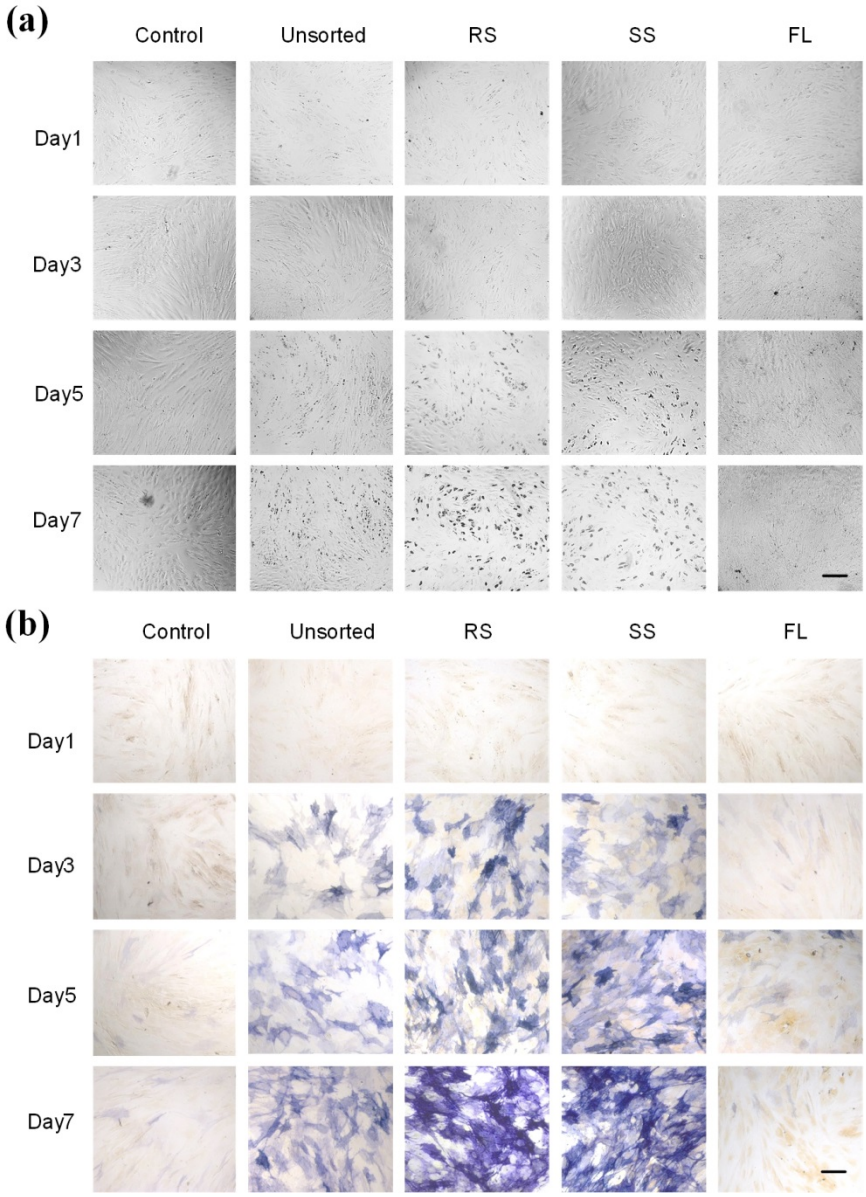

Figure 12. Morphological changes in sorted populations during adipogenic and osteogenic differentiations. The sorted populations were cultured in (a) aidipogenic and (b) osteogenic differentiation media for 7 days and the morphological changes

were observed. The non-differentiation induction populations and unsorted populations were cultured simultaneously as the controls. Scale bars: 200 μm.

binding protein 4 (FABP4), is a carrier protein for fatty acids and has been extensively used as a marker for differentiated adipocytes (Baxa CA et al., 1989). Adiponectin is secreted protein from adipocytes and has a role in modulating glucose regulation and fatty acid oxidation (Yamauchi et al., 2001). We examined the expressions of these adipogenic markers using semi- quantitative RT–PCR analysis. As shown in Fig. 13b, PPARγ2 expression in the RS and SS populations was 3- and 2.5-fold higher than in the unsorted group, respectively, and six- and fivefold higher than in the FL group, respectively. LPL expression in the RS and SS populations was 1.8 and 1.7-fold higher than in the unsorted group, and 7.5 and 7.2 fold higher than in the FL group, respectively. The expression of aP2 in the RS and SS populations was higher than the FL groups (1.3 times) but comparable to the unsorted groups. Additionally, the adiponectin level in RS was higher than in the unsorted group and SS group and significantly higher than in the FL group, respectively. These results indicated that the differentiation potential of RS and SS cells was indistinguishable. These results indicate that RS and SS groups have higher adipogenic differentiation potential than the unsorted population because of the removal of FL cells with lower differentiation potential.

Under osteogenic differentiation conditions, the populations showed remarkably different levels of ALP activity despite no significant morphologic differences, as shown in Fig. 14a. The RS and SS groups exhibited considerably higher ALP activity than unsorted cells or the LF population, but the control group did not exhibit mineralization under basal in-vitro culture conditions. Next, the relative expression levels of osteogenesis-related genes, namely Runt-related transcription factor 2 (RUNX2), osteocalcin (OCN), osteopontin (OPN), and msh

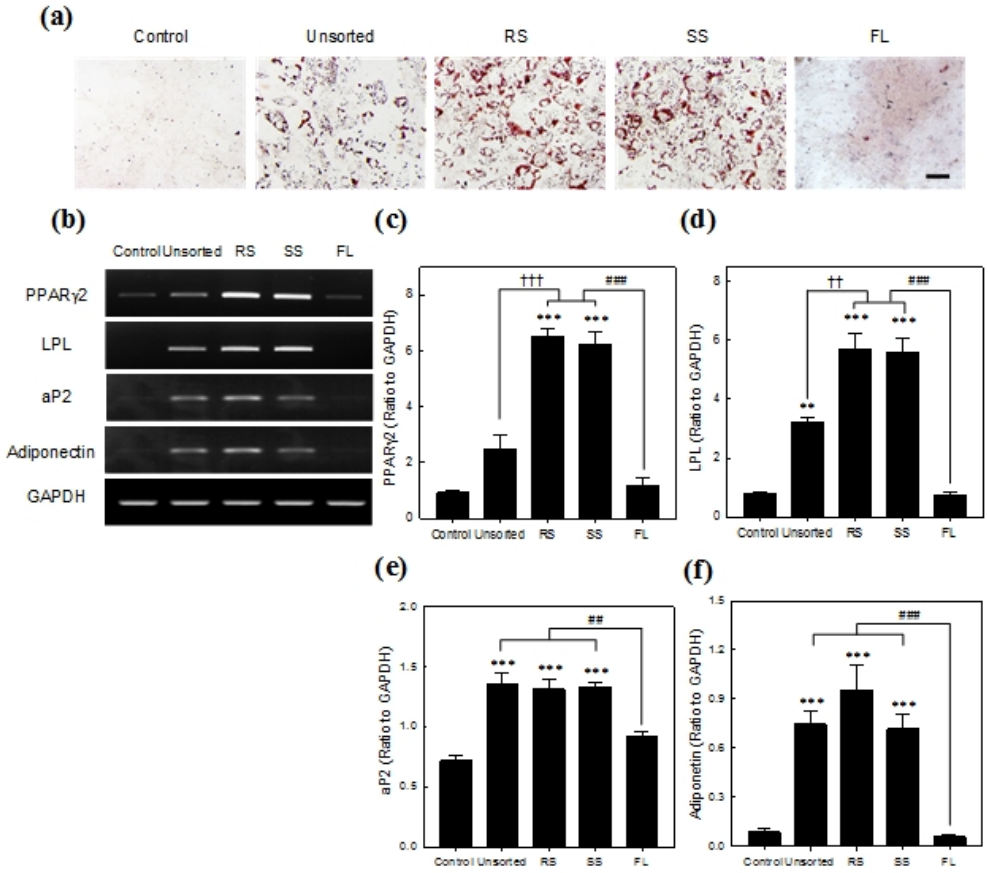

Figure 13. Comparison of adipogenic marker gene expressions in sorted subpopulations. Using the semi-quantities RT-PCR, the expression of markers for adipogenesis (PPARγ2, LPL, aP2, and adiponectin) were analyzed. There data were normalized to glyceraldehyde-3-phosphte dehydrogenase (GAPDH) and their relative expression was calculated. The bars represent mean ± SEM of at least three independent experiments. $^{***}P < 0.001$, $^{**}P < 0.01$, $^{*}P < 0.05$ versus the control hMSCs. $^{\dagger\dagger}P < 0.01$, $^{\dagger}P < 0.05$ versus unsorted hMSC and $^{\#\#\#}P < 0.001$, $^{\#\#}P < 0.01$ versus FL cells. ANOVA followed by post hoc Tukey's HSD test. Scale bars: 100 μm.

homeobox homologue 2 (MSX2), were quantified using semi-quantitative RT–PCR analysis. RUNX2 is a key transcription factor and a central regulator of bone formation, which mediates osteoblast-specific target genes, such as OCN during osteoblast differentiation (Ducy et al., 1997, Byun et al., 2012). OPN is a matricellular protein that predominantly expressed in bone by osteoblast and controlled by transcription factors, such as RUNX2 and osterix (OSX) (Kim et al., 2012). OCN is a bone-specific protein synthesized by osteoblasts and secreted into conditioned media at early stages of osteogenesis (Nakamura et al., 2009). MSX2 is a homeodomain transcription factor that acts upstream of RUNX2, which enhances osteogenesis (Cheng et al., 2003; Kim et al., 2012). Expressions of these genes indicate mineralization, which reflects the osteogenic potential of cells. Fig. 14b shows that OCN expression was 1.5 and 1.4 times higher in RS and SS cells than in the unsorted group, respectively, and four- and fourfold higher in RS and SS cells than in FL cells, respectively. Similarly, MSX2 expression in the RS and SS groups was three- and 2.5-times higher, respectively, than in the unsorted group. Moreover, MSX2 expression in the RS and SS groups was at least six and five times higher, respectively, than in FL cells, similarly to the control groups. However, the differentiation potential was indistinguishable between RS and SS cells.

Together, RS and SS groups consist of the cells with differentiation potential, whereas FL cells exhibit a low differentiation potential similar to that of the control groups. Interestingly, the unsorted group exhibited potential, but this would be lower than that of RS and SS groups because of the presence of FL cells in the unsorted population. Therefore, the sorted subpopulations have different differentiation potentials, and RS and SS cells possess significantly higher

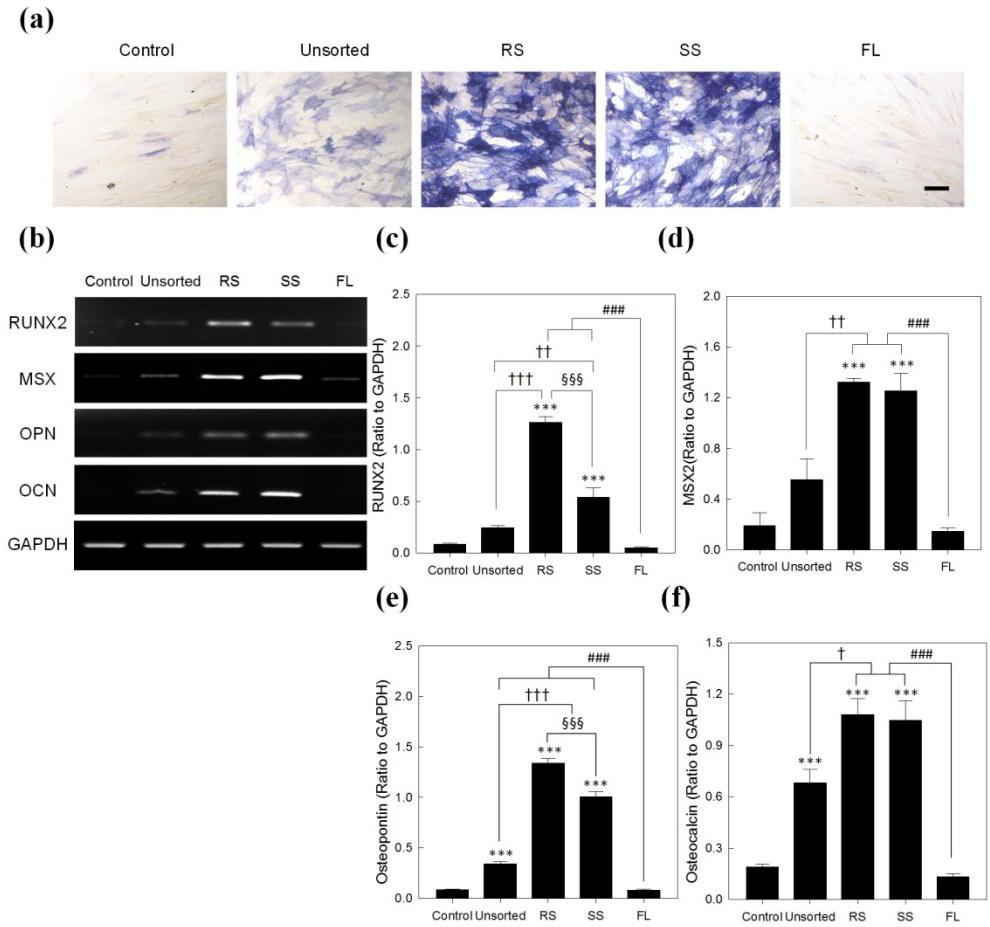

Figure 14. Comparison of osteogenic marker gene expressions in sorted subpopulations. Using the semi-quantities RT-PCR, the expression of markers for osteogenesis (RUNX2, MSX2, OPN, and OCN) were analyzed. There data were normalized to glyceraldehyde-3-phosphte dehydrogenase (GAPDH) and their relative expression was calculated. The bars represent mean ± SEM of at least three independent experiments. $^{*}P < 0.05$, $^{**}P < 0.01$, $^{***}P < 0.001$ versus the control hMSCs. $^{\dagger}P < 0.05$ $^{\dagger\dagger}P < 0.01$, $^{\dagger\dagger\dagger}P < 0.01$, versus unsorted hMSCs. $^{\#\#\#}P$ 0.001 versus FL cells. ANOVA followed by post hoc Tukey's HSD test.

differentiation potentials than the FL population.

To verify the multipotency of these stem cells, the sorted subpopulations were subjected to the induction of Schwann cell (SC) differentiation. SCs are the principal glia of the peripheral nervous system (PNS), and function to support neurons and encircle the axons of motor and sensory neurons to form the myelin sheath. SCs are involved in the conduction of nervous impulses along axons, nervous development and regeneration, trophic support for neurons, production of the nerve extracellular matrix, and modulation of neuromuscular synaptic activity. Specifically, SCs are known for their roles in supporting nerve regeneration, because nerves in the PNS consist of many axons myelinated by SCs. SCs can guide regeneration by forming mesenchymal stem cells, acts to stimulate mitogenesis, cell motility, and matrix invasion, giving it a central role in angiogenesis, tumorigenesis, and tissue, a type of tunnel that leads toward the target neurons.

There are many reports that hMSCs have the potential to transdifferentiate into neuron-like cells, exhibiting various neuronal markers and functional neuroactivity, in addition to multiple mesodermal cell types (Sanchez-Ramos et al., 2000; Woodbury et al., 2000; Trzaska et al., 2007;). To determine the status of the SC-induced cells, we examined mRNA levels of the SC-specific markers, Glial fibrillary acidic protein (GFAP), S100, and P0 using RT–PCR (Fig. 15). GFAP is an intermediate filament and a major component of the astrocyte cytoskeleton. The S100 protein is a calcium-binding protein that is expressed in astrocytes and SCs. It stimulates cell proliferation and migration while inhibiting apoptosis and differentiation. P0 (otherwise known as Myelin protein zero) is a cell-surface

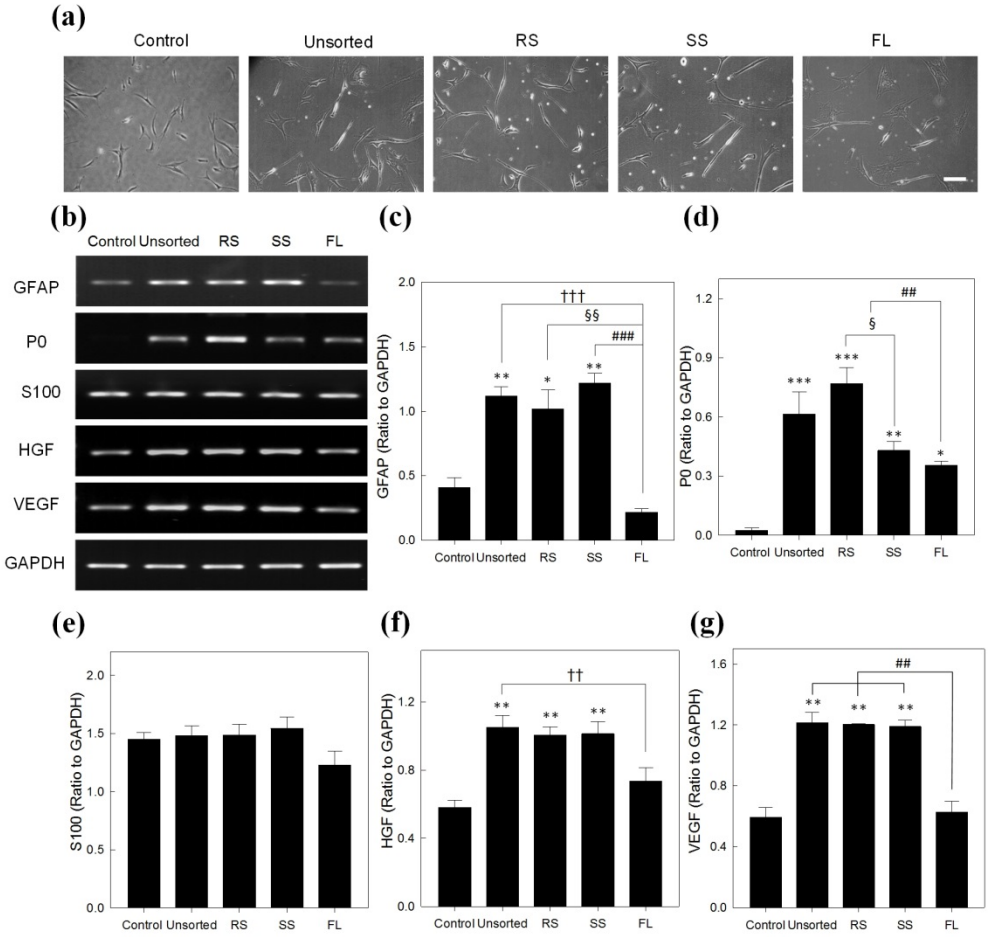

Figure 15. Comparison of Schwann cell marker gene expressions in sorted subpopulations. Using the semi-quantities RT-PCR, the expression of markers (GFAP, P0, and S100) and growth factors (HGF and VEGF) were analyzed. There data were normalized to glyceraldehyde-3-phosphte dehydrogenase (GAPDH) and their relative expression was calculated. The bars represent mean ± SEM of at least three independent experiments. $^{*}P < 0.05$, $^{**}P < 0.01$, $^{***}P < 0.001$ versus the control hMSCs. $^{\dagger\dagger}P < 0.01$, $^{\dagger\dagger\dagger}P < 0.001$ versus unsorted hMSC cells. $^{\S}P < 0.05$, $^{\S\S}P < 0.01$ versus RS cells. $^{\#\#}P < 0.01$, $^{\#\#\#}P < 0.001$ versus FL cells. ANOVA

followed by post hoc Tukey’s HSD test.

component of myelin that promotes adhesion between myelin membranes, thus helping PNS myelin compaction. As shown in Fig. 15b, GFAP expression by hMSCs is maintained in all non-induced and induced groups, but in FL cells, it was decreased 0.6-fold compared with the control group (Figs. 15b and c). Also, P0 expression by sorted hMSCs was increased in unsorted, RS, and SS cells compared with the control cells. Although P0 expression in FL cells was lower than in the other groups, its expression was highly sustained compared with the control cells (Figs. 15b and d). S100 levels were highly maintained in the induction groups and did not show significant differences among the cell groups, including the non-induced group (Figs. 15b and e). These results suggest that RS and SS groups may exhibit multipotency, and that they successfully differentiated into SCs. As mentioned earlier, SCs secrete specific growth factors, particularly the paracrine factors HGF and VEGF. HGF, a paracrine cellular growth factor secreted by regeneration. VEGF is one of the most important growth and survival factors: it induces angiogenesis and endothelial cell proliferation, and it plays an important role in regulating vasculogenesis. These proteins are reportedly secreted by SCs and exert paracrine effects during tissue injury to stimulate nerve regeneration. We examined whether the sorted subpopulations differentiated into compact SCs and secreted these growth factors, and compared them with the control and unsorted populations.

As shown (Figs. 15b and f), HGF expression increased by around 1.2–1.4 fold in the unsorted group compared with the control population, but its level in FL cells was a little lower than in the other populations. The levels of VEGF in the unsorted, RS, and SS groups were about twofold higher than in the control groups,

and FL cells exhibited basal levels similar to the control groups (Figs. 15b and g). These data suggest that the sorted RS and SS cells may have differentiated into SCs as well as the unsorted groups, and that the sorted FL cells may have lost this ability.

V. Discussion

Stem cells are defined as cells capable of continued self-renewal through replication and are the precursor cells of specific tissue types. Stem cells have been used to successfully replace dead cells and cells lost through degenerative diseases and to repair damaged tissue. Stem cells have a wide range of practical applications, including bone healing, repair of suspensory ligament tears and nerve injury, as well as inflammatory relief during arthritis and immune suppression in the context of graft rejection (Korbling and Estrov, 2003; Uccelli et al., 2008; Ertl et al., 2014). However, the utility of hMSCs is becoming increasingly unclear because of the recent finding of heterogeneous populations with different levels of stemness within hMSCs isolated by traditional plastic adherence (Lv et al., 2014). Furthermore, during long-term expansion post-isolation, stem cells may differentiate into undesired cell types, which results in a heterogeneous mixture and affects their suitability for transplantation. Therefore, the separation of target stem cells with high potential from other groups is very important for stem cell-based therapies and research. In this study, we used an HDF-based microfluidic chip that we designed previously to sort hMSCs into three subpopulations based on size (Jung et al., 2015). The sorted subpopulations showed conspicuous differences in size and viability, as well as different potentials. The RS and SS populations exhibited significantly higher differential potential than unsorted cells and FL cells during adipogenic and osteogenic differentiation. These results suggest that RS and SS groups possess greater differentiation potential than the unsorted populations because of the absence of FL cells with lower potential. These results indicate that the HDF

multibranched chip successfully sorted hMSCs based on size and that cell size is closely related to multipotency and can serve as an indicator of differential potential.

Although the size-dependent sorting of hMSCs was successful, cell size alone cannot be used to determine a cell's differentiation potential. There have been many studies of the effects of factors such as stiffness, the nuclear fraction of cells, and cell deformation on the multipotency of stem cells (Lee et al., 2014b). However, cell-size changes, in addition to limiting the physical characteristics of cells, are likely to affect cell proliferation and differentiation as well as other functions in the cellular environment. FL cells have been reported to be early osteoprogenitors and exhibit more osteogenic characteristics than small cells (Haasters et al., 2009; Poon et al., 2015). However, in our study, FL cells were obtained at a higher passage number (passage 17) and larger size (average 40 ± 5.1 μm) than in previous studies (average size $> 21.9 \pm 5.3$ μm), and ALP staining levels in FL cells did not increase according to osteogenic differentiation. This suggests that FL cells lose their differentiation ability through cell cycle exit (Despars et al., 2013).

Although RS and SS subpopulations were different in size, their differentiation potentials and sorting efficiencies were very similar. To determine if there were significant differences between the RS and SS groups in biological characteristics other than size, the current chip design could be modified. Larger cells may have more irregular (elliptical) shapes than smaller cells. This suggests that cells with a non-round shape may have different cutoff widths, leading them to irrelevant outlets. This may reduce sorting efficiency. An advanced chip model should consider shape as well as size for an additional filtering effect. In addition, hMSCs could aggregate or adhere together when introduced into the multichannel

chip. In such cases, abnormal cell groups would flow through the multibranched channels based on cell-diameter criteria, and would be discharged to outlets designed for larger-diameter cells. It is essential that these abnormal cells be sorted into smaller subgroups, because the subpopulations may be resuspended to seed long-term cultures. To prevent this problem, we could attempt to add a stirring system to the sorting chip to reduce cell sedimentation and aggregation and the secondary structure could be located at the front area of the main channel. For individual cells, we would expect a secondary filtering effect due to shape in addition to size.

Several studies have reported separation of hMSCs based on physical characteristics including cell size. However, most used hMSCs at an early passage number (< Passages 5-10), when the differentiation potentials of the various subpopulations are comparable (Khoo et al., 2008; Byun et al., 2012; Poon et al., 2015). Several reports on the extensive subcultivation of hMSCs described changes in morphology, proliferation, telomere length, and mesodermal differentiation capacity. In particular, although hMSCs retain osteogenic differentiation potential through 10-15 passages, adipogenic potential is lost. In addition, spontaneous osteogenic differentiation with the deposition of minerals is observed in some cultures (DiGirolamo et al., 1999; Khoo et al., 2008). In this study, our purpose was to acquire target subpopulations enriched with cells with stem cell characteristics. Thus, we used high-passage number hMSCs to harvest enriched cell populations with high differentiation potentials. Our data suggest that the sorting microfluidic chip described here can be used to filter hMSCs of a broad range of passage numbers for continuous long-term culture.

In conclusion, we acquired target subpopulations enriched with cells with stem cell characteristics from hMSCs using optimally designed microfluidic chip with HDF, which can help to increase the efficiency of the cell therapy and clinical application.

References

Aota A, Takahashi S, Mawatari K, Tanaka Y, Sugii Y, Kitamori T. 2011. Microchip-based plasma separation from whole blood via axial migration of blood cells. Anal Sci 27: 1173-1178.

Aravind L, Iyer LM., Leipe DD, Koonin EV. 2004. A novel family of P-loop NTPases with an unusual phyletic distribution and transmembrane segments inserted within the NTPase domain. Genome Biol 5: R30.

Arevalo JC, Yano H, Teng KK., Chao MV. 2004. A unique pathway for sustained neurotrophin signaling through an ankyrin-rich membrane-spanning protein. EMBO J 23: 2358-2368.

Arevalo JC, Pereira DB, Yano H, Teng KK., Chao MV. 2006. Identification of a switch in neurotrophin signaling by selective tyrosine phosphorylation. J Biol Chem 281: 1001-1007.

Baldin V, Lukas J, Marcote MJ, Pagano M, Draetta G. 1993. Cyclin D1 is a nuclear protein required for cell cycle progression in G1. Genes Dev 7: 812-821.

Bates S, Parry D, Bonetta L, Vousden K, Dickson C, Peters G. 1994. Absence of cyclin D/CDK complexes in cells lacking functional retinoblastoma protein. Oncogene 9: 1633-1640.

Bertoli C, Skotheim JM, de Bruin RA. 2013. Control of cell cycle transcription during G1 and S phases. Nat Rev Mol Cell Biol 14: 518-28.

Besson A, Dowdy SF, Roberts JM. 2008. CDK inhibitors: cell cycle regulators and beyond. Dev Cell 14: 159-169.

Bhagat AA, Kuntaegowdanahalli SS, Papautsky I. 2008. Continuous particle

separation in spiral microchannels using Dean flows and differential migration. Lab Chip 8: 1906-1914.

Brummelkamp TR, Bernards R, Agami R. 2002. Stable suppression of tumorigenicity by virus-mediated RNA interference. Cancer Cell 2: 243-247.

Bruus H. 2008. Theoretical Microfluidics. Oxford University Press, New York.Bertoli C, Skotheim JM, de Bruin RA. 2013. Control of cell cycle transcription during G1 and S phases. Nature reviews. Mol Cell Biol 14: 518-528.

Bouraoui L, Cruz-Garcia L, Gutierrez J, Capilla E, Navarro I. 2012. Regulation of lipoprotein lipase gene expression by insulin and troglitazone in rainbow trout Oncorhynchus mykiss) adipocyte cells in culture. Comp Biochem Physiol, Part A: Mol Integr Physiol 161: 83-88.

Borriello A, Cucciolla V, Oliva A, Zappia V, Della Ragione F. 2007. p27Kip1 metabolism: a fascinating labyrinth. Cell Cycle 6: 1053-1061.

Bracale A, Cesca F, Neubrand VE, Newsome TP, Way M, Schiavo G. 2007. Kidins220/ARMS is transported by a kinesin-1-based mechanism likely to be involved in neuronal differentiation. Mol Biol Cell 18: 142-152.

Byun MR, Jeong H, Bae SJ, Kim AR, Hwang ES, Hong JH. 2012. TAZ is required for the osteogenic and anti-adipogenic activities of kaempferol. Bone 50: 364-372.

Cesca F, Yabe A, Spencer-Dene B, Arrigoni A, Al-Qatari M, Henderson D, Phillips H, Koltzenburg M, Benfenati F, Schiavo G. 2011. Kidins220/ARMS is an essential modulator of cardiovascular and nervous system development. Cell Death Diff 2: e226.

Cesca F, Yabe A, Spencer-Dene B, Scholz-Starke J, Medrihan L, Maden CH, Gerhardt H, Orriss IR, Baldelli P, Al-Qatari M, et al. 2012. ARMS/Kidins220 mediates the integration of the neurotrophin and VEGF pathways in the vascular and nervous systems. Cell Death Diff 19: 194-208.

Chang MS, Arevalo JC, Chao MV. 2004. Ternary complex with Trk, p75, and an ankyrin-rich membrane spanning protein. J Neuro Res 78: 186-192.

Chao MV. 2003. Neurotrophins and their receptors: a convergence point for many signaling pathways. Nat Rev Neurosci 4: 299-309.

Chen PL, Scully P, Shew JY, Wang JY, Lee WH. 1989. Phosphorylation of the retinoblastoma gene product is modulated during cell cycle and cellular differentiation. Cell 58: 1193-1198.

Chen Y, Fu WY, Ip JP, Ye T, Fu AK, Chao MV, Ip NY. 2012. Ankyrin repeat-rich membrane spanning protein (Kidins220) is required for neurotrophin and ephrin receptordependent dendrite development. J Neurosci 32: 8263-8269.

Cheng SL, Shao JS, Charlton-Kachigian N, Loewy AP, Towler DA. 2003. Msx2 promotes osteogenesis and suppresses adipogenic differentiation of multipotent mesenchymal progenitors. J Biol Chem 278: 45969-45977.

Colter DC, Sekiya I, Prockop DJ. 2011. Identification of a subpopulation of rapidly self-renewing and multipotential adult stem cells in colonies of human marrow stromal cells. Proc Natl Acad Sci USA 98: 7841-7845.

Cristancho AG, Lazar MA. 2011. Forming functional fat: A growing understanding of adipocyte differentiation. Nat Rev Mol Cell Biol 12: 722-734.

Despars G, Carbonneau CL, Bardeau P, Coutu DL, Beausejour CM. 2013. Loss of the Osteogenic Differentiation Potential during Senescence Is Limited to Bone Progenitor Cells and Is Dependent on p53. PloSone 8: e73206.

Dezawa M, Kanno H, Hoshino M, Cho H, Matsumoto N, Itokazu Y et al. 2004. Specific induction of neuronal cells from bone marrow stromal cells and application for autologous transplantation. The Journal of clinical investigation 113: 1701-10.

DiGirolamo CM, Stokes D, Colter D, Phinney DG, Class R, Prockop DJ. 1999. Propagation and senescence of human marrow stromal cells in culture: A simple colony-forming assay identifies samples with the greatest potential to propagate and differentiate. Brit J Haematol 107: 275-281.

Di Carlo D, Irimia D, Tompkins RG, Toner M. 2007. Continuous inertial focusing, ordering, and separation of particles in microchannels. Proc Natl Acad Sci USA 104: 18892-18897.

Dominici M, Le Blanc K Mueller I, Slaper-Cortenbach I, Marini FC, Krause DS, Deans RJ, Keating A, Prockop DJ, Horwitz EM. 2006. Minimal criteria for defining multipotent mesenchymal stromal cells. International Society for Cellular Therapy position statement. Cytotherapy 8: 315-317.

Ducy P, Zhang R, Geoffroy V, Ridall AL, Karsenty G. 1997. Osf2/Cbfa1: a transcriptional activator of osteoblast differentiation. Cell 89: 747-54.

Duffy AM, Schaner MJ, Wu SH, Staniszewski A, Kumar A, Arevalo JC, Arancio O, Chao MV, Sharfman HE. 2011. A selective role for ARMS/Kidins220 scaffold protein in spatial memory and trophic support of entorhinal and frontal cortical neurons. Exp Neurol 229: 409-420.

Dulic V, Kaufmann WK, Wilson SJ, Tlsty TD, Lees E, Harper JW, Elledge SJ, Reed SI. 1994. p53-dependent inhibition of cyclin-dependent kinase activities in human fibroblasts during radiation-induced G1 arrest. Cell 76: 1013-1023.

El-Deiry WS, Tokino T, Velculescu VE, Levy DB, Parsons R, Trent J.M., Lin D., Mercer W.E., Kinzler K.W., and Vogelstein B. 1993. WAF1, a potential mediator of p53 tumor suppression. Cell 75: 817-825.

Ertl P, Sticker D, Charwat V, Kasper C, Lepperdinger G. 2014. Lab-on-a-chip technologies for stem cell analysis. Trends Biotechnol 32: 245-253.

Fu AY, Spence C, Scherer A, Arnold FH, Quake SR. 1999. A microfabricated fluorescence-activated cell sorter. Nat Biotechnol 17: 1109–1111.

Furlani EP, Sahoo Y, Ng KC, Wortman JC, Monk TE. 2007. A model for predicting magnetic particle capture in a microfluidic bioseparator. Biomedi Microdev 9: 451-463.

Furuno N, den Elzen N, Pines J. 1999. Human cyclin A is required for mitosis until mid prophase. J Cell Biol 147: 295-306.

Gao Y, Li W, Pappas D. 2013. Recent advances in microfluidic cell separations. Analyst 138: 4714-4721.

Giddings JC. 1985. Optimized field-flow fractionation system based on dual stream splitters. Anal Chem 57: 945-947.

Geislinger TM, Franke T. 2014. Hydrodynamic lift of vesicles and red blood cells in flow - from Fåhræus & Lindqvist to microfluidic cell sorting. Adv Colloid Interface Sci 208: 161-176.

Harper JW, Adami GR, Wei N, Keyomarsi K, Elledge SJ. 1993. The p21 Cdk-interacting protein Cip1 is a potent inhibitor of G1 cyclin-dependent kinases. Cell 75: 805-816.

Haasters F, Prall WC, Anz D, Bourquin C, Pautke C, Endres S, Mutschler W, Docheva D, Schieker M. 2009. Morphological and immunocytochemical characteristics indicate the yield of early progenitors and represent a quality the control for human mesenchymal stem cell culturing. J Anat 214: 759-767.

Higgins CF, Dorman CJ, Stirling DA, Waddell L, Booth IR, May G, Bremer E. 1988. A physiological role for DNA supercoiling in the osmotic regulation of gene expression in S. typhimurium and E. coli. Cell 52: 569-584.

Hisata S, Sakisaka T, Baba T, Yamada T, Aoki K, Matsuda M, Takai Y. 2007. Rap1-PDZ-GEF1 interacts with a neurotrophin receptor at late endosomes, leading to sustained activation of Rap1 and ERK and neurite outgrowth. J Cell Biol 178: 843-860.

Huh D, Bahng JH, Ling Y, Wei HH, Kripfgans OD, Fowlkes JB, Grotberg JB, Takayama S. 2007. Gravity-driven microfluidic particle sorting device with hydrodynamic separation amplification. Anal Chem 79: 1369-1376.

Hyun KA, Jung HI. 2013. Microfluidic devices for the isolation of circulating rare cells: a focus on affinity-based, dielectrophoresis, and hydrophoresis. Electrophoresis 34: 1028-1041.

Iglesias T, Cabrera-Poch N, Mitchell MP, Naven JP, Rozengurt E, Schiavo G. 2000 Identification and cloning of Kidins220, a novel neuronal substrate of protein kinase D. J Biol Chem 275: 40048-40056.

Jiang Y, Jahagirdar BN, Reinhardt RL, Schwartz RE, Keene CD, Ortiz-Gonzalez

XR, Reyes M, Lenvik T, Lund T, Blackstad M, Du J, Aldrich S, Lisberg A, Low WC, Largaespada DA, Verfaillie CM. 2002. Pluripotency of mesenchymal stem cells derived from adult marrow. Nature 418: 41-49.

Jadhav U, Ezhilarasan R, Vaughn SF, Berhow MA, Mohanam S. 2007. Iberin induces cell cycle arrest and apoptosis in human neuroblastoma cells. Int J Mol Med 19: 353-361.

Jiao W, Datta J, Lin HM, Dundr M, Rane SG. 2006. Nucleocytoplasmic shuttling of the retinoblastoma tumor suppressor protein via Cdk phosphorylation-dependent nuclear export. J Biol Chem 281: 38098-38108.

Jung H, Chun MS, Chang MS. 2015. Sorting of human mesenchymal stem cells by applying optimally designed microfluidic chip filtration. Analyst 140: 1265-1274.

Jung H, Shin JH, Park YS, Chang MS. 2014. Ankyrin Repeat-Rich Membrane Spanning (ARMS)/Kidins220 Scaffold Protein Regulates Neuroblastoma Cell Proliferation through p21. Mol Cell 37: 881-887.

Kawamata T, Yamada M, Yasuda M, Seki M. 2008. Continuous and precise particle separation by electroosmotic flow the control in microfluidic devices. Electrophoresis 29: 1423-1430.

Kennea NL, Mehmet H. 2002. Neural stem cells. J Pathol 197: 536-550.

Khoo ML, Shen B, Tao H, Ma DD. 2008. Long-term serial passage and neuronal differentiation capability of human bone marrow mesenchymal stem cells. Stem Cells Dev 17: 883-896.

Kim YH, Yoon DS, Kim HO, Lee JW. 2012. Characterization of different

subpopulations from bone marrow-derived mesenchymal stromal cells by alkaline phosphatase expression. Stem Cells Dev 21: 2958-2968.

Kong H, Boulter J, Weber JL, Lai C, Chao MV. 2001. An evolutionarily conserved transmembrane protein that is a novel downstream target of neurotrophin and ephrin receptors. J Neurosci 21: 176-185.

Korbling M, Estrov Z. 2003. Adult stem cells for tissue repair - a new therapeutic concept? N Engl J Med 349: 570-582.

Kranz TM, Goetz RR, Walsh-Messinger J, Goetz D, Antonius D, Dolgalev I, Heguy A, Seandel M, Malaspina D, Chao MV. 2015. Rare variants in the neurotrophin signaling pathway implicated in schizophrenia risk. Schizophr Res 168: 421-428.

Kuntaegowdanahalli SS, Bhagat AA, Kumar G, Papautsky I. 2009. Inertial microfluidics for continuous particle separation in spiral microchannels. Lab Chip 9: 2973-2980.

Lacy ER, Filippov I, Lewis WS, Otieno S, Xiao LM, Weiss S, Hengst L, Kriwacki RW. 2004. p27 binds cyclin-CDK complexes through a sequential mechanism involving binding-induced protein folding. Nat Struct Mol Biol 11: 358-364.

Lee DK, Yi T, Park KE, Lee HJ, Cho YK, Lee SJ, Lee J, Park JH, Lee MY, Song SU, Kwon SW. 2014a. Non-invasive characterization of the adipogenic differentiation of human bone marrow-derived mesenchymal stromal cells by HS-SPME/GC-MS. Sci Rep-Uk 4.

Lee OK, Kuo TK, Chen WM, Lee KD, Hsieh SL, Chen TH. 2004. Isolation of multipotent mesenchymal stem cells from umbilical cord blood. Blood. 103:

1669-75.

Lee WC, Shi H, Poon Z, Nyan LM., Kaushik T, Shivashankar GV, Chan JK, Lim CT, Han J, Van Vliet KJ. 2014b. Multivariate biophysical markers predictive of mesenchymal stromal cell multipotency. Proc Natl Acad Sci USA 111: E4409-4418.

Lee WC, Bhagat AA, Huang S, Van Vliet KJ, Han J, Lim CT. 2011. High-throughput cell cycle synchronization using inertial forces in spiral microchannels. Lab Chip 11: 1359-1367.

Lenshof A, Laurell T. 2010. Continuous separation of cells and particles in microfluidic systems. Chem Soc Rev 39: 1203-1217.

Liao YH, Hsu SM, Huang PH. 2007. ARMS depletion facilitates UV irradiation induced apoptotic cell death in melanoma. Cancer Res 67: 11547-11556.

Li J, Chen LA, Townsend CM, Jr., Evers BM. 2008. PKD1, PKD2, and their substrate Kidins220 regulate neurotensin secretion in the BON human endocrine cell line. J Biol Chem 283: 2614-2621.

Liao YH, Hsu SM, Huang PH. 2007. ARMS depletion facilitates UV irradiation induced apoptotic cell death in melanoma. Cancer Res 67: 11547-11556.

Liao YH, Hsu SM, Yang HL, Tsai MS, Huang PH. 2011. Upregulated ankyrin repeat-rich membrane spanning protein contributes to tumour progression in cutaneous melanoma. British J Cancer 104: 982-988.

Lopez-Menendez C, Gascon S, Sobrado M, Vidaurre OG, Higuero AM, Rodriguez-Pena A, Iglesias T, Diaz-Guerra M. 2009. ARMS/Kidins220 downregulation by excitotoxic activation of NMDARs reveals its involvement in neuronal survival and death pathways. J Cell Sci 122: 3554-3565.

Lopez-Menendez C, Gamir-Morralla A, Jurado-Arjona J, Higuero AM, Campanero MR, Ferrer I et al. 2013. Kidins220 accumulates with tau in human Alzheimer's disease and related models: modulation of its calpain-processing by GSK3beta/PP1 imbalance. Hum Mol Genet 22: 466-82.

Luo S, Chen Y, Lai KO, Arevalo JC, Froehner SC, Adams ME, Chao MV, Ip NY. 2005. {alpha}-Syntrophin regulates ARMS localization at the neuromuscular junction and enhances EphA4 signaling in an ARMS-dependent manner. J Cell Biol 169: 813-824.

Lv FJ, Tuan RS, Cheung KM, Leung VY. 2014. Concise review: The surface markers and identity of human mesenchymal stem cells. Stem Cell 32: 1408-1419.

McDonald JC, Whitesides GM. 2002. Poly(dimethylsiloxane) as a material for fabricating microfluidic devices. Acc Chem Res 35: 491-9.

MacDonald MP, Spalding GC, Dholakia K. 2003. Microfluidic sorting in an optical lattice. Nature 426: 421-424.

Madrigal M, Rao KS, Riordan NH. 2014. A review of therapeutic effects of mesenchymal stem cell secretions and induction of secretory modification by different culture methods. J Transl Med 12.

Malaspina D, Kranz TM, Heguy A, Harroch S, Mazgaj R, Rothman K, Berns A, Hasan S, Antonius D, Goetz R, et al. 2016. Prefrontal neuronal integrity predicts symptoms and cognition in schizophrenia and is sensitive to genetic heterogeneity. Schizoph Res 172: 94-100.

Malumbres M, Barbacid M. 2009. Cell cycle, CDKs and cancer: a changing paradigm. Nat Rev Cancer 9: 153-166.

Manning, G., Plowman, G.D., Hunter, T., and Sudarsanam, S. 2002. Evolution of protein kinase signaling from yeast to man. Trends Biochem Sci 27, 514-520.

Martin-Zanca D, Hughes SH, Barbacid M. 1986. A human oncogene formed by the fusion of truncated tropomyosin and protein tyrosine kinase sequences. Nature 319: 743-748.

Massague J. 2004. G1 cell-cycle control and cancer. Nature 432: 298-306.

Masamha CP, Benbrook DM. 2009. Cyclin D1 degradation is sufficient to induce G1 cell cycle arrest despite constitutive expression of cyclin E2 in ovarian cancer cells. Cancer Res 69: 6565-6572.

Matsuoka F, Tkeuchi I, Agata H, Kagami H, Shiono H, Kiyota Y, Honda H, Kato R. 2013. Morphology-Based Prediction of Osteogenic Differentiation Potential of Human Mesenchymal Stem Cells. PloSone 8: e55082.

Mizuno M, Yamada M, Mitamura R, Ike K, Toyama K, Seki M. 2013. Magnetophoresis-integrated hydrodynamic filtration system for size- and surface marker-based two-dimensional cell sorting. Anal Chem 85: 7666-7673.

Murray AW. 2004. Recycling cell cycle: cyclins revisited. Cell 116: 221-234.

Nakamura A, Dohi Y, Akahane M, Ohgushi H, Nakajima H, Funaoka H, Takakura Y. 2009. Osteocalcin secretion as an early marker of in vitro osteogenic differentiation of rat mesenchymal stem cells. Tissue Eng, Part C-Me 15: 169-180.

Neubrand VE, Thomas C, Schmidt S, Debant A, Schiavo G. 2010. Kidins220/ARMS regulates Rac1-dependent neurite outgrowth by direct interaction with the RhoGEF Trio. J Cell Sci 123: 2111-23.

Neubrand VE, Cesca F, Benfenati F, Schiavo G. 2012. ARMS/Kidins220 as a functional mediator of multiple receptor signaling pathways. J Cell Sci 125: 1845-1854.

Nilsson J, Evander M, Hammarstrom B, Laurell T. 2009. Review of cell and particle trapping in microfluidic systems. Anal Chem Acta 649: 141-157.

Pamme N, Manz A. 2004. On-chip free-flow magnetophoresis: continuous flow separation of magnetic particles and agglomerates. Anal Chem 76: 7250-7256.

Park HJ, Park HW, Lee SJ, Arevalo JC, Park YS, Lee SP, Paik KS, Chao MV, Chang MS. 2010. Ankyrin repeat-rich membrane spanning/Kidins220 protein interacts with mammalian Septin 5. Mol Cells 30: 143-148.

Park HW, Cho JS, Park CK, Jung SJ, Park CH, Lee SJ, Oh SB, Park YS, Chang MS. 2012. Directed induction of functional motor neuron-like cells from genetically engineered human mesenchymal stem cells. PLoSOne 7: e35244.

Petersson F, Aberg L, Sward-Nilsson AM, Laurell T. 2007. Free flow acoustophoresis: Microfluidic-based mode of particle and cell separation. Anal Chem 79: 5117-5123.

Phinney DG, Prockop DJ. 2007. Concise review: Mesenchymal stem/multipotent stromal cells: The state of transdifferentiation and modes of tissue repair - Current views. Stem Cell 25: 2896-2902.

Pittenger MF, Mackay AM, Beck SC, Jaiswal RK, Douglas R, Mosca JD, Moorman MA, Simonetti DW, Craig S, Marshak DR. 1999. Multilineage potential of adult human mesenchymal stem cells. Science 284: 143-147.

Primiceri E, Chiriaco MS, Rinaldi R, Maruccio G. 2013. Cell chips as new tools for cell biology--results, perspectives and opportunities. Lab Chip 13: 3789-3802.

Prockop DJ. 2007. "Stemness" does not explain the repair of many tissues by mesenchymal stem/multipotent stromal (MSCs). Clin Pharmacol Ther 82: 241-243.

Poon Z, Lee WC, Guan G, Nyan LM, Lim CT, Han J, Van Vliet KJ. 2015. Bone marrow regeneration promoted by biophysically sorted osteoprogenitors from mesenchymal stromal cells. Stem Cell Transl Med 4: 56-65.

Primiceri E, Chiriacò MS, Rinaldi R, Maruccio G. 2013. Cell chips as new tools for cell biology – results, perspectives and opportunities. Lab Chip 13: 3789–3802.

Rogers DA, Schor NF. 2013a. ARMS/Kidins220 depletion is associated with the neural-to Schwann-like transition in a human neuroblastoma cell line model. Ex Cell Res 319: 660-669.

Rogers DA, Schor NF. 2013b. ARMS/Kidins220 is expressed in neuroblastoma tumors and stabilizes neurotrophic signaling in a human neuroblastoma cell line. Pediatr Res 74: 517-524.

Sanchez-Ramos II, Castanera P. 2000. Acaricidal activity of natural monoterpenes on Tyrophagus putrescentiae (Schrank), a mite of stored food. J Stored Prod Res 37: 93-101.

Schneider T, Karl S, Moore LR, Chalmers JJ, Williams PS, Zborowski M. 2010. Sequential CD34 cell fractionation by magnetophoresis in a magnetic dipole flow sorter. Analyst 135: 62-70.

Sherman LS, Munoz J, Patel SA, Dave MA, Paige I, Rameshwar P. 2011. Moving from the laboratory bench to patients' bedside: considerations for effective therapy with stem cells. Clin Transl Sci 4: 380-386.

Sherr CJ. 1995. Mammalian G1 cyclins and cell cycle progression. Proc Assoc Am Phys 107: 181-186.

Sherr CJ, Roberts JM. 1999. CDK inhibitors: positive and negative regulators of G(1)-phase progression. Genes Dev 13: 1501-1512.

Shin Y, Han S, Jeon JS, Yamamoto K, Zervantonakis IK, Sudo R, Kamm RD, Chung S. 2012. Microfluidic assay for simultaneous culture of multiple cell types on surfaces or within hydrogels. Nat. Protoco 7: 1247-1259.

Smith JR, Pochampally R, Perry A, Hsu SC, Prockop DJ. 2004. Isolation of a highly clonogenic and multipotential subfraction of adult stem cells from bone marrow stroma. Stem Cell 22: 823-831.

Sniderhan LF, Stout A, Lu Y, Chao MV, Maggirwar SB. 2008. Ankyrin-rich membrane spanning protein plays a critical role in nuclear factor-kappa B signaling. Mol Cellular Neuro 38: 404-416.

Song H, Rosano JM, Wang Y, Garson CJ, Prabhakarpandian B, Pant K, Klarmann GJ, Perantoni A, Alvarez LM, Lai E. 2015. Continuous-flow sorting of stem and differentiation products based on dielectrophoresis. Lab on a chip 15: 1320-1328.

Stone HA, Stroock AD, Ajdari A. 2004. Engineering flows in small devices: Microfluidics toward a Lab-on-a-Chip. Annu Rev Fluid Mech 36: 381-411.

Sugaya S, Yamada M, Seki M. 2011. Observation of nonspherical particle behaviors for continuous shape-based separation using hydrodynamic filtration. Biomicrofluidics 5: 024103.

Titmarsh DM, Chen H, Glass NR, Cooper-White JJ. 2014. Concise review: Microfluidic technology platforms: Poised to accelerate development and translation of stem cell-derived therapies. Stem Cell Trans Med 3: 81-90.

Tontonoz P, Hu E, Graves RA, Budavari AI, Spiegelman BM. 1994. mPPAR gamma 2: Tissue-specific regulator of an adipocyte enhancer. Genes Dev 8: 1224-1234.

Trzaska KA, Rameshwar P. 2007. Current advances in the treatment of Parkinson's disease with stem cells. Curr Neurovasc Res 4: 99-109.

Tsai MS, Hwang SM, Tsai YL, Cheng FC, Lee JL, Chang YJ. 2006. Clonal amniotic fluid-derived stem cells express characteristics of both mesenchymal and neural stem cells. Biol Reprod 74: 545-551.

Uccelli A, Moretta L, Pistoia V. 2008. Mesenchymal stem cells in health and disease. Nat Rev Immunol 8: 726-736.

Vahey MD, Voldman J. 2008. An equilibrium method for continuous-flow cell sorting using dielectrophoresis. Anal Chem 80: 3135-3143.

Vodermaier HC. 2004. APC/C and SCF: Controlling each other and cell cycle. Curr Biol 14: R787-796.

Warkiani ME, Guan G, Luan KB, Lee WC, Bhagat AA, Chaudhuri PK, Tan DS, Lim WT, Lee SC, Chen PC, et al. 2014. Slanted spiral microfluidics for the ultra-fast, label-free isolation of circulating tumor cells. Lab Chip 14: 128-137.

Woodbury D, Schwarz EJ, Prockop DJ, Black IB. 2000. Adult rat and human bone marrow stromal cells differentiate into neurons. J Neurosci Res 61: 364-370.

Wu SH, Arevalo JC, Sarti F, Tessarollo L, Gan WB, Chao MV. 2009. Ankyrin repeat-rich membrane Spanning/Kidins220 protein regulates dendritic branching and spine stability in vivo. Dev Neurobiol 69: 547-557.

Wu HW, Lin CC, Lee GB. 2011. Stem cells in microfluidics. Biomicrofluidics 5: 13401.

Wu SH, Arevalo JC, Neubrand VE, Zhang H, Arancio O, Chao MV. 2010. The ankyrin repeat-rich membrane spanning (ARMS)/Kidins220 scaffold protein is regulated by activity-dependent calpain proteolysis and modulates synaptic plasticity. J Biol Chem 285: 40472-40478.

Xiong Y, Hannon GJ, Zhang H, Casso D, Kobayashi R, Beach D. 1993a. p21 is a universal inhibitor of cyclin kinases. Nature 366: 701-704.

Xiong Y, Zhang H, Beach D. 1993b. Subunit rearrangement of the cyclin-dependent kinases is associated with cellular transformation. Genes Dev 7: 1572-1583.

Yamada M, Kano K, Tsuda Y, Kobayashi J, Yamato M, Seki M, Okano T. 2007. Microfluidic devices for size-dependent separation of liver cells. Biomed Microdev 9: 637-645.

Yamada M, Nakashima M, Seki M. 2004. Pinched flow fractionation: Continuous size separation of particles utilizing a laminar flow profile in a pinched microchannel. Anal Chem 76: 5465-5471.

Yamada M, Seki M. 2006. Microfluidic particle sorter employing flow splitting and recombining. Anal Chem 78: 1357-1362.

Yen BL, Huang HI, Chien CC, Jui HY, Ko BS, Yao M, Shun CT, Yen ML, Lee MC, Chen YC. 2005. Isolation of multipotent cells from human term placenta. Stem Cell 23: 3-9.

Yoo JH, Woo DH, Chang MS, Chun MS. 2014. Microfluidic based biosensing for Escherichia coli detection by embedding antimicrobial peptide-labeled beads. Sens Actuators B 191: 211-218.

Zhang P, Liegeois NJ, Wong C, Finegold M, Hou H, Thompson JC, Silverman A, Harper JW, DePinho RA, Elledge SJ. 1997. Altered cell differentiation and proliferation in mice lacking p57KIP2 indicates a role in Beckwith-Wiedemann syndrome. Nature 387: 151-158.

국문초록

신경성장인자(neurotrophin)는 척추동물의 신경계 발생과정 중 신경세포의 생존과 분화를 결정짓는 인자로서 발생신경학 뿐만 아니라 퇴행성 신경질환 및 정신 질환 등 여러 분야에서 그 작용에 대한 연구가 활발하게 진행되어 왔다. 신경성장인자의 세포내 신호는 신경성장인자 수용기와 결합하여 전달되는데, 이들 수용기와 상호작용하는 매개(adaptor) 단백질에 의해 신호전달의 결과가 결정된다.

Ankyrin repeat-rich membrane spanning scaffold protein (ARMS)는 11개의 ankyrin repeats와 4개의 transmembrane 도메인, PDZ binding motif, sterile alpha motif (SAM) 도메인과 polyproline 도메인을 가지고 있으며, protein kinase D의 기질(Kidins220)로도 알려져 있다. 최근 보고된 연구결과를 통해 ARMS/Kidins220은 CrkL-G3G 복합체를 통해 mitogen-activated protein kinase (MAPK)의 신호를 비정상적으로 높이는 것으로 밝혀졌고, 특히 흑색종(melanoma)에서 발현양이 크게 상승했음이 알려졌다. 이것은 ARMS가 잠재적으로 암유발인자로서 작용할 가능성을 보여준 것으로 세포주기를 조절하는 역할에 대한 연구의 필요성을 인식하게 되었다.

본 연구에서는 ARMS 의 신경아세포종(neuroblastoma)의 세포주기(cell cycle)을 조절하는 단백질의 발현과 관련한 기능을 밝혔다. ARMS 의 발현감소는 세포의 성장률을 크게 감소시켰고 이것은 세포주기 중 G_1 단계를 조절하는 cyclin D1 과 CDK4 의 발현 감소에 의한 것임을 확인하였다. 반면에 다른 주기의 조절 단백질인 cyclin A, cyclin E 혹은 CDK2 의 발현양은 크게 변화가 없었다. 또한 ARMS 의 발현감소 세포주에

cyclin D1 과 CDK4 의 억제 인자인 p21 의 발현 증가에 따른 pRb 의 과인산화 (hyperphosphorylation)가 유의적으로 감소됨을 확인하였다.

우리는 이 연구를 통해 ARMS 가 세포주기를 조절하는 역할이 있음으로 확인하였고, 이것은 세포주기 중 G_1 단계의 cyclin D1/CDK4/ p21 의 발현 변화에 따른 신호전달에 의한 것임을 밝힘으로써 신경계질환 이외 암연구에 있어서 새로운 조절인자로서의 가능성을 제시하게 되었다.

사람 골수 유래 중간엽 줄기세포(hMSC)는 많은 성체 조직에 존재하면서 자가증식(self-renewal)이 가능하고 다양한 세포로 분화될 수 있는 분화능(multipotency)을 가진 세포이다. 따라서 이 세포의 특성을 연구하여 조직공학(tissue engineering)과 세포치료(cell therapy) 등에 적용하고자 많은 연구가 진행되어 왔다. 그러나 실제 hMSCs 는 체내 획득률이 낮고 다양한 크기의 세포로 이뤄져 있고, 각 세포군간 분화능의 차이가 있는 것으로 보고 되었다. 따라서 보다 높은 분화능을 가진 세포군을 분리하려는 많은 시도가 현재까지의 세포분리는 유세포분석기 (FACS)나 자기활성세포분석기 (MACS)와 같은 고가의 장비와 이를 운용할 수 있는 훈련된 인력이 필요하고 분리시 고가의 항체를 사용함으로써 실험방법에 있어 상당한 시간과 경비가 소모되어 왔다. 이에 본 연구에서는 이러한 단점을 보완하고 효율을 극대화 할 수 있는 방법으로 미세유체칩(microfluidic chip)을 제안하였다. 또한 분리시 세포의 손상(damage)이나 조작(modification)없이 본래의 상태를 유지하는데 최적인 유체역학적 여과(hydrodynamic filtration, HDF)의 원리를 적용하여 세포 크기별 분리 가능성을 검증하였다.

본 연구에서 제작된 미세유체 세포 분리칩(cell sorting chip)은 2개의 주입구 (각 시료 주입구, 유체 주입구)가 주채널에 연결되어 있고,

주채널의 다른 측면에 55 개의 다중가지 채널이 연결되어 있다. 이 다중가지 채널은 세개의 배출구로 연결되며, 세포의 크기에 따라 세 그룹으로 분리되도록 설계되었다. 즉 hMSCs는 미세 유체 세포 분리칩을 통해 크기에 따라 RS (rapidly self-renewal cells, < 25 μm) 세포군, SS (spindle shaped cells, 25-40 μm) 세포군, 그리고 보다 크고 평평한 모양의 FL (large, flattened cells, >40 μm) 세포군으로 분리되었고 분리효율은 지금까지 타 연구결과 보다 높은 86% 임을 확인하였다. 각 분리군의 성장속도, 표지 마커의 발현 및 분화 효율을 분석한 결과 RS 세포와 SS 세포가 FL 세포에 비해 성장속도가 빠르고, 표지 마커 (CD73, CD90, CD105)가 모두 발현됨을 확인하였다. 또한 분리된 각 세포군을 지방세포(adipocyte), 뼈세포(osteoblast), 슈반세포(Schwann cell)로 분화시켰을때, RS 세포군와 SS 세포군이 FL세포에 비해 분화률이 현저히 높음을 확인하였다.

결론적으로 우리는 최적화된 미세유체 분리칩을 사용하여 각기 다른 분화능을 가진 중간엽줄기세포 중 분화능이 높은 세포를 효과적으로 분리했고, 이 방법에 통해 세포치료의 효율을 증가시킬 수 있는 분리법을 개발했다는데 의의가 있다.

주요어: 사람 중간엽 줄기세포, 미세유체칩, 세포분리, 유체역학적 여과, 신경성장인자, ARMS, 세포주기, 세포주기조절 단백질

학 번: 2009-31135